DISSERTATION

submitted to the
Combined Faculty of Natural Sciences and Mathematics
of the Ruperto-Carola-University
of Heidelberg, Germany
for the degree of
Doctor of Natural Sciences

Put Forward by
Lennart Aufleger
born in Aurich

Oral examination: February 2nd, 2022

Nonlinear spectroscopy on an autoionizing two-electron resonance in intense, extreme ultraviolet fields at a free-electron laser

Referees:
Prof. Dr. Thomas Pfeifer
Prof. Dr. Andreas Wolf

If I have seen further
it is by standing on the shoulders of Giants
- Isaac Newton

Nichtlineare Spektroskopie einer autoionisierenden Zweielektronen-Resonanz in intensiven, extrem ultravioletten Feldern an einem Freie-Elektronen-Laser

In dieser Arbeit wird der Einfluß von hoch intensivem, extrem ultravioletten (XUV) Licht auf Helium experimentell untersucht. Dafür werden XUV Pulse eines Freie-Elektronen-Lasers (FEL) mit Transienter Absorptionsspektroskopie kombiniert und die Ergebnisse mit einem numerischen quantenmechanischen Model verglichen. Ein neuer Transiente-Absorptionsspektroskopie Aufbau ermöglicht die Messung des prototypischen Dreikörpersystems Helium am Freie-Elektronen-Laser in Hamburg (FLASH). Der Fokus in dieser Arbeit liegt auf der energetisch niedrigsten Zweielektronenresonanz, 2s2p, mit ihrer asymmetrischen Fano-Linienform. Dieser gebundene Zustand ist eingebettet in das Ionisationskontinuum und repräsentiert daher ein quantenmechanisches Interferometer. Dessen Haupteigenschaft, die Phasensensitivität, wird in dieser Arbeit genutzt um durch starke XUV Felder induziert Änderungen zu detektieren. In den Experimenten wird eine Veränderung der Linienform in Gegenwart hoch intensiver XUV Pulse beobachtet. Zunächst wird die Änderung der Liniensymmetrie mit einem numerischen Model, welches auf nur wenigen Zuständen basiert, untersucht und ein Zusammenhang zum transienten optischen Pumpen des angeregten Zustands hergestellt. Mit dem Einsatz realistischer stochastischer Pulse werden die Liniensymmetrieabhängigkeits-Untersuchungen im theoretischen Model um den Parameter der XUV Pulsdauer erweitert. Schließlich wird die Linienformverbreiterung mit Hilfe der Modelsimulation erklärt, welche eine Entkopplung der Beiträge der Zweiphotonen Absorption und der verstärkten Kopplung zurück an den Grundzustand erlaubt.

Nonlinear spectroscopy on a autoionizing two-electron resonance in intense, extreme ultraviolet fields at a free-electron laser

In this work, the influence of intense extreme-ultraviolet (XUV) fields on helium is experimentally investigated. Therefore, XUV pulses from a free-electron laser (FEL) are combined with transient absorption spectroscopy (TAS) and explored with numerical quantum-mechanical simulations. A novel TAS beamline enables measurements on the prototypical atomic three-body system, helium, at the free-electron laser in Hamburg (FLASH). In particular, the energetically lowest two-electron resonance, 2s2p, with its asymmetric Fano absorption line shape is of interest. This bound state is embedded in the single-ionization continuum and thus represents an atomic interferometer. Its main property, the sensitivity to phase, is used in this work to detect manipulations induced by strong XUV pulses. In the experiments, a distortion of the absorption line is observed in the presence of highly intense XUV pulses. Firstly, the line shape's symmetry change is investigated with a numerical few-level model simulation and found to be connected to the transient dressing of the excited state. Employing realistically modelled stochastic pulses, the investigation is extended to the line shape's dependence on the pulse duration. Finally, the line broadening is explained by the model simulation and allows for disentangling the contributing mechanisms, two-photon absorption and the increased reversion to the ground state.

List of publications

This work is based on proceedings and result partially published in the following articles:

- C. Ott, L. Aufleger, T. Ding, M. Rebholz, A. Magunia, M. Hartmann, V. Stooß, D. Wachs, P. Birk, G. D. Borisova, K. Meyer, P. Rupprecht, C. da Costa Castanheira, R. Moshammer, A. R. Attar, T. Gaumnitz, Z.-H. Loh, S. Düsterer, R. Treusch, J. Ullrich, Y. Jiang, M. Meyer, P. Lambropoulos, and T. Pfeifer (2019). *Strong-field extreme-ultraviolet dressing of atomic double excitation.* Physical Review Letters, 123(16):163201. doi:10.1103/PhysRevLett.123.163201. [1]
- L. Aufleger, P. Friebel, P. Rupprecht, A. Magunia, T. Ding, M. Rebholz, M. Hartmann, V. Stooß, C. Ott, and T. Pfeifer (2020). *Pulse length effects on autoionizing states under the influence of intense SASE XUV fields.* Journal of Physics B: Atomic, Molecular and Optical Physics, 53:234002. doi:10.1088/1361-6455/abbe2d. [2]
- L. Aufleger, P. Friebel, P. Rupprecht, A. Magunia, T. Ding, M. Rebholz, M. Hartmann, C. Ott, and T. Pfeifer (accepted, 2021). *Line-shape broadening of an autoionizing state in helium at high XUV intensity.* New Journal of Physics, doi:10.1088/1367-2630/ac3b2e. [3]

Additional publications with own contributions:

- M. Rebholz, T. Ding, V. Despré, L. Aufleger, M. Hartmann, K. Meyer, V. Stooß, A. Magunia, D. Wachs, P. Birk, Y. Mi, G. D. Borisova, C. da Costa, P. Rupprecht, G. Schmid, K. Schnorr, C. D. Schröter, R. Moshammer, Z.-H. Loh, A. R. Attar, S. R. Leone, T. Gaumnitz, H. J. Wörner, S. Roling, M. Butz, H. Zacharias, S. Düsterer, R. Treusch, G. Brenner, J. Vester, A. I. Kuleff, C. Ott, and T. Pfeifer (2021). *All-XUV Pump-Probe Transient Absorption Spectroscopy of the Structural Molecular Dynamics of Di-iodomethane.* Physical Review X, 11(3):031001. doi:10.1103/PhysRevX.11.031001. [4]
- T. Ding, M. Rebholz, L. Aufleger, M. Hartmann, V. Stooß, A. Magunia, P. Birk, G. D. Borisova, D. Wachs, C. da Costa Castanheira, P. Rupprecht, Y. Mi, A. R. Attar,

T. Gaumnitz, Z.-H. Loh, S. Roling, M. Butz, H. Zacharias, S. Düsterer, R. Treusch, A. Eislage, S. M. Cavaletto, C. Ott, and T. Pfeifer (2021). *Measuring the frequency chirp of extreme-ultraviolet free-electron laser pulses by transient absorption spectroscopy.* Nature Communications, 12:643. doi:10.1038/s41467-020-20846-1. [5]

- T. Ding, M. Rebholz, L. Aufleger, M. Hartmann, V. Stooß, A. Magunia, P. Birk, G. D. Borisova, C. da Costa Castanheira, P. Rupprecht, Y. Mi, T. Gaumnitz, Z.-H. Loh, S. Roling, M. Butz, H. Zacharias, S. Düsterer, R. Treusch, C. Ott, and T. Pfeifer (2020). *XUV pump–XUV probe transient absorption spectroscopy at FELs.* Faraday Discussions, 228, 519-536. doi:10.1039/D0FD00107D. [6]

- A. Magunia, L. Aufleger, T. Ding, P. Rupprecht, M. Rebholz, C. Ott, and T. Pfeifer (2020). *Bound-State Electron Dynamics Driven by Near-Resonantly Detuned Intense and Ultrashort Pulsed XUV Fields.* Applied Sciences, 10(18):6153. doi:10.3390/app10186153. [7]

- T. Ding, M. Rebholz, L. Aufleger, M. Hartmann, K. Meyer, V. Stooß, A. Magunia, D. Wachs, P. Birk, Y. Mi, G. D. Borisova, C. da Costa Castanheira, P. Rupprecht, Z.-H. Loh, A. R. Attar, T. Gaumnitz, S. Roling, M. Butz, H. Zacharias, S. Düsterer, R. Treusch, S. M. Cavaletto, C. Ott, and T. Pfeifer (2019). *Nonlinear Coherence Effects in Transient-Absorption Ion Spectroscopy with Stochastic Extreme-Ultraviolet Free-Electron Laser Pulses.* Physical Review Letters, 123(10):103001. doi:10.1103/PhysRevLett.123.103001. [8]

Contents

1. Introduction

The physical world as we experience it is made from matter. Representatives of that are single atoms, e.g. noble gases, larger molecules, and even complex solid-state materials. Condensed matter comprises also all biological tissue, of which the human body is made. Its blueprint is encoded in molecular form within the DNA, which stands out as the building block of life.

The question, however, arises, what holds the constituents of molecules together. Chemistry answers this question about the assembly of individual atoms to molecules and other complex forms of matter. While the strong and the weak fundamental interaction are crucial within the atomic nucleus, the intra-atomic force within molecules is dominated by the electromagnetic interaction. Hence, the 'glue' between atoms are electrons. To gain further understanding of the world as we know it, it is key to expand detailed knowledge about the electrons surrounding the atomic core and their properties. The interest, though, is not limited to the electronic structure within an atom but extends to their dynamics and interaction with external factors. To get an intuitive understanding of this topic one can think about the most basic atom, hydrogen: A singly positively charged core surrounded by one electron. As the electron is influenced by the Coulomb potential of the nucleus, it forms an electronic structure with distinct energy levels. This electronic structure can be calculated by the fundamental equation of non-relativistic quantum mechanics, the Schrödinger equation. While this quantum mechanical equation of motion can be solved analytically for the described two-body problem of hydrogen [9], more complex cases remain unsolved.

Even for the next heavier element in the periodic table, helium, open questions remain. Here, a doubly positively charged nucleus is enclaved by two electrons. Therefore, it represents the quantum mechanical version of the classical three-body problem [10, 11].

Helium thus presents the perfect playground at the interface of the analytically calculable systems to the most basic analytically non-solvable problems, providing the chance to learn about fundamental quantum mechanics. One experimental approach is to put this quantum system in extreme conditions and measure its response. Such an experiment can be realized by exposing the helium atom to strong electromagnetic fields similar in strength to intra-atomic forces [12]. The system is pumped into an excited state to investigate the influence of such external fields. This excited-state decay with its natural lifetime provides a natural dynamical evolution of the quantum system which can be explored by perturbations with external forces. The photon energy of the extreme-ultraviolet (XUV) spectral region enables the simultaneous excitation of both electrons in helium. These resulting doubly-excited states are located above the single-electron ionization potential. Hence, they decay into singly ionized helium and a free electron.

The doubly excited states in helium have been extensively studied, both, experimentally and theoretically [10]. Among those studies are theoretical investigations into the strong-field behavior of doubly-excited states [13–16]. For an experimental investigation into these states two methods are established: Firstly, measurements using reaction microscopes quantifying the momentum of the reaction products [17–19], including the ejected electron, have been conducted. More specifically, electron spectroscopy has been successfully utilized with strong electric DC fields [20] or intense electromagnetic fields in the near-visible frequency range [21–23] as perturbation.
Another access to the atomic system is provided via the emitted dipole of the system. Light-matter interaction is mediated by the dipole moment of an electronic transition in an atomic system. This is no one way street and absorption of light leads in many cases to successive emission of a photon. These emitted dipole fields interfere with the external electric field and result in the classical spectral absorption lines. Under the influence of strong fields, the dipole response can be manipulated. This concept allows for the phase-sensitive detection of high-intensity effects of the two-electron transition. The experimental method that builds upon these dipole interferences, transient absorption spectroscopy (TAS), has been extensively used to investigate helium [24–30]. A direct way to impose a manipulation of the phase is to shift the doubly excited state's energy level. This can be conducted by perturbing the atomic system with high laser intensities in the visible (VIS) and infrared (IR) spectral regime via ponderomotive shifts [25]. Further investigations have studied the impact of impulsive, strong perturbations [29].
In the before-mentioned TAS experiments tabletop sources are used: The excitation is realized with a coherent high-order harmonic source while the strong perturbation is induced by intense laser pulses in the VIS and IR spectral regime. With the advent of

the free-electron laser (FEL) [31], new opportunities emerged. These light sources at large-scale facilities provide intensities allowing for resonant strong field perturbation in the XUV regime. The high reachable peak intensity comes at a cost, though. In contrast to conventional laser sources the accelerator-based pulses lack full temporal coherence. Their stochastic pulse structure varies from shot to shot [32].

In this work, experiments in helium with stochastic FEL pulses are realized. Specifically, the goal is to explore the behavior of a doubly-excited state representative, the 2s2p state, in intense XUV fields. The respective resonance ($1s^2 \rightarrow 2s2p$) is the energetically lowest and spectroscopically isolated two-electron transition in helium. By using intense XUV fields one can go beyond the pure weak-field excitation and additionally influence the transition before the excited state decays. This leads to strong coupling of the doubly excited state. The aim is to achieve new insight by tuning the intensity of the XUV fields.

The conducted experiments extend the manipulation of the helium doubly excited state observed in strong IR fields to the single-color XUV strong-coupling regime. The experimental setup utilized for the investigations is a novel TAS vacuum beamline, in which the beam of the stochastic high-intensity XUV source is focused into a small volume of helium gas. While tuning the intensity, or more precisely the energy of the XUV pulses, the transmitted XUV beam is spectrally resolved and the absorption spectrum recorded.

This thesis is structured as follows: In the beginning (ch. 2) the fundamental physical background is discussed that is required for understanding the results presented in this thesis. Here, also a brief introduction into the working principle of an FEL is provided (ch. 2.5). This is followed by a description of the experimental setup and the facility-based devices (ch. 3), detailing the essential parts used in the conducted measurements. Thereafter the methods utilized in the data evaluation processes (ch. 4) are shown. This is succeeded by the introduction of the numeric model simulation (ch. 5) that will enable the physical interpretation of the acquired results. In chapter 6 the results are presented, discussed and interpreted with simulations. Thereby, chapter 6.1 contains observations on line-shape modifications in strong fields. The adjacent chapter 6.2 analyzes the impact of the pulse envelope on the aforementioned effect. Finally, in chapter 6.3 further explorations into the coupling of the states by intense fields are conducted. In the end, the key finding of this thesis are summarized in a conclusion and their potential for future experiments reviewed.

2. Theory

In this chapter, the physical background and the respective theories relevant for the motivation and results of this work are discussed. First, light-matter interaction of quantum systems is treated for weak and strong electric fields. In chapter 2.2 an introduction to Fano's theory of bound states embedded in a continuum is provided. The basis for the experimental detection method and second part of light-matter interaction is the topic of chapter 2.3. The atomic target system, helium, is presented in chapter 2.4. Finally, the light source providing extreme ultraviolet radiation is discussed. In the respective chapter (2.5), the fundamental working of free-electron lasers will be described.

2.1. Light-Matter Interaction

The subject of this thesis can be classified in essence as light-matter interaction. The interaction is based on the exchange of energy and momentum between the light quanta and the matter particles. In principle, charged particles that are within the influence of a constant potential can participate in the energy transfer, unlike free charged particles, which follow the electric field of the electromagnetic wave without a transfer in energy. With this condition of charged particles in a potential, this interaction is very prominent in atomic and molecular physics: Both, electrons and the positively charged nuclei can take part in the interaction. This thesis is build upon the photon-absorption process by electrons in atomic systems.

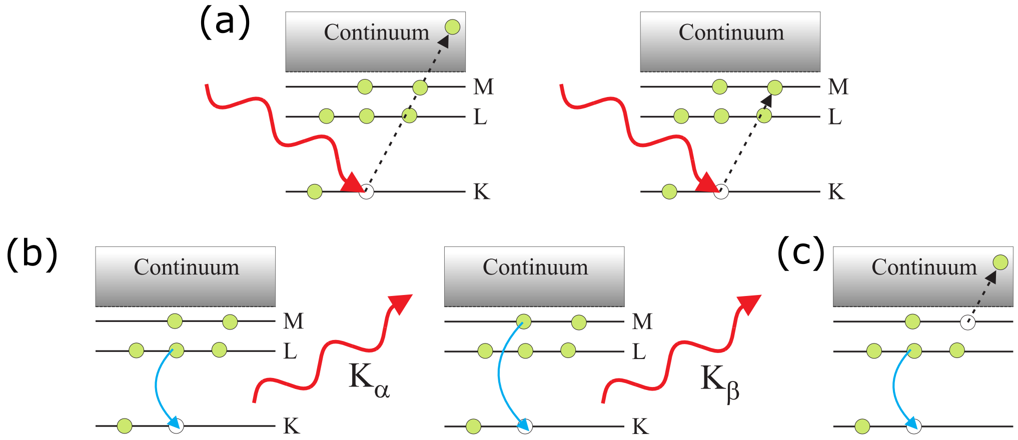

Figure 2.1.: Light-matter-interaction processes. **(a)** Photo absorption. **(b)** Fluorescence emission. **(c)** Auger electron emission. Adapted from [33].

Depending on the energy of the absorbed photon an electron is either excited to an energetically higher bound state or emitted to the continuum creating an electron vacancy, called hole, in its place (fig. 2.1(a)). The process of *fluorescence* describes the recombination of this hole with an electron under the emission of a photon (fig. 2.1(b)). The electron that is participating in the recombination process is either the beforehand excited one or another electron from an energetically higher state. Alternatively to the emission of a photon, the excited system can relax via the ejection of an electron (fig. 2.1(c)). This process is called *Auger* electron emission after its discoverer Auger and Meitner.

The binding energy of the electron needs to be overcome for a system to be ionized and the electron to be ejected. For most interactions, in particular in the context of this work, one can concentrate on the electric field of the electro-magnetic waves. This is justified, since the magnetic field strength as well as the respective transitions probabilities are significantly smaller and can be neglected in dipole approximation.

2.1.1. Introduction of Quantum Mechanics

In order to understand the processes in atomic systems irradiated by electric fields, a short introduction in the quantum mechanical description of an atomic system and its interaction is provided. The time-dependent Schrödinger equation (SE) is the equation of motion for a non-relativistic quantum system:

$$i\frac{\partial}{\partial t}\left|\mathbf{\Psi}(t)\right\rangle = \hat{H}(t)\left|\mathbf{\Psi}(t)\right\rangle . \tag{2.1}$$

The Hamilton operator $\hat{H}(t)$ hereby describes the atomic system. Equation 2.1 determines the the time-dependent wavefunction $|\boldsymbol{\Psi}(t)\rangle$, which describes the distinct states of the system. This wavefunction can be represented as a superposition of the orthogonal eigenstates, the eigenbasis of the Hamiltonian

$$|\boldsymbol{\Psi}(t)\rangle = \sum_k c_k(t)\, |\mathit{\Phi}_k\rangle + \int dE'\; c_{E'}(t)\, |\chi_E\rangle \tag{2.2}$$

which can contain bound $|\mathit{\Phi}_k\rangle$ and continuum $|\chi_E\rangle$ states. The in general complex expansion coefficients $c_k(t)$, the state coefficients, describe the state's individual contribution and contain the temporal evolution of the state. A general solution to the SE is given by

$$c_k(t) \;=\; c_{k,0} \cdot e^{-iE_k/\hbar \cdot t}. \tag{2.3}$$

This represents a phase evolution of the state k with its eigenenergy E_k starting from the initial value $c_{k,0} \;=\; c_k(t=0)$ at time $t = 0$. The equation is analogue for the continuum states where the states are parameterized with E' instead of k.
A quantity is never measured with absolute precision in quantum mechanic but only determined in terms of its expectation value

$$\langle X\rangle(t) \;=\; \langle \boldsymbol{\Psi}(t)|\hat{X}|\boldsymbol{\Psi}(t)\rangle \tag{2.4}$$

with $\hat{X}(t)$ the operator to the respective observable. Calculating the expectation value (here without loss of generality limited to bound states)

$$\langle \boldsymbol{\Psi}(t)|\hat{X}|\boldsymbol{\Psi}(t)\rangle = \sum_{k,m} c_{k,t=0}\; c^*_{m,t=0}\; \langle \mathit{\Phi}_m|\hat{X}|\mathit{\Phi}_k\rangle\; e^{-i\frac{E_k - E_m}{\hbar}\cdot t} \tag{2.5}$$

one can identify that a temporal evolution is only observed when state $|\boldsymbol{\Psi}(t)\rangle$ is a superposition of two or more eigenstates. This builds the basis for quantum-mechanical wave packages.

2.1.2. Perturbation Theory

A coupling of states is either possible by an external coupling, e.g an electromagnetic field, or a configuration interaction (see chapter 2.2). Under the influence of small external fields, the system can be accurately described by low-order perturbation theory. In that case, the Hamiltonian constitutes of the field free Hamiltonian $\hat{H}_0$ and the small perturbation H':

$$\hat{H} = \hat{H}_0 + \eta \cdot \hat{H}' \qquad \text{with} \qquad \eta \ll 1. \tag{2.6}$$

The solution to the SE of the field free Hamiltonian $\hat{H}_0$ is given as

$$|\mathbf{\Psi}(t)\rangle = \sum_{k,0} c_k e^{-i\frac{E_k}{\hbar}t} |\mathit{\Phi}_k\rangle \tag{2.7}$$

with $|\mathit{\Phi}_k\rangle$ the eigenstates to the field free Hamiltonian and hence the expansion coefficients c_k being time independent. When the perturbation acts after a time $t = 0$ the expansion coefficient becomes time dependent and is in the first order determined by

$$c_m^{(1)}(t) \;=\; -\frac{i}{\hbar}\sum_k c_{k,0} \int_0^t e^{i\omega_{mk}t'} \langle \mathit{\Phi}_m|\hat{H}'(t)|\mathit{\Phi}_k\rangle \;. \tag{2.8}$$

The perturbation is assumed to be an interaction of a real valued electric field $\tilde{F}(t)$ with the system via the dipole interaction

$$\hat{H}'(t) \;=\; \hat{d} \cdot \tilde{F}(t) \tag{2.9}$$

which couples two states $\mathit{\Phi}_k$, $\mathit{\Phi}_m$. The monochromatic electric field can be expressed in the complex representation $\tilde{F}(t) = \tilde{F}_0, \frac{1}{2}(e^{i\omega_F t} + e^{-i\omega_F t})$. Combining equation 2.8 and equation 2.9 results in

$$c_m^{(1)}(t) \;=\; -\frac{i}{\hbar}\, c_k^{(0)}\, d_{mk} \cdot \frac{\tilde{F}_0}{2} \int_0^t dt' e^{i(\omega_{mk}+\omega_F)t'} + e^{i(\omega_{mk}-\omega_F)t'} \tag{2.10}$$

with $d_{mk} = \langle \mathit{\Phi}_m|\hat{d}|\mathit{\Phi}_k\rangle$ the dipole coupling element of those two states.
In general, the population probability of a state $\mathit{\Phi}_k$ at time t is determined by

$$P_k(t) = |c_k(t)|^2. \tag{2.11}$$

Here, the integral over the population computes to

$$|c_k(t)|^2 \propto \frac{4 \cdot \sin^2((\omega_{mk} + \omega_F)t/2)}{(\omega_{mk} + \omega_F)^2 \cdot t} \xrightarrow{t\to\infty} 2\pi \cdot \delta(\omega_{mk} \pm \omega_F) \tag{2.12}$$

resulting in a temporal evolution of the population:

$$|c_k(t)|^2 \;=\; \frac{2\pi}{\hbar^2}\,|d_{mk}|^2 \cdot \frac{\tilde{F}_0^2}{4} t \cdot \delta(\omega_{mk} \pm \omega_F). \tag{2.13}$$

This description is valid as long as the transfer of population is not significant, e.g. the ground state is not depleted and its depletion rate is in good approximation vanishing $\frac{\partial}{\partial t} c_g \;=\; 0$.
One can see in equation 2.13, though, that the transferred population is proportional to the intensity of the external field. Hence, the description of the light-matter interaction with intense electric fields, which is considered in this work, requires a different approach.

2.1.3. Laser Dressing

High field intensities close to a resonance lead to significant population transfer. Therefore, a quantum mechanical treatment beyond the perturbation theory is required to describe such system. Here, the example of a two-level system which is strongly coupled by an external field energetically close to the transition energy of the states is looked into.
The two states, $|\Phi_a\rangle$ and $|\Phi_b\rangle$, are eigenstates of the Hamiltonian $\hat{H}_0$ of the unperturbed system. A coupling between the states is introduced by the external field $F(t)$ via the dipole $\hat{d}$. Due to this coupling the states $|\Phi_a\rangle$ and $|\Phi_b\rangle$ are not eigenstates of the Hamiltonian $\hat{H} = \hat{H}_0 + \hat{H}'$ with $\hat{H}'(t) \;=\; \hat{d} \cdot \tilde{F}(t)$. Nevertheless, they will serve as the orthogonal basis here

$$|\boldsymbol{\Psi}(t)\rangle = c_a(t) \cdot |\Phi_a\rangle \;+\; c_b(t) \cdot |\Phi_b\rangle\,. \tag{2.14}$$

In order to solve the SE and find the new eigenstates of the dressed system the SE is written in its vector/matrix representation:

$$i\frac{\partial}{\partial t}\begin{pmatrix} c_a(t) \\ c_b(t) \end{pmatrix} = H(t)\begin{pmatrix} c_a(t) \\ c_b(t) \end{pmatrix} \qquad \text{with} \qquad H(t) \;=\; \begin{pmatrix} E_a & d^*_{ab}\cdot\tilde{F}(t) \\ d_{ab}\cdot\tilde{F}(t) & E_b \end{pmatrix}. \tag{2.15}$$

The coupling of the states is noted on the off-diagonal elements in the Hamiltonian, while the eigenenergy of the basis states is included on the diagonal. The real-valued electric field $\tilde{F}(t)$ is chosen in the complex representation for this treatment

$$\tilde{F}(t) \;=\; \tilde{F}_0 \cdot \frac{1}{2}\left(e^{i\omega_F t} - e^{-i\omega_F t}\right) \tag{2.16}$$

with the amplitude $\tilde{F}_0$, or in case of a slowly varying field envelope $\tilde{F}_0(t)$, and ω_F the frequency of the coupling electric field.

To eliminate the fast oscillating terms in the resulting differential equations (eq. 2.15), the rotating-wave approximation is applied,

$$\begin{aligned} c_a(t) &= \bar{c}_a(t) \cdot e^{-i(\omega_a - \Delta/2)\cdot t}, \\ c_b(t) &= \bar{c}_b(t) \cdot e^{-i(\omega_b + \Delta/2)\cdot t} \end{aligned} \tag{2.17}$$

with the detuning of the electric field from the energy gap of the states

$$\Delta \;=\; (\omega_b - \omega_a) \;-\; \omega_F.$$

In this co-rotating frame the Hamiltonian operator changes to

$$H_{rot} = \hbar \cdot \begin{pmatrix} \Delta/2 & \Omega \\ \Omega^* & -\Delta/2 \end{pmatrix} \tag{2.18}$$

with $\Omega = d_{ab} \cdot F_0/\hbar$ being the Rabi frequency of the system. To solve this Hamiltonian, the matrix is diagonalized and the eigenstates and vectors determined. The eigenenergies of the dressed system calculate to

$$\begin{aligned} E_a^{\pm} &= E_a - \frac{\hbar\Delta}{2} \pm \frac{\hbar}{2}\,\Omega_G \qquad \text{and} \\ E_b^{\pm} &= E_b + \frac{\hbar\Delta}{2} \pm \frac{\hbar}{2}\,\Omega_G \end{aligned} \tag{2.19}$$

with the generalized Rabi frequency $\Omega_G \;=\; \sqrt{\Delta^2 + |\Omega|^2}$. Thus, the states of the system are shifted in reference to the energy levels of the unperturbed system.

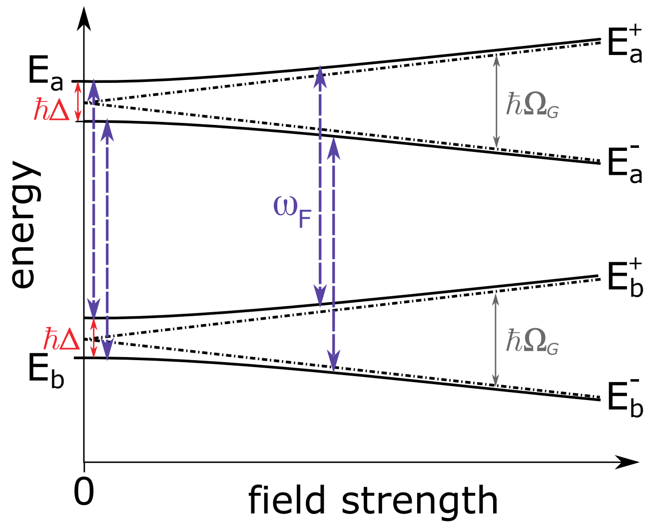

Figure 2.2.: Energy levels (E_a, E_b) of a two-level system dressed with intense electric fields of frequency ω_F detuned by Δ, determined by 2.19. The Rabi frequency Ω governs the level repulsion for rising field strengths.

The energy levels (eq. 2.19) show a second level, which is shifted by the detuning Δ and induced by the laser coupling for a weak field strength, as plotted in figure 2.2. The splitting between the energy levels increases with rising field strength. This repulsion is known as the AC Stark effect and leads to absorption features like the Mollow triplet when coupling between the states or the Autler Townes doublet when the states are probed from a third uninvolved state [34, 35]. In principle, the energy level shifts are only present for the duration of the external electric field dressing. Meanwhile, the state coefficients in the rotating basis of the unperturbed states compute to

$$\begin{aligned} \bar{c}_a &= -i\frac{\Omega}{\Omega_G}\sin\left(\frac{\Omega_G}{2}\cdot t\right), \\ \bar{c}_b &= +i\frac{\Delta}{\Omega_G}\sin\left(\frac{\Omega_G}{2}\cdot t\right) + \cos\left(\frac{\Omega_G}{2}\cdot t\right). \end{aligned} \tag{2.20}$$

They show a time-dependent oscillation of the population, following equation 2.13, with the frequency proportional to the generalized Rabi frequency Ω_G. This leads to a oscillatory population transfer between the levels in dependence on the driving-frequency detuning and the field strength.

Note, that this treatment has been derived for the case of monochromatic fields. For laser pulses, which are inherently not monochromatic, a numeric approach can be used, see chapter 5.

2.2. Fano's Embedded State

As a Fano-shaped resonance is in the center of the experimental and theoretical work in this thesis, Fano's treatment of this resonance is described in the following. Whenever a discrete bound state is embedded in the continuum (fig. 2.3(a)), asymmetric line shapes are observed, as generally described by Fano [36]. The treatment can be detailed as follows, continuing the nomenclature of the previous chapter: In absence of the coupling, the wave functions of the bound $|\mathit{\Phi}\rangle$ and the energetically degenerated continuum states $|\chi_E\rangle$ are eigenstates of the Hamiltonian $\hat{H}$ with

$$\begin{aligned} \langle \mathit{\Phi} | \hat{H} | \mathit{\Phi} \rangle &= E_e \\ \langle \chi_{E''} | \hat{H} | \chi_{E'} \rangle &= E' \; \delta(E'' - E'). \end{aligned} \tag{2.21}$$

When the field-free coupling of the bound state $\mathit{\Phi}$ with the continuum χ_E is introduced by the so-called configuration interaction $V_{CI,E}$

$$\langle \chi_E | \hat{H} | \mathit{\Phi} \rangle = V_{CI,E} \tag{2.22}$$

the states and no longer eigenstates of the system, but can serve as the orthogonal basis of the new eigenstates

$$|\Psi\rangle = a_E \, |\mathit{\Phi}\rangle + \int dE' \; b_{E,E'} \; |\chi_{E'}\rangle \tag{2.23}$$

Fano found the solution for these coefficients with some algebraic effort [36]. The new eigenstates are

$$|\Psi\rangle = \frac{\sin \Delta_E}{\pi V_{CI,E}} \, |\mathit{\Phi}\rangle - \cos(\Delta_E) \, |\chi_{E'}\rangle \tag{2.24}$$

with the parameter Δ_E being

$$\Delta_E = -\arctan \frac{\pi \left| V_{CI,E} \right|^2}{E - E_e - F(E)} \quad \text{with} \quad F(E) = \mathfrak{P} \int dE' \frac{\left| V_{CI,E'} \right|^2}{E - E'}. \tag{2.25}$$

The new, modified bound computes to

$$\left| \mathit{\Phi}' \right\rangle = |\mathit{\Phi}\rangle + \mathfrak{P} \int dE' \frac{V_{E'}}{E_e - E'} \, |\chi_{E'}\rangle \tag{2.26}$$

with $\mathfrak{P}$ being the principle value of the integral circumventing the pole at $E_e = E'$. One can directly identify the new bound state to be a mixture of the former bond state with a portion of the continuum state. For a transition $\hat{d}$ from a distant state $|g\rangle$, which is not degenerated with the continuum, the typical Fano profile is derived from the relative transition strength of the path into the new eigenstate and the unperturbed continuum

$$\sigma \propto \frac{\left|\langle\Psi|\hat{d}|g\rangle\right|^2}{\left|\langle\chi_E|\hat{d}|g\rangle\right|^2} = \frac{\left|q^2+\varepsilon\right|^2}{1+\varepsilon^2}. \tag{2.27}$$

with

$$q = \frac{\langle\Phi|\hat{d}|g\rangle}{\pi V_{CI}\ \langle\chi_E|\hat{d}|g\rangle} \quad \text{and} \quad \varepsilon(E) = \frac{E-E_e}{\Gamma/2}. \tag{2.28}$$

Here, q parameterize the asymmetry while the reduced energy $\varepsilon(E)$ describes the detuning from the resonance with the resonance width $\Gamma = 2\pi|V_{CI}|^2$.
The Fano profile is calculated and displayed for a few representative values in figure 2.3(b).

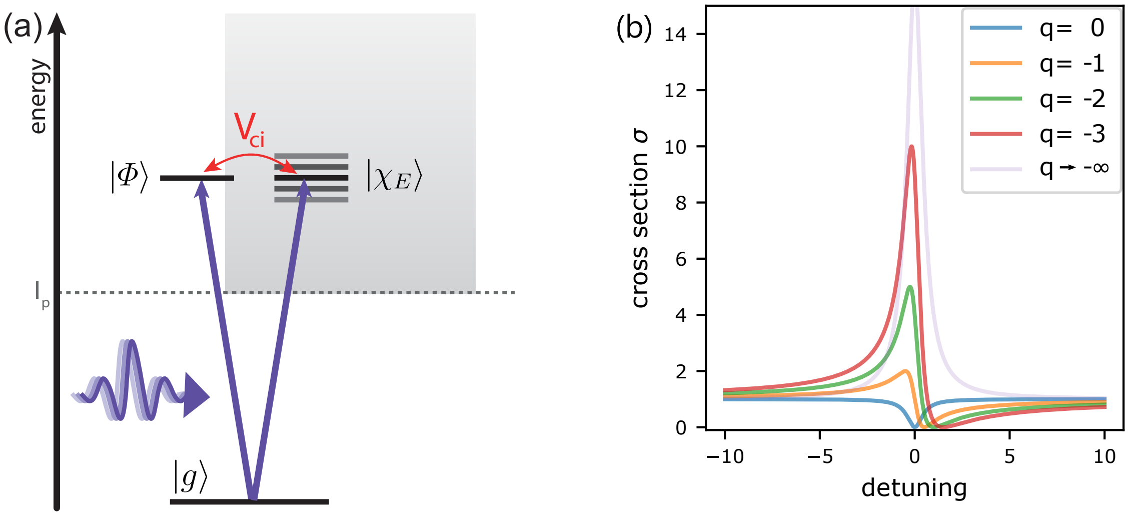

Figure 2.3.: (a) Level diagram of a isolated bound state embedded in the continuum. The transition from the distant bound state $|g\rangle$ to both, the excited embedded state $|\Phi\rangle$ and the continuum state $|\chi\rangle$ form in combination with the continuum interaction V_{CI} a quantum interferometer. **(b)** Fano cross section plotted for indicated values of q. Note, for illustration the $q \to -\infty$ case is normalized to $\sigma = 15$.

A few extreme cases for $q \in (-\infty, \infty)$ in the Fano formula shall be discussed briefly: For $q = 0$ equation 2.28 indicates a suppressed direct path into the bound state. This leads to a cross section of the transition to form the so-called water window, where the value decreases for the energy resonance position. For the case of a vanishing continuum interaction, $V_{CI} \rightarrow 0$ hence $q \rightarrow \pm\infty$, the typical Lorentz lineshape, known from traditional linear spectroscopy of bound states, is reproduced.

In figure 2.3(a) the considered transitions are depicted. While the final state in the continuum can be reached via excitation to the embedded bound state and the continuum interaction V_{CI}, the identical quantum state can be reached via direct ionization. The fact, that two indistinguishable transitions lead to the same final state classifies the considered system as a quantum interferometer.

Fano's original description is limited to weak fields and hence is a time independent treatment. As intense fields lead to dynamics in the system, see previous chapter 2.1.3 a full time-dependent approach is necessary. Such an analytical extension has been formulated by Lambropoulos et al. [14], in principle solving the system for an Hamiltonian constituting of the $\hat{H}_{CI}$ of Fano's formalism added by a time-dependent field interaction in dipole approximation $\hat{d} \cdot F(t)$

$$\hat{H} \; = \; \hat{H}_{CI} + \hat{d} \cdot F(t) \tag{2.29}$$

for which the following solution has been derived:

$$|\Xi\rangle = c_g \; |g\rangle \; + \; \int dE' \; c_{E'}(t) \; |\Psi_{E'}\rangle \tag{2.30}$$

with $|g\rangle$ the ground state and Ψ_E the general eigenstate of Fano's formalism [36]. Thus both states are eigenstates to the strong coupling Hamiltonian $\hat{H}_{CI}$. Since a numeric model will be used in this work the interested reader is referred to [14] for more results of these derivations.

2.3. Transient Absorption Spectroscopy

While so far in the previous chapters the interaction of light and matter was predominantly discussed in terms of the impact of light fields on matter, the action of the perturbed matter back onto the light field comes into the focus now. This builds the foundation for the detection method of absorption spectroscopy.

Joseph von Fraunhofer discovered in 1814 that sunlight dispersed into its frequency components, the colors of the visible spectral range, contains sharp dark gaps in the continues spectrum [37]. Later, Kirchhoff and Bunsen found the relation of absorption lines to specific elements and which can serve as a fingerprint to identify the species of an element [38]. Fraunhofer-style transmission spectroscopy utilizes a light source with a continues spectrum which is transmitted through a target and for analysis spectrally dispersed into it's components. The attenuation of frequency components is mediated by the light-matter interaction of atoms and molecules in the beam path. Hence, on the fundamental level, transmission spectroscopy roots in light-matter interaction. Nowadays, the method is extended since the absorption lines are not just connected to specific atomic or molecular species, but to a certain transitions between energy levels within these targets of interest. Additionally, with modern equipment further dimensions can be added in terms of coherent light sources and non-linear spectroscopy as well as the investigation of temporal aspects and dynamics of atomic systems.

At the heart of the just mentioned light-matter interaction enabling absorption spectroscopy is the manipulation of the electronic wavefunction of the interacting atom, which is based on a quantum mechanical description. The propagation of the wavefunction is the result of the quantum mechanical treatment. With that, the dipole of the atomic system, which is classically defined by $d = -e \cdot r$ with the elementary charge e and the electron position r, is determined following equation 2.4:

$$\langle d \rangle(t) \;=\; \langle \mathbf{\Psi}(t)|\hat{d}|\mathbf{\Psi}(t)\rangle \;=\; \sum_{k,m} c_k(t)\; c_m^*(t)\;\; \langle \varPhi_m|\hat{d}|\varPhi_k\rangle \,. \tag{2.31}$$

An assumption about the interacting target is made to transfer from the microscopic perspective of a single dipole to the macroscopic perspective of the ensemble dipole response: The target systems is dilute and of low particle density. Hence, all particles of the ensemble are exposed and interact with the same electric field, which is not significantly altered by the first targets in the beam path. Also, the interaction of the particles with themselves, e.g. inter-coulombic decay, particular on the time scale of the pulse duration and hence of relevance to the experiment, can be neglected. In consequence, the coherent excitation of all particles can be assumed, allowing the macroscopic polarization to be described in representation by a single particle dipole d and the particle density ρ

$$P(t) \,=\, \rho \cdot \langle d \rangle \, (t). \tag{2.32}$$

Starting form Maxwell's wave equation the field propagation through a medium is shortly discussed here to calculate the transmitted fields. For the simplicity of the derivation, a second assumption is made, which is valid for the experimental application in this work: The electric field $F_0(t,z)\, e^{i(k\,z-\omega\,t)}$ is linear polarized and propagates in z-direction through a homogeneous, non-birefringent medium. The simplified wave equation is given by:

$$\left(\frac{\partial^2}{\partial z^2} \,-\, \frac{1}{c^2}\frac{\partial^2}{\partial t^2}\right) \cdot F_0(t,z)\, e^{i(k\,z-\omega\,t)} = \mu_0 \frac{\partial^2}{\partial t^2} \cdot P_0(t,z)\, e^{i(k\,z-\omega\,t)}. \tag{2.33}$$

The temporal electric field is linked to its spectrum via the Fourier transformation:

$$\begin{aligned} F(\omega) \,&=\, \frac{1}{\sqrt{2\pi}} \int\limits_{-\infty}^{\infty} dt\, F(t) \cdot e^{-i\omega t} \qquad \text{and vice versa} \\ F(t) \,&=\, \frac{1}{\sqrt{2\pi}} \int\limits_{-\infty}^{\infty} d\omega\, F(\omega) \cdot e^{i\omega t} \end{aligned} \tag{2.34}$$

Equation 2.33 can be solved in the spectral domain utilizing slowly varying envelope approximation ($\frac{\partial^2}{\partial z^2} F_0(z) \rightarrow 0$) and the relation:

$$\frac{\partial}{\partial t} F_0(\omega) \,\propto\, \int dt\; e^{i\omega t} \frac{\partial}{\partial t} F_0(t) = i\omega \int dt\; e^{i\omega t} F_0(t) = i\omega F_0(\omega) \tag{2.35}$$

resulting in:

$$\frac{\partial}{\partial z} F(\omega, z) \,=\, i \frac{1}{2\varepsilon_0 c}\, \omega \cdot P(\omega) \tag{2.36}$$

with the natural constants for the speed of light in vacuum c and the the electric permittivity ε_0. As the incoming electric field $F(\omega, z=0)$ propagates through the target medium, the polarization of the combined microscopic dipoles generates and adds an electric field F_+:

$$\begin{aligned} F(\omega, z) &= F(\omega, z=0) + \int_0^L dz' \, \frac{i\,\omega}{2\varepsilon_0\, c}\, \rho_N \, d(\omega) \\ &= F(\omega, 0) + i\frac{\varrho L}{2\varepsilon_0 c}\,\omega\, d(\omega) = F_0(\omega) + iF_+(\omega). \end{aligned} \tag{2.37}$$

with the interaction length L. The spectral amplitude is split in the component of the initial field $F_0(\omega)$ and electric field F_+ generated by and proportional to the dipole. Note the i in the second term, which introduces a $\pi/2$ phase shift in the spectral amplitude. Another $\pi/2$ shift is introduced by the phase difference between the initial external field and the driven dipole analogue to the relation in a driven harmonic oscillator. Thus, in total this adds up to a phase shift of π between the incoming and resonantly generated electric field leading to destructive interference of the fields and the attenuation dip in the absorption spectrum observed by Fraunhofer.

A measure for the absorption is the optical density (OD):

$$OD(\omega) = -\log_{10}\left(\frac{S(\omega)}{S_0(\omega)}\right) \tag{2.38}$$

with $S(\omega) = |F(\omega)|^2$ the transmitted spectral intensity and thus $S_0(\omega)$ the initial spectrum. Hereby, the spectrum of the initial field can either be conducted physically before the light interacts with the target or simply in absence of the target when continuous field properties can be assumed.

For numeric simulations, where the full complex electric field and dipole response are known, the OD (eq. 2.38) can be evaluated with equation 2.37 to

$$OD(\omega) = -\log_{10}\left(\frac{S(\omega)}{S_0(\omega)}\right) = -\log_{10}\left(\frac{|F_0(\omega) + i\,\eta \cdot d(\omega)|^2}{|F_0(\omega)|^2}\right) \tag{2.39}$$

with $\eta = \frac{\rho\, L\, \omega}{2\,\varepsilon_0\, c}$ representing the experimental and natural constants from equation 2.37. Note, that this form is valid while ω can be assumes constant, e.g. for a small laser bandwidth. The interference term in the numerator makes the transmission spectrum sensitive to the phase of the emitted dipole response. In the limit of weak fields this equation describes Beer Lambert's widely known law of absorption. The presented computation of the OD exhibits advantages in comparison to another common representation of the OD

$$OD(\omega) \; = \; \frac{\rho L}{\ln(10)} \frac{\omega}{\varepsilon_0 \, c} \cdot \mathrm{Im}\left(\frac{d(\omega)}{F_0(\omega)} \right) . \tag{2.40}$$

For stochastic electric fields, considered in chapter 5.2, with a spiky spectral intensity, the limit of $F_0 \to 0$ leads to extrem values in the fraction of equation 2.40. This challenge is circumvented with equation 2.39 and an averaging $\langle ... \rangle$ of the fields:

$$OD \; = \; -\log_{10} \left(\frac{\left| \langle F(\omega) + i\,\eta \cdot d(\omega) \rangle \right|^2}{\left| \langle F(\omega) \rangle \right|^2} \right) . \tag{2.41}$$

Lastly, it will be shown how the spectrally measured OD can be used to extract information about the temporal dipole moment of the atom investigated: The temporal evolution of a dipole, which is determined from quantum mechanical calculations with equation 2.31 of a basic excited state in a field free decay, represents an exponentially damped sinusoidal oscillation, see figure 2.4(a). Its spectrum is determined with the Fourier transformation (eq. 2.34). The result within the OD is a Lorentzian line shape. When a phase shift to the decaying dipole response is introduced by a perturbation, it manifests in a distortion of the absorption line shape (fig. 2.4(a)). This line shape can be described with the Fano formula (eq. 2.27), where the Lorentzian represents the limit of $q \to \infty$. For an impulse perturbation of the natural decay, the phase shift in the dipole response relates to the asymmetry change by [25]

$$\varphi(q) = \; 2 \cdot \arg(q - i) \qquad \text{and} \qquad q(\varphi) = \; -\cot(\varphi/2) . \tag{2.42}$$

This relation in combination with respective line shapes is illustrated in figure 2.4(b). With the help of equation 2.42 one can use spectral line shape changes to determine temporal phase shifts of the decaying dipole moment. A good review on the entire topic is [39].

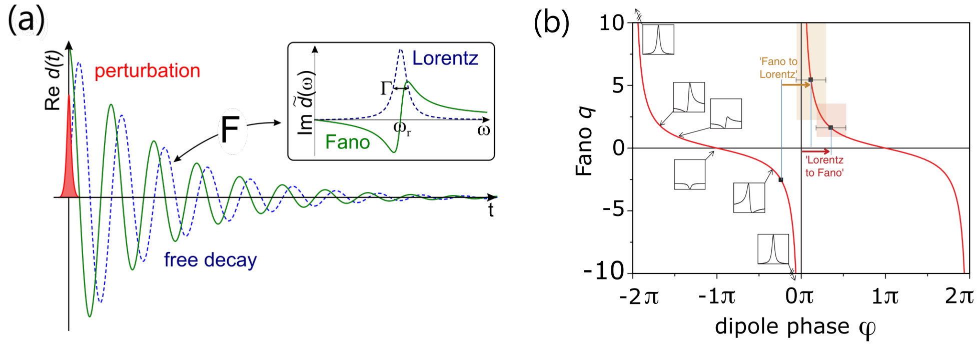

Figure 2.4.: **(a)** Temporal evolution of a field-free decaying dipole and its spectrum (inset) illustrating the impact of a ultrashort perturbation on both quantities, adapted from [27] **(b)** Illustration of the relation in equation 2.42 between the phase shift of the decaying dipole and its absorption line symmetry, adapted from [25].

2.4. The Atomic Target Helium

The goal of this work is to investigate the behavior and dynamics of a two-electron transition in near resonant, intense electric laser fields. Helium is the most basic atomic system containing two bound electrons in its neutral ground state with the electron configuration $1s^2$. As a noble gas its natural occurrence is in atomic form versus the molecular appearance of e.g. hydrogen in H_2.

Helium has been experimentally well characterized by synchrotron measurements [40–43]. Single-electron extinctions lie below the single ionization potential of 24.59 eV. Multiple series of two-electron resonances start at about 60 eV (fig. 2.5(a)). The energetically lowest is the $1s^2 \rightarrow 2s2p$ transition ($^1S^e \rightarrow {}^1P^o$) at 60.15 eV [40]. Its resonance is spectrally isolated from the energetically subsequent resonances and thus an ideal candidate to investigate new effects and subject to this work. Excited by one near resonant photon, both electrons are excited under the exchange of the photon energy, while the angular momentum is absorbed by just one of the electrons. This requires electron-electron interaction which makes these two-electron transitions subjects of general interest. As the state lies above the single ionization continuum it is an autoionizing bound state embedded in the continuum. The theory for such a quantum state has been treated by Fano, see chapter 2.2. Therefore, the absorption lines of the two-electron resonances in figure 2.5(a) exhibit the typical Fano line shape (fig. 2.3). The state decays after a lifetime of 17 fs into the ionic ground state (n=1) of He^+, [21]. Its line width has been characterized to 37 meV [40] while the asymmetry q-parameter has been determined to $q = -2.75$ [40].
With the second channel of the direct ionization into the same final state of He^+ figure

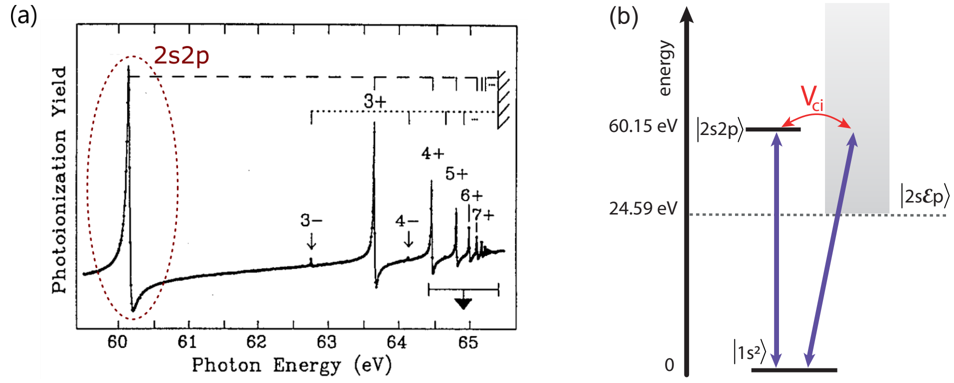

Figure 2.5.: **(a)** Synchrotron measurement of the He 2snp series [40], **(b)** Level diagram of the helium 2s2p resonance, showing the coupling of the ground state to the bound 2s2p state and the single ionization continuum with an XUV field (violet). The bound state is directly coupled to the continuum by the configuration interaction V_{Ci}.

2.5(b) illustrates the association of the resonance with a "quantum interferometer". Its key feature, the sensitivity to phase, allows for the detection of perturbations of the excited state and its transition from the ground state (eq. 2.27). These manifest in a change of the absorption line as discussed in chapter 2.2 in context of Fano's theory and the previous chapter 2.3.
Therefore, the two-electron state in helium has been subject to extensive studies [10]. The resonance has been investigated in the presence of strong fields both, theoretically [13–16] as well as experimentally with electron spectroscopy [21–23] and with TAS [24–30]. In particular the temporal build up of the absorption line has been observed recently [22, 29].

In the context of this thesis, the absorption line of the helium 2s2p state is quantified by the fit with an adjusted Fano formula (eq. 2.27):

$$OD(\omega) = \frac{a}{1+q^2} \cdot \left(\frac{(q+\varepsilon(\omega))^2}{1+\varepsilon^2(\omega)} - 1 \right) - b \qquad \text{with} \qquad \varepsilon(\omega) = \frac{\omega - \omega_r}{\Gamma/2}. \quad (2.43)$$

The off-resonant offset ($=1$) is subtracted. Furthermore, the equation normalized by $1+q^2$, compared the original formula. This prevents the peak of the line shape in the limes of the Lorentzian line shape ($q \to \pm\infty$) from reaching extreme values on resonance ($\omega = \omega_r \Rightarrow$ reduced energy $\varepsilon(\omega) = 0$). Therefore, the quantification of the line strength a is decoupled from the line shapes asymmetry. The off-resonant linear-absorption background is quantified by b, while the line width is determined by Γ.

2.5. High-Energy Photon Sources

2.5.1. XUV and Soft X-Ray Light

To perform experiments with light atoms on inner-shell resonances photon energies in the XUV (extreme ultraviolet) and soft x-ray (SXR) regime are necessary. The XUV spectral range ($\sim$10 - 120 eV) entails some additional demands, which are not present in the visible spectral region. Short wavelengths (10 nm regime) experience in principle a high absorbance in matter, including the molecules constituting the atmosphere. As a result, the transmission and beam distribution of XUV pulses have to be conducted in evacuated volumes. A pressure on the order of 10^{-6} mbar or better can be required depending on the photon energy and the experimental conditions. An additional peculiarity of the sub-100 eV photon-energy regime is the lack of ordinary transmission optics commonly employed in the VIS und IR spectral regime. This is due to the low refractive index at these frequencies in combination with the just mentioned absorbance of short electromagnetic wavelengths on small length scales in solid materials. As a result, most optics used in such experiments are **reflective optics**, either under a very small angle of incidence, in so-called **gracing incidence**, or under larger angles of incidence but with a certain bandwidth in the form of specially coated multi-layer optics. Both of the described properties influence the concept and design of high-energy photon sources.

2.5.2. The Free-Electron Laser

The exploration of light-matter interaction at high field strengths requires light sources of high brilliance. The first FEL was build 1970 by Madey *et al.* at Stanford University [44–46], though it played no significant role in the presence of conventional quantum lasers in the IR and VIS spectral regime. These conventional laser are limited to lower photon-energy regions, namely IR, VIS and ultraviolet (UV) and thus cannot reach the XUV or SXR. In abstract terms, a conventional quantum laser consists of an active medium located in a cavity. The medium is externally pumped with energy and couples it to the coherent photon beam via stimulated emission. The lack of optics with sufficient reflectivity at normal incidence prevented the extension of this concept to wavelength below 100 nm [47]. The initial interest in the XUV and SXR spectral region was covered by high-order-harmonic generation and synchrotron sources for many experiments [48, 49]. In scientific areas where these sources could not provide sufficient brilliance, FELs offered an access to this XUV regime. Due to their working principle, XUV and SXR FEL pulses are inherently in the femtosecond regime.

In an FEL the pump energy is delivered in from of kinetic energy of a relativistic accelerated electron cloud and transferred to the electro-magnetic fields via their sinusoidal motion in magnetic fields. The basic of this concept, particularly the transfer of energy to high brilliance radiation, is described in the following. For information beyond the scope of this section, the reader is referred to [47, 50], which is used as an orientation for the presented content.

Schematically, an FEL constitutes of three major parts: The *electron gun* generates free electrons, which are accelerated close to the speed of light in a linear, in many cases superconductive and cavity-based [47], *accelerator*. This relativistic electron bunch then propagates through an *undulator*, consisting of alternatingly oriented magnets. Here, the electromagnetic waves are generated by the sinusoidal motion that the magnetic fields force the electron bunch to perform.

In general an accelerated charge emits radiation, called *bremsstrahlung*. When an electron trajectory is bent with an magnet by the *Lorentz force*

$$-e \cdot \mathbf{v} \times \mathbf{B} = m_e \cdot \gamma \frac{\partial \mathbf{v}}{\partial t} \tag{2.44}$$

the radiation, in particular its power per angle, is described by the *Larmor formula*

$$\frac{dP}{d\Omega} = \frac{e^2}{16\pi^2 \varepsilon_0 m_0^2 c^3} \left(\frac{dp}{dt}\right)^2 \cdot \sin^2 \Theta. \tag{2.45}$$

When this bending is repeated periodically in alternating order with respectively oriented magnets, it forces the electron on a sinusoidal trajectory (fig. 2.6). Depending on the amplitude of that oscillation, the motion is characterized as a wiggle or undulator motion. The basic difference is, that in a wiggler, the radiation of each single electron does not add up coherently. Meanwhile, such a condition can be found in an undulator, which is treated in the following. Since the Lamor formula describes the oscillation of a dipole in the non-relativistic case, the dipole radiation (eq. 2.45) is calculated in the rest frame of the electron on the undulator axis. The resulting radiation profile (fig. 2.7 left) is transferred back via the Lorentz transformation into the laboratory frame (fig. 2.7 right). The majority of the power is emitted in forward direction along the undulator axis.

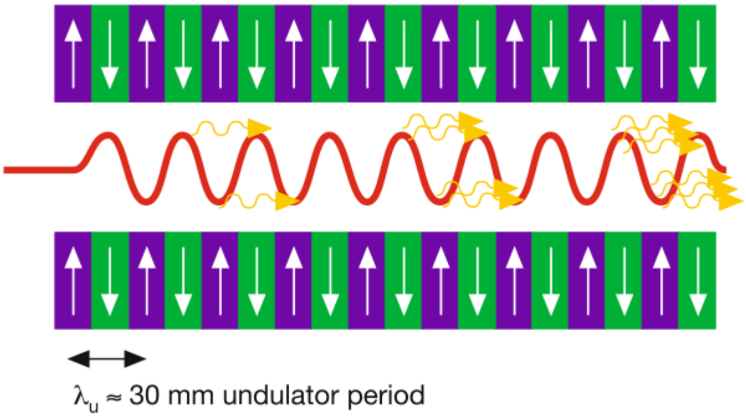

Figure 2.6.: Schematic principle of an FEL undulator with alternating polarized magnets (green, violett) and the undulator motion of the electron beam (red) emitting photons in forward direction (yellow). From [47].

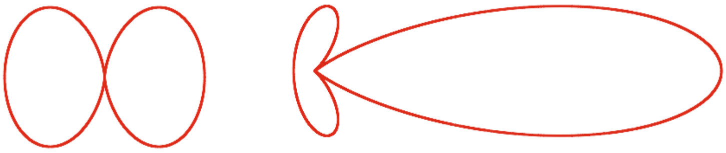

Figure 2.7.: Schematic of a Hertzian dipole emission, (left) in the moving frame, (right) viewed in the rest frame, illustrating the emission by relativistic electrons in an undolator in forward direction. From [47].

The period of the magnetic field λ_u seen by a relativistic electron due to the length contraction computes to

$$\lambda_u^* = \frac{\lambda_u}{\gamma} \tag{2.46}$$

with the *Lortenz factor* $\gamma = \left(1 - \frac{v^2}{c^2}\right)^{-\frac{1}{2}}$.
Considering the Doppler effect and performing a few calculations [47], the wavelength of the emitted radiation computes to

$$\lambda_l = \frac{\lambda_u}{2\gamma^2}\left(1 + \frac{K^2}{2}\right) \tag{2.47}$$

with the *undulator parameter*

$$K = \frac{e\, B_0\, \lambda_u}{m_e\, c\, 2\pi}. \tag{2.48}$$

In essence, the emitted wavelength can hence be adjust with the kinetic energy E_{kin} of the electrons via v in γ, with the undulator period λ_u and magnetic field strength

B via K. Thus, with a fixed-gap undulator, as it is the case for the light source used in the experiments at the center of this work, the emitted photon energy can only be tuned by the amount of electron acceleration.
The undulator parameter represents the properties of the magnetic device: For $K < 1$ the electron motion keeps overlapping with the emitted light field, the emission profile is a small cone and the motion is called undulator motion. For $K > 1$ this motion exceeds the overlap and is called wiggling motion.
So far, the model has described the field emission of one electron. For high intensities an entire electron cloud, which can extend over multiple magnet periods, is sent through the undulator. This leads to the incoherent accumulation of fields from every part of the electron bunch on the undulator axis. To enable a coherent build-up resulting in a high intensity, the electron cloud needs to be bunched into small segments, spaced by a certain distance to meet a phase-matching condition. This bunching can either be achieved by an external XUV/SXR source - a method called seeding - or by a spontaneous process called self-amplified spontaneous emission (SASE), which is explained in the following.

The electron bunch can exhibit an inhomogeneous density. The initially generated light emitted by a particular dense part can achieve comparatively higher field strengths and hence dominate the interaction of the light field back onto the electron cloud. Assuming a plane wave $F(t)$ with a constant envelope as the initial electric field in the undulator, the energy transfer between the electric field and the electron bunch is described by

$$\frac{dW}{dt} = \mathbf{v} \cdot \mathbf{F} = -e \cdot v_x(t)\, F_x(t). \tag{2.49}$$

One can conclude from the scalar product, that the largest energy exchange takes place when the polarization of the electric field and the electron motion are in the same plane. Furthermore, it is highest within an oscillation period, when the velocity component of the electron is close to parallel to the electric field. This is the case for the nodes of the periodic electron motion and peaks of the electric field. Thus no energy is transferred in the extreme points of the periodic electron trajectory. The energy transfer goes both ways: For $\frac{dW}{dt} < 0$ energy is transferred into the electric field and thus the vectors in 2.49 point in the same direction. Meanwhile, for $\frac{dW}{dt} > 0$ and an opposite direction of the electric field and electron motion the energy is transferred towards the kinetic energy of the electrons in the bunch. This modification of the electrons' kinetic energy leads to a modulation in their density within the electron cloud. It results in a bunching of the cloud into smaller micro bunches.

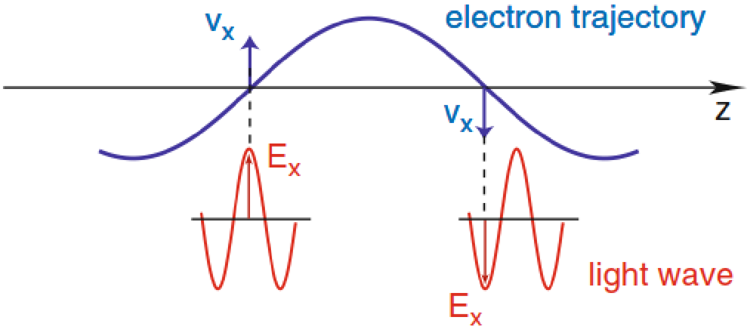

Figure 2.8.: Energy transfer between the relativistic electrons (blue) and an initial electric field present in the undulator (red), illustrating the phase-matching condition. From [47].

For highest intensities and thus a coherent superposition of the contributions from different micro bunches, their spacing has to fulfill a phase matching condition: While an electron travels half an undulator period $\lambda_u/2$, the field propagates the same distance with an equivalent phase evolution of π (see fig. 2.8):

$$\frac{\lambda_u}{2}\frac{1}{\bar{v}_z} = \frac{\lambda_u}{2}\frac{1}{c} + \frac{T_{ph}}{2} = \frac{1}{2c}\left(\lambda_u + \lambda_{ph}\right). \tag{2.50}$$

This condition is met by

$$\lambda_{ph} = \frac{\lambda_u}{2\gamma^2}\left(1 + \frac{K^2}{2}\right) \tag{2.51}$$

as well as for every odd harmonic of λ_{ph}, $\lambda^*_{ph} = \frac{\lambda_{ph}}{2m+1}$. Note that this equation is equivalent to 2.47, meaning that initially generated light emitted by parts of the electron bunch can seed the FEL. This leads to a self organization by micro bunching and enhancement of the electro-magnetic field. Since the seeding photons of the organizing process originate from stochastic, spontaneous emission, it is named self-amplified spontaneous emission. The output pulse energy of an FEL increases with the distance traveled through an undulator until the micro bunches are well defined in segments, smaller than the undulator wavelength. At that point the nonlinear gain saturates, see figure 2.9. The output power of such a high-gain FEL scales with $P \propto N_e^2$ compared to the incoherent add up of $P \propto N_e$ typically observed in synchrotron sources.

As mentioned above, the micro bunching can also be achieved by seeding the FEL with external source. Here, the electron bunch is modulated with XUV fields of the desired frequency with a typically narrow-bandwidth spectrum. In many cases the seed is generated by an high-order-harmonic-generation process [51].

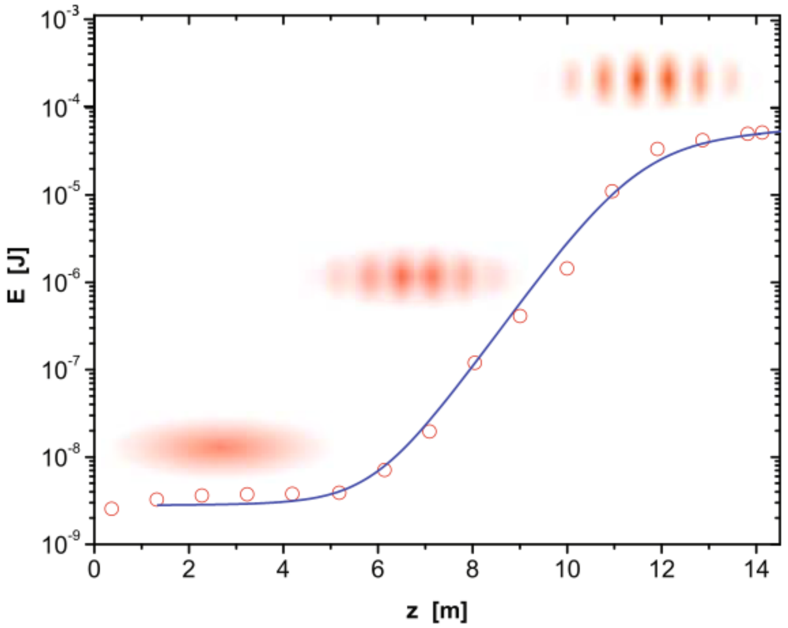

Figure 2.9.: Gain curve (photon pulse energy in logarithmic scale over undulator length) of a high-gain FEL. After the electron bunch reaches complete micro bunching the non-linear gain saturates and further gain is only added by the electrons performing the undulating motion. From [47].

Seeded FELs exhibit a well defined temporal and spectral structure [52] compared to SASE FELs, where the stochastic nature is not limited to the spectral and temporal envelope and phase, but extends to further parameters (subject of chapter 4).
For completeness, a third version, a so-called self-seeded FEL [53], is mentioned here, which combines both of the above. In that case, a monochromator for the electric fields is placed after a first section of the undulator. Its transmitted light seeds the remaining undulator sections.

The process of micro bunching allows for sufficient gain within a single pass through the undulator section. It is hence possible to use high electron charge densities, which lead to the high peak intensities of so-called high-gain FELs. This is neither possible for low-gain, cavity-based FELs in the VIS or IR regime, nor for synchrotrons. In both cases the electron bunch is utilized multiple times. Here, though, the Coulomb repulsion of the electrons leads to an elongation of the electron cloud and prevents ultrashort and thus highly intense and brilliant pulses.

3. Experimental Setup

For the explorations at the center of the work, experimental measurements are conducted at the Free-Electron Laser in Hamburg (FLASH). Two experiments have been performed at separate measurement campaigns.
To explore high intensity effects in helium, an XUV beam is focused into a small volume filled with the target gas (fig. 3.1). The transmitted beam is dispersed by a reflective grating and the absorption spectra recorded. One of the major tuning parameters at the experiments is the pulse energy. XUV pulses generated by FLASH are therefore attenuated with an adjustable gas attenuator. The pulse energy is measured before and after the attenuator. To determine the exact spectral absorbance of the target while utilizing stochastic pulses, an parasitic reference spectrometer records spectra without absorption before the target for every pulse.
The subject of this chapter is a detailed description of the devices used in the experiments as outlined in the paragraph above. After a short introduction of the particularities of experiments in the XUV spectral region, the parameters of the light source FLASH are characterized. This is followed by a portrayal of the facility-based devices utilized in the experiments. In the second part, the home-built vacuum beamline (BL) is presented with its key elements crucial for the experiments.

In general, the photon-energy regime of XUV and SXR comes with constraints to the experimental setup, separating it from the approach viable in the VIS and IR spectral regime. As explained in chapter 2.1 and 2.4, light-matter interaction with XUV photons leads to many processes within the electronic structure of an atomic system, as the photon's energy reaches up to inner-shell interactions. In consequence, the XUV spectral region is subject to significant absorption by nitrogen and oxygen, requiring the transport and propagation path of the XUV beam to be evacuated from atmosphere. Therefore, the entire setup, including the facility-based beam distribution and FLASH itself, is built in and consists of vacuum chambers. The requirement for the vacuum in the section of the BL is in the lower 10^{-6} mbar regime, as the observable

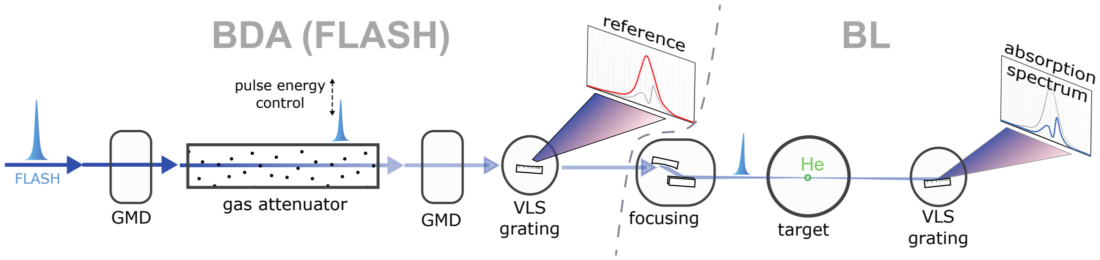

Figure 3.1.: Schematic setup of the experiment at the center of this work. The graphic is split into the facility based section as part of FLASH's beam-distribution array (BDA) and the part of the home-build beamline (BL). The devices are explained in the course of this chapter, including the gas-monitor detectors (GMDs) and the variable line-space (VLS) grating.

of the experiments discussed here are XUV absorption spectra. Increased requirements to the vacuum exist for long distance beam guidance, e.g. in the beam-distribution array over several 10 m, as well as for the utilization of charged particles. The latter are disrupted by residual atmosphere, as they possess an even higher interaction cross section in form of scattering or charge-capture than XUV photons. Affected are the FEL itself, with its accelerated electrons, as well as measurement methods involving charged particles, e.g. electron spectroscopy.

As discussed in chapter 2.5.2, another peculiarity of the XUV and SXR photon-energy region is the spectrum of available optics. Thick transmission optics widely used in the VIS and IR spectral regime are not an option due to the refractive indices close to one as well as the already mentioned high absorption. While diffractive transmission optics provide an alternative with an inherently low transmission, reflective optics present the most practical solution and are widely employed. Dielectric multi-layer optics are utilized under normal incidence. Since their reflective spectral bandwidth is small, their usage limits the possibility for wide wavelength tunability. Metal mirrors (gold, silver, nickel), as well as other coatings (e.g. carbon) provide high reflectivity in the XUV and SXR regime, when utilized under grazing incidence with angles smaller than ten degree to the plane of the optics. Despite their rather large proportions in the dimension along the beam axis, they proved to be the most usable optics and are thus employed in the BL as well as in many positions along the beam path at FLASH.

3.1. Free-Electron Laser in Hamburg

While the general concept of an FEL has been covered in chapter 2.5.2, FLASH and its parameters are shortly presented in the following. In particular the parameters

that FLASH is adjusted to during the experiments and its principle capabilities are set in comparison. The documented values originate from [54] as well as [55].
FLASH is a SASE-based XUV source of high brilliance and with stochastic, temporally partially coherent pulses. As can be seen in figure 3.2, the facility recently gained a second undulator path called FLASH 2. The here presented experiments have been conducted at the fixed-gap undulator noted as FLASH 1 in the figure. Therefore, in the context of this work the combination of the upstream FEL sections and the FLASH 1 undulator is simply referred to as FLASH. It presents the ideal candidate for the unique demands created by the explorations of this thesis, namely a high pulse energy of several µJ at a photon energy of 60 eV with a broad relative bandwidth of about 1% and a short pulse duration of about 100 fs at an open-port beamline. A neutral-density attenuator as well as the parasitic reference spectrometer, both also essential for the presented experiments and discussed in the subsequent sections, are available. Operational since 2005 FLASH reached an at that time new regime of coherent peak and average powers in the XUV spectral region [31]. It is able of delivering pulse trains, grouping up to 800 pulses with microsecond spacing which burst at a 10 Hz rate. While that is ideal for experiments demanding high statistics, the here described TAS experiment only uses a single pulse per 10 Hz window. This retains the ability of recording the spectra for every pulse individually, as will be further elaborated on in chapter 4. The central photon energy is set to 60 eV, equivalent to 20.66 nm, well within the range of the fundamental wavelength 6.9–47 nm. The same holds true for the relative bandwidth, which is at 0.7% (0.4 eV at 60 eV) well within the range of 0.5–1%. The pulse duration, which is at present between 30 fs - 200 fs, is also entangled with the demanded pulse energy. Average pulse energies of 60 µJ with peak energies above 80 µJ have been recorded during the measurements (see next section, ch. 3.2). The pulse duration is derived from the electron bunch length measurement, a so-called LOLA measurement [56, 57]. With no direct photon measurement available at the facility during the campaign LOLA-measurement results serve as a good estimate. Values of 75 fs and about 100 fs have been determined for the two measurements.

3.2. XUV Processing and Characterization

The subject of this section are the FLASH-facility-based devices. The beam-distribution array (BDA) guides the XUV pulses in vacuum tubes from the undulator to the

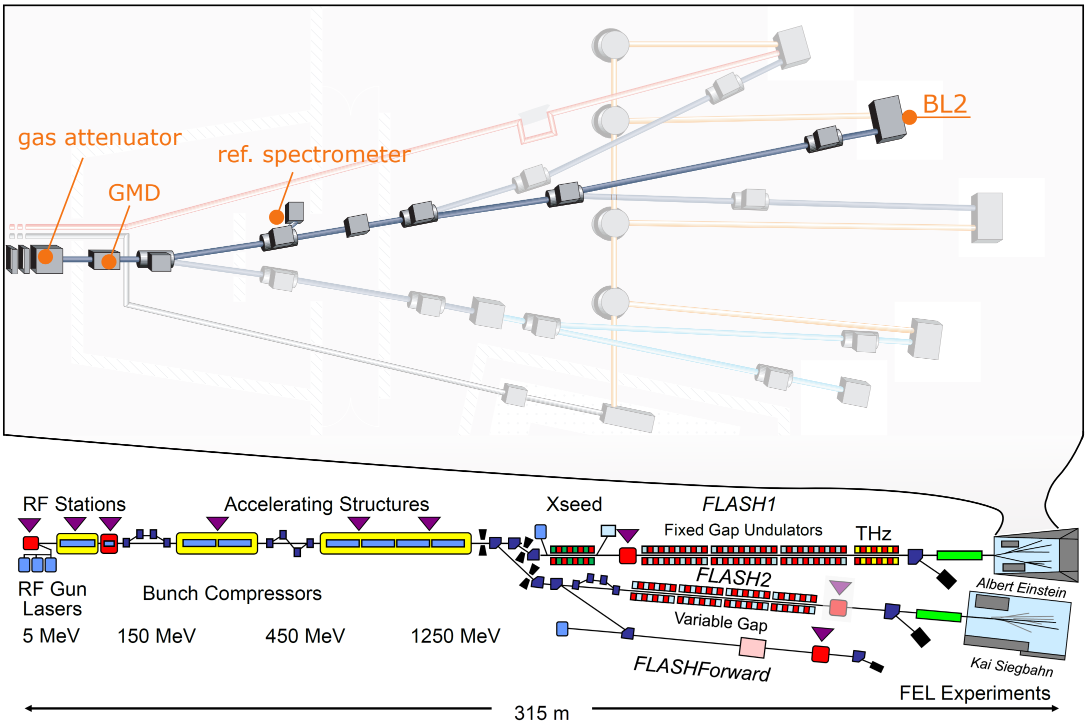

Figure 3.2.: Sketch of the FLASH facility, bottom: Overview over the sections of FLASH itself, including FLASH1 (abbreviated as FLASH in this thesis) and the recent extension FLASH2. Top: Magnification of the experimental hall displaying the BDA and the components discussed in the following, the reference spectrometer, GMD, gas attenuator and the open port BL2. Figures adapted from [54](top) and [58](bottom).

available endstations, see figure 3.2 top. It contains several devices that enable the characterization (reference spectrometer, gas monitor detector) and the manipulation (gas attenuator, apertures, thin metal attenuation filters) of the photon beam.

Pulse-Energy Measurement and Adjustment

For the exploration of intensity-dependent effects a precise knowledge of the pulse energy is required. The stochastic nature of SASE-based XUV sources causes strong fluctuations in the pulse energy as well (fig 3.3). Hence, a single-pulse energy measurement is essential for assigning the energy to the individual pulses. An intensity measurement, requiring access to the peaks within the temporal structure of the pulse, carries many advantages. It allows for the direct observation of intensity related effects by selection and sorting this parameter. Such a device is challenging to realize for short pulse durations of about 100 fs and the even shorter intra-pulse intensity spikes and is not offered as a parasitic photon diagnostic at the facility. Therefore, so-called gas-monitor detectors (GMDs) measure the temporal integrated pulse energy for each pulse [54, 59]. Their working principle is based on a dilute gas with spectrally neutral density, which is ionized by each XUV pulse. The created free charged particles are detected by Faraday cups and the measured current is proportional to the number of photons in the pulse:

$$N_{ions} = N_{photons} \cdot \sigma_{ionization} \cdot \rho_{taget\,gas} \cdot l_{interaction} \tag{3.1}$$

with N being the number of ions and photons respectively, σ the ionization cross section of the detecting gas species and $\rho \cdot l$ the path-length-density product representing the gas density and the interaction length in the device. The pulse energy can be determined with a precision of about 10% [54]. Additionally, such a device is also able to monitor the beam position parasitically. A typical pulse-energy measurement of single XUV pulses (fig. 3.3, in blue) shows the broadly scattered values on the order of 40 µJ full width at half maximum (FWHM).

To facilitate measurements across the full pulse-energy range and achieve sufficient statistic, particularly in the lower pulse-energy section, this parameter is tuned. FLASH could be adjusted to reach this goal, but this would have implications on the FEL stability as well as on the remaining pulse parameters, e.g. pulse duration, spectral distribution and beam alignment. Instead, the pulse energy is adjusted by tuning the overall intensity with a *gas attenuator* [54] as a more subtle approach.

This several meter long tube is filled with a gas species of neutral density in the spectral region of interest. Molecular nitrogen serves as the absorber at a pressure up to 0.1 mbar for measurements at about 60 eV considered in this work.

Reference Spectrometer

Reference spectra are required for the calculation of the OD (ch. 2.3, in particular eq. 2.38). As mentioned in that chapter, this can be achieved by a reference measurement without a target in the beam path. For a stochastic source like FLASH, a single-shot based, parasitic reference measurement reaches better results. The facility-based 'online' spectrometer utilized for this purpose possesses the same working principle as the main spectrometer. This will be described in detail in the following chapter 3.3, including example spectra of the FEL. For the calculation of the OD (eq. 2.38) the reference spectrometer is mapped to the main spectrometer in chapter 4.2. Further information specific to this spectrometer and beyond the treatment of the main

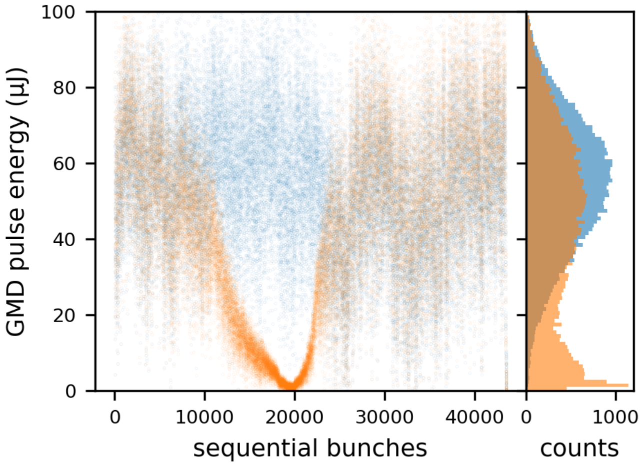

Figure 3.3.: Pulse energy measurement during the experiment displaying the naturally broad distribution of the parameter. The pulses measured before the gas attenuator exhibit a normal distribution (blue), while the pulse energy measured after the attenuator (orange) shows the impact of the cycled gas attenuator. The histogram illustrates the pulse energy probability and hence underlines the effect of the gas attenuator.

spectrometer can be found in [60].

3.3. Vacuum Beamline

The vacuum beamline (BL) for the experiments described in this work has been newly built for both, lab- and facility-based experiments. It is utilized for high-harmonic generation based attosecond transient absorption spectroscopy experiments [61, 62] at the MPIK, while for the time of the here considered experiments it is transported to FLASH. Therefore, the entire BL is constructed and optimized for portability and flexibility, enabling a compact transition between the locations of the laboratory and facility-based experiments. Furthermore, speed and precision in daily routines have been taken into account during the design process to allow an efficient use of the precious time during an FEL campaign. This is realized in form of fast and encoder-based motorized stages and fast-access flanges for sections with high maintenance demands. While photographs of the setup can be found in the appendix, this work will concentrate, though, on the scientific case rather than the technical details. The following sections provide the principal concepts crucial for the understanding of the experiments. An overview of the BL is provided in form of a rendering in figure 3.4. The home-built setup is connected to the open-port beamline BL2 at the BDA of

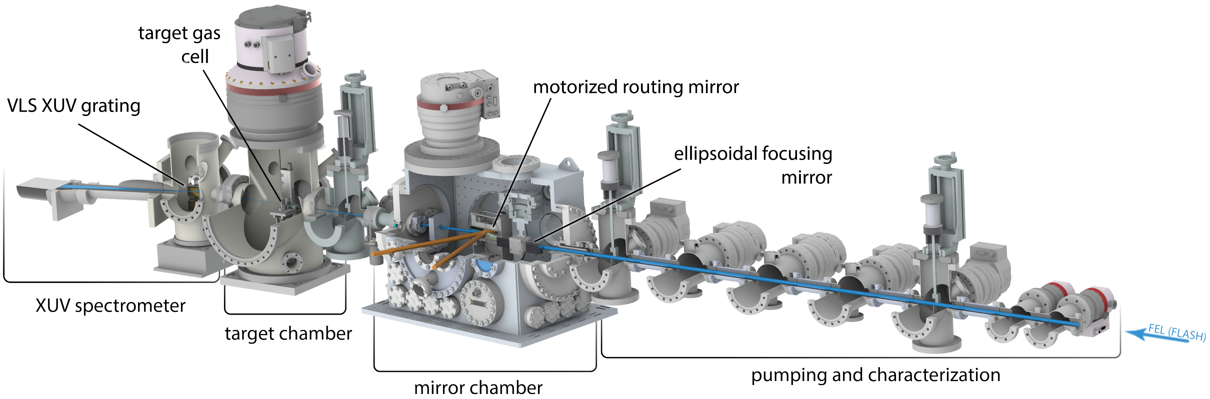

Figure 3.4.: Rendering of the beamline utilized in the second measurement campaign. Photos of setup as well as the beamline utilized in the first measurement campaign can be found in the appendix.

FLASH. Over several measurement campaigns the setup design has been subject to minor adaptations. The two campaigns are referred to as the *first* and the *second* campaign in the following. In principle, the BL can be split into three compartments with relevance to this work: The *focusing*, the *target*, and the *spectrometer* section.

The first chambers of the BL (fig. 3.4) connected to the open port BL2 comprise multiple differential pumping stages to protect the pressure in the BDA and FLASH, even when the experiment works with higher target gas pressures in the BL. Additionally, these chambers contain diagnostic screens, pinholes and filters for the alignment of the beam and the BL (in respect to FLASH). This is critical for the propagation of the beam through the entire BL up to the spectrometer.

Focusing

The focusing optic focuses the beam and its energy into a small spot to achieve highest field intensities. In the first measurement campaign, the facility-based focusing optic of BL2 is utilized, which is localized in the BDA shortly before the BL2 port. The ellipsoidal mirror focuses the beam 2 m to a spot size of about 25 µm FWHM at a 3° angle of incidence with an reflectivity of 93% [63, 64]. The target cell is placed in the focus of the beam. Afterwards, the transmitted beam is propagated through the remaining sections of the BL and is coupled into the spectrometer.
At the second campaign, the BDA transmits an unfocused ∼7 mm diameter beam [63]. This time, the XUV pulses are focused by an off-axis ellipsoid mirror [65] located in the BL under an 8° angle of incidence. A shorter focal length of 1 m leads to a spot size of about 5 µm ($1/e^2$). Since this mirror is part of the portable beamline, it does

not have the advantage of an stationary optic. Thus, an alignment procedure has to be performed at the beginning of every shift. A Hartmann-plate-based, XUV-optimized wavefront sensor is used for this purpose [66, 67], measuring the beam directly reflected off the focusing optic. The alignment and optimization procedure has been described in literature and can be found among others in [68, 69]. Once optimized, the beam is guided back onto the target volume by a motorized plane mirror, also at 8° angle of incidence.

In both campaigns, the ellipsoid mirror images the SASE pulses from the 85 m distant source point in the undulator onto the target volume in the BL. The high reflectivity is achieved by the small angle of incidence and the coating with layers of carbon. This is crucial particularly for all optics along the beam path in front of the target cell, to achieve highest field strength in the target.

Target Cell

The target cell provides the target, in this case helium, in the gas phase. It is located within the target chamber in the focus of the beam for highest intensity. The cell is manufactured of stainless steel and has an inner diameter of 2 mm, with two openings of 100 µm diameter aligned on an axis for the beam to propagate through the target.

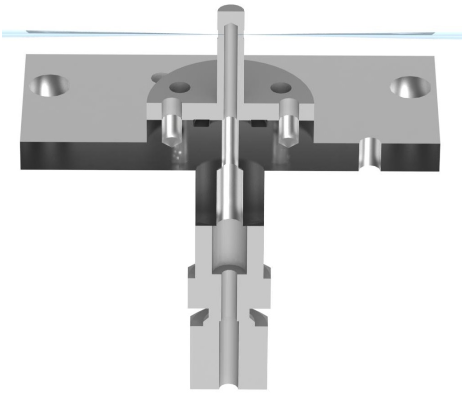

Figure 3.5.: The target cell (rendering, cut open and with illustrated beam), a stainless steel cell on a carrier-stage mount provides the gas target from a feeding line connected below.

The interaction length of the target with the beam is estimated to about 3 mm, which derives from the inner diameter and the 1 mm wall thickness of the cell at a decreasing gas pressure due to the vacuum in the chamber. The interaction region is constantly flushed with target gas through a flexible stainless-steel tube. It provides a constant but adjustable backing pressure, which is set to about 100 mbar and finetuned in such a way that the OD reaches a maximum value of one.

The target cell is mounted on a fast (20 mm/s) and precise close-loop (µm repeatability) slip-stick piezo stage [70], which enables a quick and efficient alignment of the cell as well as scans in the spatial dimensions, e.g. to determine the exact position of the focus on the lateral axis.

Note that the pulse energy in the target volume is at about 50% of the GMD measured pulse energy. The lower effective pulse energy originates from losses in the BL and BDA photon transmission. In this thesis the pulse energy will be quantified as measured by the GMD.

Spectrometer

The spectrometer can be understood as an imaging optic, projecting an initial source point spectrally dispersed onto an imaging screen. It constitutes of three main elements at the beamline: The entrance point, the dispersive optic and the device recording the dispersed spectrum (fig. 3.6). Ideally, the *entrance point* concurs spatially with the focus in a target volume. This has been the case in the second campaign. For technical reasons in the first campaign, the focus in the target has been refocused and the beam propagated through additional chambers of the beamline. It has then been coupled into the spectrometer with a motorized slit aperture located at the entrance point.

The *dispersive optic* is a prism in most ordinary cases in the VIS spectral regime. Here, it is realized in form of a gold-coated reflective grating [71] where the zeroth order is dumped while the first order is propagated onto the recording device. The utilized grating contains two particular properties. First, to work as an imaging optic in the spectral domain, projecting a point source of one wavelength from the entrance point onto one point on the imaging plane, the substrate is curved. It therefore acts as a cylindrical lens focusing the light in one dimension while the other axis remains unaltered. Here, the spectral dimension is oriented horizontally (fig. 3.6). The device is hence suitable to be employed as a spectrograph. Secondly, the grating is a variable line-space grating (VLS) [72], meaning that the spacing of the lines imprinted on its surface to disperse the light via interference is not equidistant. An ordinary grating with equidistant lines focuses the frequency components on the so-called Rowland circle or respectively cylinder [73, 74]. In case of a planar recording device, which can furthermore move along the spectral axis, this would cause parts of the measured spectrum to be out of focus and thus lead to a non-constant and decreasing spectral resolution. The variable line spacing compensates that and focuses all wavelength in the specified spectral region on a straight line. This leads to a complex and costly manufacturing of the dispersive component but enables a spectral resolution that can not be attained otherwise.

Note that the reference spectrometer works analogously with the distinction that the

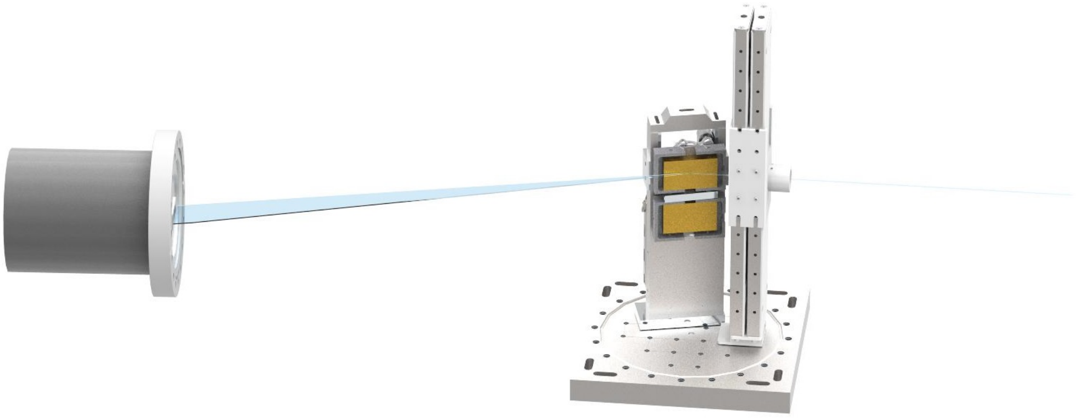

Figure 3.6.: Spectrometer (rendering, without vacuum housing). The beam is coupled in from the right side, attenuated by the double filter array and dispersed by the VLS grating onto the XUV camera. The filter array and grating holder each provide multiple slots for flexible application in terms of variation or backup.

substrate is plane. Here, the zeroth order is propagated as the main beam to the experiment and needs to remain unaltered. The focusing is thus achieved by a more advanced ruling of the lines [60].

For the acquisition of the spectra a *recording device* is placed in the focus plane. This camera [75] possesses a back-illuminated, XUV-sensitive CCD chip, recording the spectrally dispersed photons in one spectral and one spatial dimension. With a chip size of 1340x400 pixel with 20 µm per pixel, the camera allows for a fine sampling of a broad spectral range from the first diffraction order. The 60 eV central photon energy at the experiments is well within the specified range of 10 eV and 30 keV. The spectrometer resolution is determined in chapter 4.2. It ranges between 60 meV and 40 meV for the first and second campaign respectively. As mentioned above, the discrepancy is mostly caused by the different kind of spectrometer incoupling.

During the experiment, the region of interest in the spatial dimension on the CCD chip is limited to the beam profile. The image is then binned along that axis to maximize the signal-to-noise ratio. To protect the CCD chip from saturation and damage, a multi-layer filter array with thin aluminum filters between 0.2 µm and 6 µm thickness is located in the spectrometer chamber to adjust the transmitted intensity. The spectrum acquisition timing is set to a short window of 10 ms synchronized with the 10 Hz repetition rate by a basic trigger signal. The acquisition time fully incorporates pulses of 100 fs duration and any jitter of the pulse arrival. Figure 3.7 shows representative single pulse spectra.

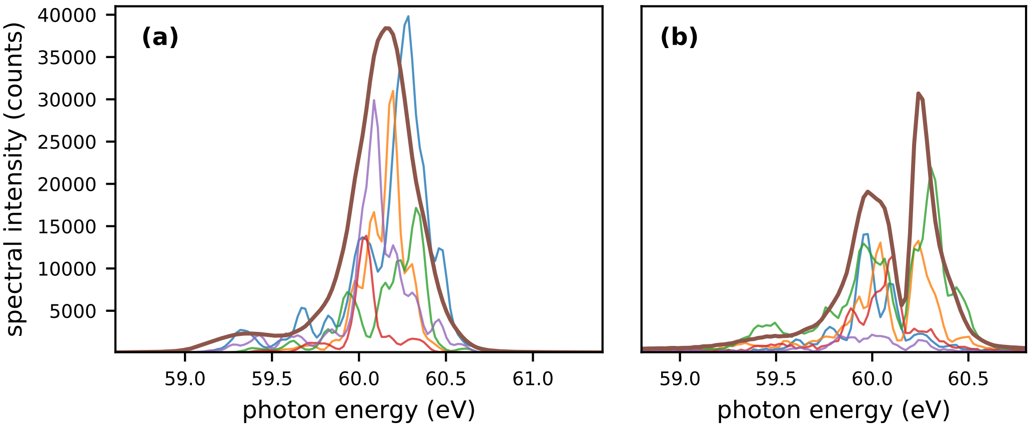

Figure 3.7.: Experimentally measured spectra recorded by the BL spectrometer. Depicted are ten consecutive pulses (color) and an average over 200 pulses (brown) scaled by a factor of 3 to be qualitatively comparable to the single-shot spectral peak intensities. **(a)** Without a target gas in the cell. **(b)** With helium at a backing pressure of about 100 mbar. Note that the spectral position of FLASH shifted between the times of the measurements with and without the gas target. Furthermore, the absolute values of the spectral intensity in (a) and (b) are not comparable due to different filter attenuations in the spectrometer chamber.

One can observe the intensely spiky spectral structure and the massive shot-to-shot fluctuation. With an average over at least 100 individual pulses the spectrum becomes sufficiently smooth for analysis of the OD.

The Measurement

This chapter showed that the BL in combination with FLASH presents an ideal basis for strong field experiments in the XUV. Thus, all experiments discussed in this thesis are conducted using this facility-based TAS approach. For the goal of this thesis, the investigation of helium in highly intense fields, the XUV pulse energy is scanned. In both experiments multiple 10 k single pulses are recorded at 10 Hz. During that time, the gas attenuator is ramped up and down manually to increase the statistic in all pulse energy bins (fig. 3.3). An additional measurement is performed for about 10,000 pulses with no helium in the target cell. These measurements serve as respective *no target measurements* for the mapping of the spectrometers in chapter 4.2.
The XUV camera is activated by the BL's data acquisition system (DAQ) and triggered by FLASH. Upon successful acquisition, the system receives a signal from the camera and queries the numeric pulse identifier from FLASH (see ch. 4.1). Once the data are downloaded form the camera, and the DAQ system activates it again. Ideally the regions of interest are chosen such that this process fits within the 100 ms cycle to

benefit from the 10 Hz rate of FLASH. Every ten pulses, the recorded spectra are stored in combination with the monitored values of the stage potions and the gas pressures into one file. All facility-based devices record their data in binary from to on-side servers. Though it is possible to access the real-time data for live-analysis programs, e.g. monitoring the pulse energy statistic or the appearance of an interesting effect, the full database in hdf5 format file form is provided after the campaign. These databases in combination with the files recorded in the BL DAQ are the starting point for the data evaluation in the next chapter.

4. Data Evaluation

So far the experiment is conducted and the measured data acquired. The next step is the preparation of this raw material to allow for the observation and analysis of physical effects. This proceeding is split in several tasks, starting from the correct pulse assignment between the different databases (end of ch. 3.3), continuing via the calibrations of the spectrometers and finally the sorting of the individual pulses into bins to retrieve the pulse-energy dependent OD.

4.1. Pulse Assignment

The data recorded during the experiments are stored by the individual devices (e.g. GMD, spectrometer, reference spectrometer) on different server machines as discussed at the end of the previous chapter. Since the data analysis in this thesis is based on a single-shot evaluation, an assignment of the individual pulses between the datasets has to be conducted. While the temporal synchronization between FLASH and the BL is created via a basic trigger signal, the overall pulse assignment is based on a facility-wide identifier. This numeric ID is generated for every individual pulse of FLASH, the so-called *bunch ID*. The BL's DAQ queries that number for every trigger signal while the XUV camera is active. Systematic shifts between the IDs recorded in the measurement devises make a pulse-assignment test for every evaluated dataset necessary. For that purpose, the stochastic feature of the SASE pulses are utilized. The integrated recorded spectra of the BL and the reference spectrometer as well as the measured pulse energies are compared with one another in statistical correlation plots. Such a correlation is presented in figure 4.1 for a correct (blue) and incorrect (grey) pulse assignment.

With this method a bunch ID shift of $\Delta = 1$ one is determined between the reference spectrometer and the BL data acquisition. On the other hand, the remaining devices recorded the data in correct pulse assignment to one another for the here considered experiments. Elegantly, this technique works with as well as *without* a target in

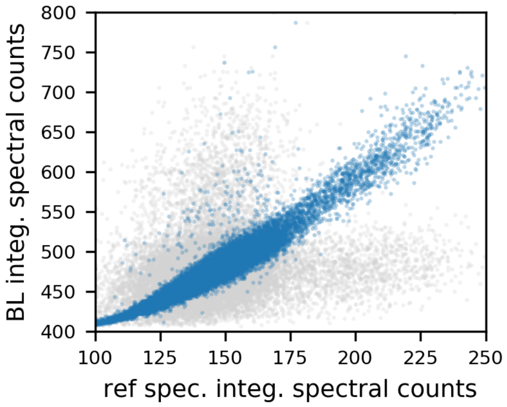

Figure 4.1.: Measured integrated spectra of the BL and reference spectrometer correlated for a bunch-ID shift of zero (gray) and one (blue). It can be easily identified that a shifted pulse assignment between those devices exists. For illustration purposes the spectra are averaged instead of integrated here.

the focus, as the absorption acts globally on the correlation and does not result in a scattered pattern of an uncorrelated cloud. The deviation from a perfect line in the correlated case (fig. 4.1) arises from non-linearities in the CCD chip of the spectrometers and measurement uncertainties of the facility devices.

4.2. Spectrometer Mapping and Calibration

As a first step for all further processes, the background signal of each spectrum is subtracted. For that purpose the background is determined via a linear fit in regions not illuminated on the CCD chip on both sides of the spectral intensity peak and subsequently subtracted from the spectrum. This step is performed for all spectra individually.

For the calculation of the OD (eq. 2.38), the spectral axis of the two spectrometers, the reference spectrometer in the BDA and the spectrometer in the BL, have to be mapped onto each other. Both of them contain non-stationary optics, namely the VLS gratings (3.3) and thus do not possess a permanently calibrated spectrometer axis. Therefore, the mapping cannot be conducted via the calibrated photon axes and a different approach is required. In principle, the spiky spectral structure of the SASE single pulses would present an ideal pattern to link both photon energy axes. However, the spectral intensities seen by both devices are not identical due to clipping in the beam path in the BDA and spatial incoherence of the SASE beam, which makes this method insufficient. Instead, a solution needs to include the averaging of multiple pulses to eliminate this effect. Two options are considered: First, the covariance analysis (cov), where the outer product of the measured spectra of the BL spectrometer S and the reference spectrometer S_{ref} is evaluated, averaged and normalized [76]. A more advanced version, the partial covariance analysis (pcov), eliminates intensity fluctuations of the pulse energy (I) from the result:

$$\begin{aligned} cov(S, S_{ref}) &= \langle S \times S_{ref} \rangle - \langle S \rangle \cdot \langle S_{ref} \rangle \\ pcov(S, S_{ref}, I) &= cov(S_{ref}, S) - \frac{cov(S, I) \cdot cov(I, S)}{cov(I, I)} \end{aligned} \tag{4.1}$$

The result is a matrix with the dimensions of both spectrometer axes (fig. 4.2(a)). It shows a dominant correlation ridge, which maps the two spectral axes to each other. The ridge is interpolated and sliced orthogonally to its long axis to apply a peak-finder algorithm. In principle, also the maximum value per line can be evaluated, which leads to a more crude result, though. The computed points then present the mapping curve of both spectrometers.

The second approach maps the reference spectrometer onto the BL spectrometer

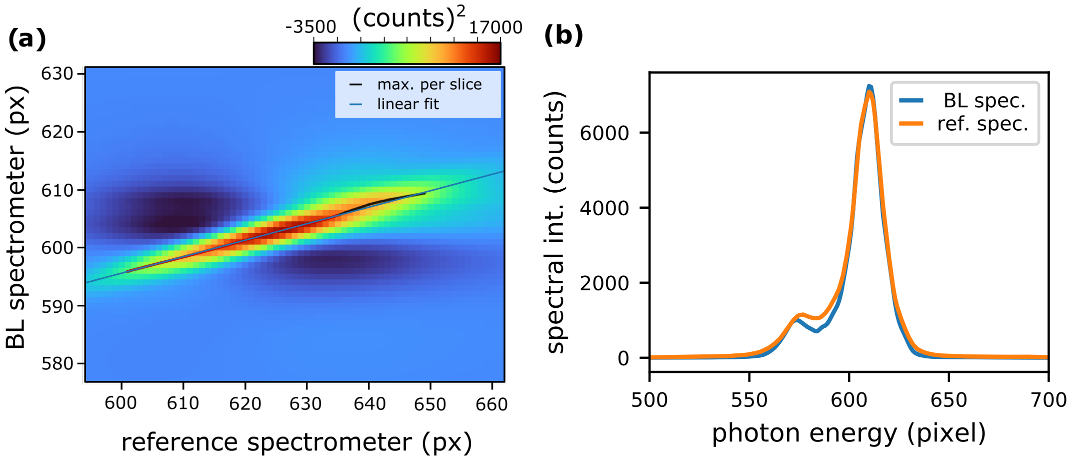

Figure 4.2.: Mapping of the BL and reference spectrometer via **(a)** the partial covariance analysis depicted here with the fitted maxima of the ridge (black) and their linear fit (blue), **(b)** the polynomial axis scaling of the reference spectrometer determined by minimizing the integrated difference.

by a polynomial scaling and interpolation of its spectral and amplitude axis. For that purpose, a measurement without target gas in the focus is conducted and the spectra of each device averaged for several pulses. The fit algorithm optimizes for the integrated difference of both spectra (figure 4.2(b)). Since the illuminated region on the photon energy axis is limited to sub 100 pixels and the resonance to a few ten pixels on the CCD chips, polynomial orders higher than the third order are without

significant contribution ($< 10^{-6}$). The scaling of the signal amplitude axis is chosen to be linear.
Comparing both methods, the second approach is chosen for the presented datasets, since it closely recreates the literature Fano line-shape asymmetry (q parameter) of the considered resonance in the weak field limit (see ch. 6). Shortly summarized, the covariance method exhibits difficulties in the mapping of the wings of the FEL spectrum (see fig. 4.2(a)), where the narrow resonance is spectrally located due to a red-detuned central photon energy.

After the mapping of both spectrometers is established, the **calibration of the photon-energy axis** remains. The reasons for a lack of a calibration in both spectrometers has been elaborated in the previous section. A spectral calibration is usually conducted via the identification of known resonances, where their energy positions serve as reference points. An ordinary approach with several resonances in the absorption spectrum is not practical during the measurement campaign. One of the reasons it the narrow FEL spectrum of roughly 0.4 eV at 60 eV. On the other hand, within this bandwidth only one narrow, isolated resonance is investigated. Therefore, calibration of the full range of the spectrometer is not require and a precise calibration in the vicinity of the resonance is sufficient. Elegantly, this resonance is well characterized by synchrotron measurements [40]. Hence, its literature values recorded with synchrotron radiation can be utilized for the calibration. For that, the spectra of pulses with pulse energies below 5 µJ are averaged and the OD (eq. 4.2) calculated. The resulting OD is fitted by the Fano formula (eq. 2.43). The resulting line-width and resonance-position parameters are matched with the literature value of the resonance (width $\Gamma = 37\,\text{meV}$, position $E_r = 60.15\,\text{eV}$). This provides a full and sufficient energy calibration for the spectral region of interest.
For a proper quantification of experimentally measured absorption lines the resolution of the experimental apparatus has to be taken into account. Therefore, the fit process of the Fano formula includes the convolution of the theoretical Fano formula with a Gaussian function. The width of this Gaussian envelope represents the spectrometer resolution. It is once determined for low pulse energies and then set as a constant for all further experimental fit processes within each measurement shift during a measurement campaign. The spectrometer setup received minor changes between the measurement campaigns (see 3.3). Hence, the spectrometer resolution differs slightly and is determined to 75 meV FWHM in the first and 59 meV FWHM in the second measurement campaign (ch. 3.3).

The reference spectrometer in the BDA inherently sees no spectrum transmitted through the target gas. Furthermore, its recorded spectra are only evaluated averaged over several pulses. The thus smooth spectral envelopes have been mapped to the BL spectrometer and consequently a separate energy calibration and determination of the resolution is not needed.

4.3. Absorbance Evaluation

When the preparation in form of pulse assignment, spectrometer mapping and calibration is successfully achieved, the individual measurements can be analyzed. The experimental datasets in this work are based on pulse energy measurements. In addition to the fluctuation of the pulse energy due to the stochastic nature of the SASE-based FLASH, the average pulse energy is further tuned with the gas attenuator, discussed in chapter 3. This leads to an equal distribution of pulses in all regimes of the available pulse energy.

Algorithmic filters are applied to the dataset in order to increase data quality. The most basic one eliminates all shot events where one or more devices have not recorded adequate data, e.g. empty spectra. To exclude any effects on the measurement which originate from factors correlated with the pulse energy measured after the undulator, e.g. shift in the central photon energy, further algorithmic filters can be added. The top 30% of the pulse-energy SASE statistic before the gas attenuator is selected. Therefore, all pulses in each energy interval after the gas attenuator originate from the same window of pulse energies before the gas attenuator.

The OD of the measured pulses is obtained with equation 2.38. Due to the stochastic nature of the SASE spectra and the non-identical spectra measured in both spectrometers, a single-pulse calculation of the optical density is not feasible. Instead, the spectra are sorted first into bins subdividing the full pulse energy range. They are then averaged $\langle \ldots \rangle$ within each bin j for both spectrometers individually. With these averaged spectra the OD is determined by

$$OD_j(\omega) = -\log_{10}\left(\frac{\langle S(\omega)\rangle_j}{\langle S_{ref}(\omega)\rangle_j}\right) \tag{4.2}$$

with the spectral intensities $S(\omega)$ of the BL spectrometer and $S_{ref}(\omega)$ of the reference spectrometer, respectively. Note that the bin size is adjusted such that at least a hundred pulses are averaged to ensure a sufficiently high signal-to-noise ratio. Once the OD is calculated for all bins of the pulse energy range, the same procedure is performed for the subsequent reference, the measurement without target, if available. This no-target OD can serve as a quasi background containing small systematic errors which cannot be eliminated otherwise. It is thus subtracted from the main measurement. In particular, at the second campagne this has resulted in an improved signal.

The quantification of the helium 2s2p absorption line is conducted with the Fano formula (eq. 2.43). In the experimental case, the spectrometer resolution acts on the observed absorption line shape. In order to achieve correct fit results, the Fano formula is convoluted with a Gaussian function of width equal to the spectrometer resolution. The spectrometer resolution, however, is on the same order as the pixel width of the spectrometer camera. Therefore, the grid resolution of the spectrometer axis is increased for the process of the convolution by interpolation. The resulting convoluted spectrum on the high-resolution grid is evaluated on the original, non-interpolated grid positions. This proceeding is performed in every step of the optimizing algorithm. In this chosen approach the presented OD contains the spectrometer resolution. This follows the principal to look at the measured data as unaltered as possible in presence of many systematic and statistic influences at an FEL. At the same time, the line-shape parameters resulting from the fit algorithm are independent of the spectrometer resolution and can be compared to literature values and numeric simulations.

5. Simulation Framework

To draw conclusions from observations in the experiments, a basic numeric model simulation is set up. First, the quantum-mechanical treatment of the light-matter interaction (ch. 2.1.1) is transferred into a numeric procedure of a few-level model simulation. It is then adapted to the helium 2s2p resonance, the transition at the center of this work. Finally, it is followed by an introduction of the partial-coherence pulse model, a numeric method to generate SASE-like stochastic pulses.

5.1. Few-Level Model Simulation

In the experiment the considered resonance is dressed with intense XUV pulses. Hereby, the photon energy of the radiation is close to the energy of the transition. As discussed in chapter 2.1, this leads to a significant population transfer and makes a full quantum-mechanical treatment beyond the limit of perturbation theory necessary. Chapter 2.1 described the quantum mechanical treatment of the interaction between electric fields and quantum states of atomic systems. This is extended here, since the analytic treatments of the light-matter interaction are solved for monochromatic electric fields. For the ultrashort and even stochastic pulses utilized in the analysis of the experiments the numerical approach is thus desirable. In a numerical few-level model, which is the basis for this simulation, the aim is to consider as few states as possible and, at the same time, as many states as necessary to correctly describe the experimental observations. For the resonance considered in this work, namely the 2s2p state in helium, this approach is a perfect match. The resonance is spectrally isolated and the bandwidth and spectral position of the XUV pulses thus limit the quantum mechanical states to consider to the ground state, the 2s2p state and the energetically degenerate continuum. The goal is to access the parameters of the quantum mechanical states, e.g. their energy and population, to allow for the exploration of the time-dependent coupling effects. Note, for convenience the treatment and numerical calculations are given in atomic units (a.u.) with $\hbar = e = m_e = 1$ (unless noted otherwise).

As explained in chapter 2.1.1, the equation of motion for an non-relativistic quantum system is the Schrödinger equation (SE)

$$i\frac{\partial}{\partial t}\left|\boldsymbol{\Psi}(t)\right\rangle = \hat{H}(t)\left|\boldsymbol{\Psi}(t)\right\rangle \tag{5.1}$$

with the Hamiltonian operator $\hat{H}(t)$ describing the quantum system. The time-dependent wave function $|\boldsymbol{\Psi}(t)\rangle$ can be represented as the superposition of the n orthogonal states of the unperturbed and uncoupled system

$$\left|\boldsymbol{\Psi}(t)\right\rangle = \sum_{k=0}^{n} c_k(t)\left|\Phi_k\right\rangle \tag{5.2}$$

with the time-dependent state coefficients $c_k(t)$. Expanding the SE in the matrix representation with $k \in n$

$$i\frac{\partial}{\partial t}\begin{pmatrix} \vdots \\ c_k(t) \\ \vdots \end{pmatrix} = \begin{pmatrix} \langle 0|\hat{H}(t)|0\rangle & \langle 0|\hat{H}(t)|1\rangle & \cdots & \langle 0|\hat{H}(t)|n\rangle \\ \langle 1|\hat{H}(t)|0\rangle & \ddots & & \vdots \\ \vdots & & \ddots & \\ \langle n|\hat{H}(t)|0\rangle & \cdots & & \langle n|\hat{H}(t)|n\rangle \end{pmatrix}\begin{pmatrix} \vdots \\ c_k(t) \\ \vdots \end{pmatrix}, \tag{5.3}$$

the energy of the n states is found on the diagonal of the Hamiltonian matrix, while the coupling between the states is described by the off-diagonal elements. A solution to equation 5.3 is given by the temporal evolution of the state vector $\mathbf{c}(t) = [c_0(t), \ldots, c_n(t)]^T$:

$$\begin{pmatrix} \vdots \\ c_k(t) \\ \vdots \end{pmatrix} = e^{-i\,H(t)\cdot t}\begin{pmatrix} \vdots \\ c_k(t_0) \\ \vdots \end{pmatrix}. \tag{5.4}$$

The Hamiltonian matrix $H(t)$ is diagonalized, as it in general contains off-diagonal elements. In order to be diagonalizable, it can only contain numeric values and all variables are evaluated beforehand. The resulting eigenvectors of the diagonalization procedure build the columns of the matrix T presenting a unitary transformation $\hat{T}$ with $T^{-1}\cdot T = \mathbb{1}$. These matrices transform the state vector between the uncoupled basis and the eigenbasis of the diagonalized Hamiltonian. Hence, the solution to equation 5.4 for a discrete time step Δt can be written as

$$\begin{aligned}\mathbf{c}(t+\Delta t) &= e^{-iH\Delta t}\ \mathbf{c}(t) \\ &= T^{-1}\, T\ e^{-iH\Delta t}\ T^{-1}\, T\ \ \mathbf{c}(t).\end{aligned} \tag{5.5}$$

The diagonalized Hamiltonian

$$H_{diag}\ =\ T\ H\ T^{-1}\ =\ \begin{pmatrix} \lambda_0 & & \\ & \ddots & \\ & & \lambda n \end{pmatrix} \tag{5.6}$$

hereby contains only the eigenvalues λ_k determined in the diagonalization. Equation 5.5 thus computes to

$$\mathbf{c}(t+\Delta t) = T^{-1}\ e^{-iH_{diag}\cdot\Delta t}\ T\ \mathbf{c}(t). \tag{5.7}$$

Effectively, the state vector is rotated in the complex-valued Hilbert space $T\,\mathbf{c}(t)$ where the state is propagated by $e^{-iH_{diag}\cdot\Delta t}$ with the diagonalized Hamiltonian H_{diag}, before it is rotated back into the initial basis by the inverse transformation matrix T^{-1} and finally evaluated. The rotation and propagation are repeated for every step on the temporal grid. In addition, the diagonalization of the Hamiltonian has to be computed for every step as well, if time-dependent components are contained within the off-diagonal of the Hamiltonian, e.g. a coupling by an external electric field $\tilde{F}(t)$. Finally, a time-dependent observable can be evaluated by

$$X(t) =\ \langle\mathbf{\Psi}(t)|\hat{X}|\mathbf{\Psi}(t)\rangle = \sum_{k=1}^{n}\sum_{m=1}^{n} c_m^*(t)\cdot\ \langle m|\hat{X}(t)|k\rangle\cdot c_k(t). \tag{5.8}$$

5.1.1. Split-Step Approximation

Taking a deeper look at the technical realization details of the simulation, some further aspects are notable: When the Hamiltonian matrix becomes time dependent by the electric field $\tilde{F}(t)$, it can be split into a field-free and field-dependent part:

$$H(t) = H_0 + H'(t) = H_0 + \tilde{F}(t)\cdot H''. \tag{5.9}$$

This allows for a reduced numerical effort as the diagonalization of $\hat{H}_0$ and $\hat{H}''$ has to be performed only once. The propagation is then conducted utilizing the split-step algorithm [77, 78]: First, the time-independent part is propagated by $1/2\,\Delta t$, followed by the time-dependent part with Δt and finalized by $1/2\,\Delta t$ of the time-independent part:

$$\mathbf{c}(t+\Delta t) = T_0^{-1}\, e^{-i\,H_{0,diag}\cdot\Delta t/2}\; T_0 \cdot T''^{-1}\, e^{-i\,\tilde{F}(t)\cdot H''_{diag}\cdot\Delta t}\; T'' \cdot T_0^{-1}\, e^{-i\,H_{0,diag}\cdot\Delta t/2}\; T_0 \;\cdot \mathbf{c}(t). \tag{5.10}$$

In this implementation the algorithms provides second order accuracy in the time step Δt [79].

Note, that for a correct result of an observable with relation to the external field, e.g. the dipole response for the OD, the point-in-time for the evaluation and storing of the field and the state vector have to be synchronized. In the realization of this work the state coefficients have been stored after each full propagation of both Hamiltonian parts H_0 and H'. Meanwhile, the electric field is evaluated in the middle of each propagation cycle. To correct this temporal difference of evaluation, the state coefficients are shifted by $1/2\,\Delta t$. This is realized by the interpolation of the state coefficient array.

A non-shifted state vector would lead to a phase-shifted dipole response of the system in reference to the phase of the electric field. This would cause a non-physical modification of the line-shape symmetry (eq. 2.42), which in its degree is then dependent on the grid resolution.

5.1.2. Helium 2s2p Resonance

The general concept of the few-level model simulation is now applied to the atomic target system investigated in this work: Helium. When driving the ground state to the 2s2p transition resonantly with XUV pulses of 0.4 eV FWHM bandwidth, only three states have to be considered in the Hamilton matrix: The ground state $(|\Phi_g\rangle)$, the doubly excited state $(|\Phi_e\rangle)$ and the pseudo continuum state $(|\Phi_c\rangle)$:

$$H(t) = \begin{pmatrix} E_g & d_{ge}^{*}\cdot\tilde{F}(t) & d_{gc}^{*}\cdot\tilde{F}(t) \\ d_{ge}\cdot\tilde{F}(t) & E_e & V_{CI}^{*} \\ d_{gc}\cdot\tilde{F}(t) & V_{CI} & E_c - i\,\Gamma/2 \end{pmatrix}. \tag{5.11}$$

Besides the energies to the unperturbed atom, the Hamilton contains coupling elements on the off-diagonal, in particular the coupling of the states by the dipole matrix elements d_{mk} and the real-valued electric field $\tilde{F}(t)$. The ground state is set to $E_g = 0\,\mathrm{eV}$. Normally, as described in Fano's theory (ch. 2.2) the continuum above the ionization threshold is represented by an infinite sum of single-electron-ionization-continuum states. Instead, a very broad state is numerically realized here. This has the advantage

of limiting the calculation cost compared to the large number of overlapping, narrow states representing the continuum. The width of this pseudo continuum describes the loss rate of its population. It is defined by the imaginary part of the eigenenergy of the continuum state with $\Gamma = 39.73\,\text{eV}$. Its energetic position $E_c = 32.65\,\text{eV}$ and dipole-matrix element coupling it to the ground state $d_{gc} = 0.6753\,\text{a.u.}$ are calibrated to the off-resonant absorption cross section in helium [80, 81].
Meanwhile, the excited state is set to $E_e = 60.115\,\text{eV}$. This value is calibrated such, that the resulting absorption line is located on the literature value of of 60.15 eV [40]. Furthermore, the values of the dipole matrix elements $d_{ge} = -0.04932\,\text{a.u.}$ and the configuration interaction $V_{CI} = 0.0373\,\text{a.u.}$ are taken from literature [82] with minor adjustments to meet the line shape parameters measured at synchrotron experiments [40]. At the beginning of the simulation the state vector $\mathbf{c}(t) = [c_g(t),\, c_e(t),\, c_c(t)]^T$ is fully in the ground state $\mathbf{c}(t = 0) = [1,\, 0,\, 0]^T$. It is propagated with equation 5.10 on the temporal grid, which has a resolution of $\Delta t = 0.1\,\text{a.u.}$ and a length ($\approx 50000\,\text{a.u.}$) sufficient to fully comprise both, the XUV pulse and the dipole response. Finally, the temporal dipole is calculated following equation 5.8:

$$d(t) = \left(c_g^*(t) \cdot d_{ge} \cdot c_e(t) + c_g^*(t) \cdot d_{gc} \cdot c_c(t)\right). \tag{5.12}$$

The spectrum of the dipole response $d(\omega)$ is evaluated via Fourier transformation (eq. 2.34). With that, the OD can be determined (eq. 2.38 and 2.39).

5.2. Partial-Coherence Pulse Model

The numeric investigation of the 2s2p doubly excited state in helium in the presence of intense stochastic fields requires simulated SASE-like fields as input. To realistically model such pulses, the partial-coherence pulse model (PCPM) [83] is utilized:
The general concept starts in the spectral domain on a discretized grid. A spectral intensity envelope $S_0(\omega_j)$, in this case a Gaussian function of chosen bandwidth, represents the input parameter of the first model. For every point j on the spectral grid a random phase value $\varphi(\omega_j) \in [-\pi, \pi)$ is generated (first panel in fig. 5.1). Combined with the real-valued spectral amplitude $\tilde{F}_0(\omega_j) \propto \sqrt{S_0(\omega_j)}$, it provides the complex valued electric field $F(\omega_j) = \tilde{F}_0(\omega_j) \cdot e^{i\,\varphi(\omega_j)}$. This is Fourier transformed (eq. 2.34) into the temporal domain $F(t_l) = \mathfrak{F}\left\{F(\omega_j)\right\}$. Note, that the spectral grid requires a resolution of $\Delta\omega \ll 2\pi \cdot \tau^{-1}$ with τ the typical time scale of the desired

pulse envelope.

The electric field $F(t_l)$ exhibits a temporal structure of spiky features (second panel fig. 5.1). Its amplitude is equally distributed over the entire grid, due to the initial random phase. Here, the second input parameter comes into play: The temporal duration of the generated pulse is introduced by the multiplication of the stochastic field with a temporal window envelope $F_{\mathrm{w}}(t)$, in this case a Gaussian function: $F_{\mathrm{pulse}} = F_{\mathrm{w}}(t) \cdot F(t)$. The overall pulse duration is then determined by the width of $|F_{\mathrm{w}}(t)|^2$. The result is a SASE pulse suitable for the few-level model simulation. To account for the statistical nature of SASE FEL experiments, a manifold of different SASE pulses has to be computed with individual sets of initial phases. It results in a library of stochastic pulses with individual temporal stochastic fields. Note, that for different pulse durations it is sufficient to repeat the last step in the process following the choice of the temporal window envelope.

The spectrum of these new pulses $S_{\mathrm{pulse}}(\omega) \propto \left|F_{\mathrm{pulse}}(\omega)\right|^2$ is evaluated by the inverse Fourier transformation $F_{\mathrm{pulse}}(\omega) = \mathfrak{F}^{-1}\left\{F_{\mathrm{pulse}}(t)\right\}$, see third panel figure 5.1. Here, the observation can be made, that the spiky spectral structure of the individual pulses is in qualitative agreement with the experimentally measured single shot spectra (compare fig. 3.7). The good approximation of the PCPM has recently been shown in comparison with experimental results and complex numerical bottom-up FEL calculations [84].

One advantage of the model is the direct access to the spectral phase (fig. 3.7 right panel). Compared to the initial random values, the phase obtained structure and contains smooth segments with steep, random jumps between them. The order has been induced by the limitation of the Gaussian envelope in the temporal domain. In short, the pulse gained partial coherence, giving the name to the method in the first place.

Finally, the average of the spectra from several stochastic pulses, each of individual spiky nature, reproduces the initial spectral envelope $S_0(\omega_j)$ of the first step. From that, one can deduce that the average temporal width τ^* of the intra-pulse intensity spikes corresponds to the width $\Gamma^* = 1/\tau^*$ of the initial spectral envelope. Even though this relation is only valid for a flat spectral phase, it serves as a good estimate, since the phases are comparably flat within a single spectral spike. The knowledge of the duration from intensity spikes becomes relevant when the durations reaches the same order of magnitude as the lifetime of the investigated state.

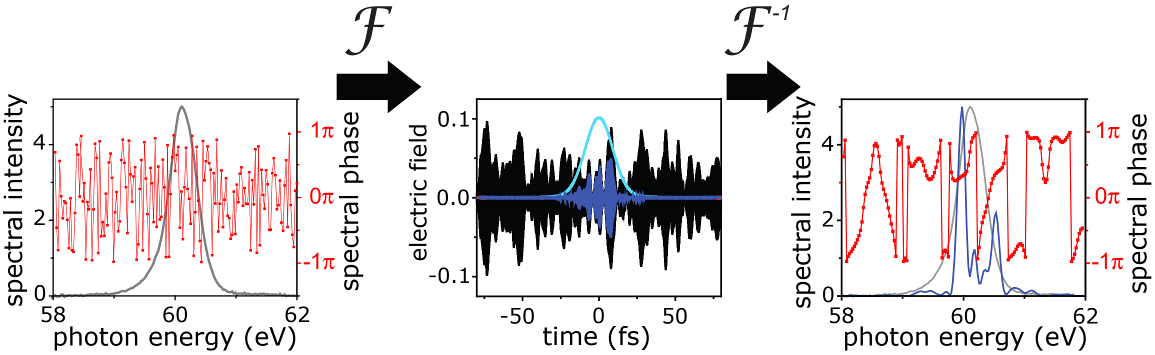

Figure 5.1.: Illustration of the partial-coherence pulse model [83] utilized for the numerical SASE-like electric-field generation process. **First panel**: The initial spectral envelope (grey) with a randomly generated spectral phase (red) for every point on the grid. Combined as a complex-valued electric field it is Fourier transformed. **Second panel**: The result is a stochastic electric field (black). A window function (cyan) defines the duration of the resulting stochastic pulse (blue). **Third panel**: Fourier transformed back into the spectral regime, the spectral intensity (blue) exhibits a spiky structure while the spectral phase (red) gained partial coherence compared to the initial case (first panel). The average of multiple spectral intensities results in a smooth curve (grey) recreating the initial spectrum. Figure adapted from [85].

The OD from a simulation utilization such stochastic pulses as input electric fields is evaluated with equation 2.41. In most cases, unless noted otherwise, a count of 300 pulses has been sufficient for a smooth OD result. The quantity η represents the pulse length density and other fundamental constants (ch. 2.3). In this realization its value $\eta = 10^{-4}$ arises from the calibration of the OD to the same order of magnitude as the experimentally measured OD.

6. Experimental and Numerical Results

The goal of this work is the exploration of the autoionizing 2s2p state in helium and its two-electron transition from the ground state in presence of resonant, highly intense XUV fields.

For this purpose, measurements scanning the XUV pulse energy have been conducted at FLASH with the presented setup (ch. 3). In this chapter the results of the recorded data are presented and discussed, which have been evaluated as layed out in chapter 4. In the first section the shape of the photon absorption line and its asymmetry stands in the focus. Particularly the changes to the symmetry by intense XUV pulses are investigated. A numeric model simulation introduced in chapter 5 is conducted in order to discover the physical origin of the observed effects. The second section concentrates on the controlled manipulation of the absorption line shape. As the experimentally measured data originate from two measurement campaigns with different SASE-pulse parameters, the impact of the pulse duration on the symmetry distortion is examined. Here, the numeric model is extended from Gaussian-shaped dressing field to stochastic pulses, taking into account the SASE nature of the XUV pulses utilized in the experiment. In the third and final section, the absorption line width is studied, providing insight into the coupling dynamics of the autoionizing state.

6.1. Line-Shape Symmetry Distortion

The 2s2p state in helium has been well characterized with low-intensity XUV radiation generated by synchrotrons [40]. Reproducing the observed spectral line shape is part of the first measurement. To gain a deeper understanding the question is raised how the observed transition is altered when it is resonantly driven with strong XUV fields. Thus, the helium 2s2p is dressed resonantly with XUV laser pulses from FLASH in

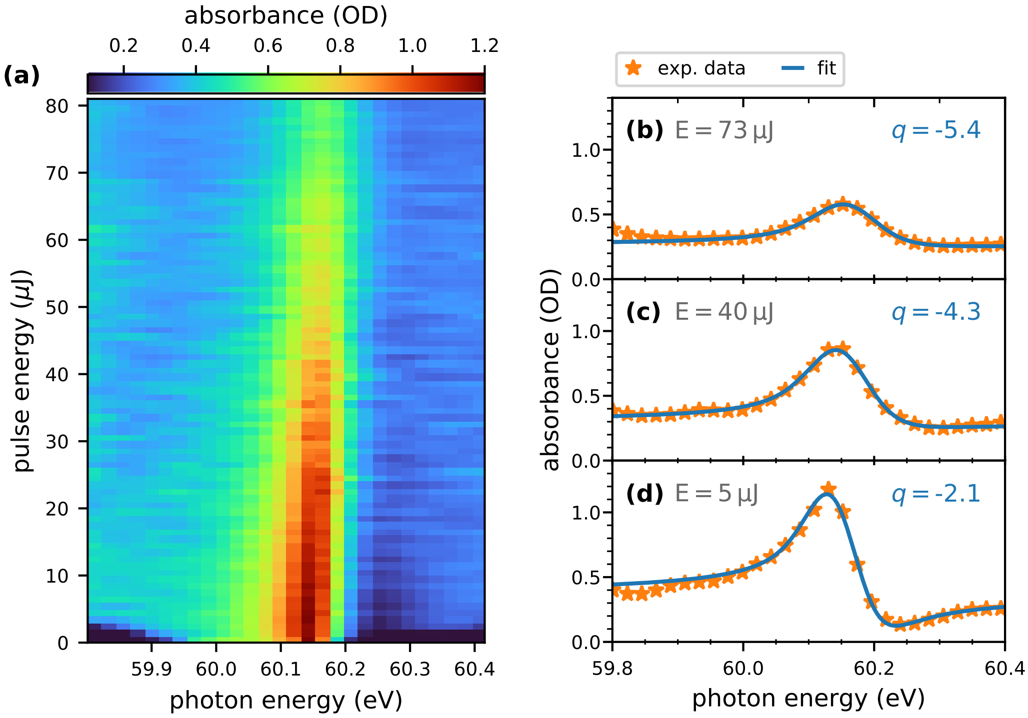

Figure 6.1.: Experimental pulse-energy scan of the He 2s2p resonance using 75 fs FWHM overall duration XUV SASE pulses. **(a)** two-dimensional map of the OD for a pulse-energy range between 0 µJ and 80 µJ. **(b)-(d)** OD lineouts as orange stars for selected pulse energies E noted in the panels. The Fano fits are depicted as blue lines in combination with the respective resulting q parameter.

an experimental investigation. Hereby, the FEL is set to 10 Hz single bunch mode at a photon energy of 60 eV with a spectral bandwidth of 0.4 eV FWHM and an overall pulse duration of approximately 75 fs. An intensity scan is performed, in which the average pulse energy is tuned with the gas attenuator (ch. 3.2) between the weak-field limit of a few µJ up to the strong-field regime of about 60 µJ, with peak pulse energies reaching beyond 80 µJ. Note, as discussed in chapter 3.3, the pulse energy on target is estimated to 50% of the value recorded by the GMD (ch. 3.2). This is due to losses in the beamline transmission. Thus the maximum pulse energy on target amounts to 40 µJ. However, since the GMD measured pulse energy is the directly recorded quantity in the experiment, it will be used as pulse energy representative in the following. The single pulses are varied in pulse energy by the attenuator as well as the SASE fluctuation. They are sorted into 1 µJ wide bins, similar to a multi-dimensional histogram. For each bin the measured quantities are averaged and evaluated in accordance to chapter 4.3. The resulting OD (ch. 4.2) is depicted in from of a 2D-color plot (fig. 6.1 (a)), showing the pulse energy dependence of the absorption signal. While a peak at 60.15 eV and a dip at 60.25 eV can be

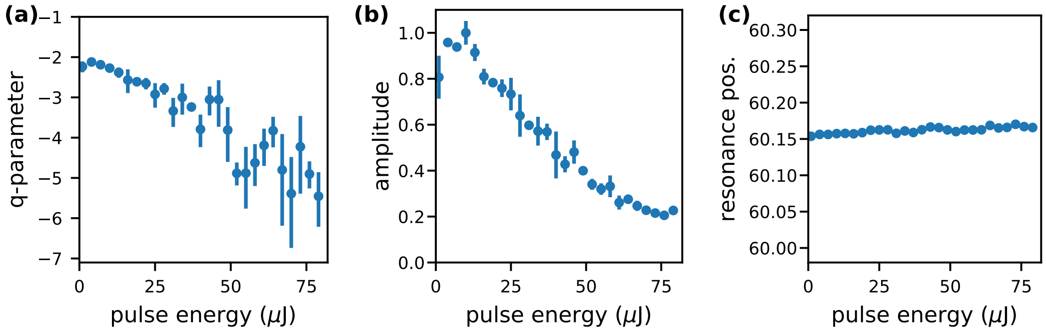

Figure 6.2.: Absorption line parameters extracted from the Fano fit of the experimental data in figure 6.1. The results for the **(a)** q parameter, **(b)** line amplitude and **(c)** resonance position are depicted over pulse energy. Hereby, the amplitude is normalized to its highest values in the weak-field limit.

identified for small values of pulse energy, both extremes decrease and the dip vanishes with rising pulse energy. This becomes more evident in the single lineouts presented in figure 6.1 (b)-(d)). At low pulse energies the absorbance is described by the typical asymmetric Fano-like absorption line shape (fig. 2.5(a) and [40]). For rising pulse energy two observations can be made: First and predominantly, the amplitude of the absorption line decreases. Secondly, the asymmetry of the resonance qualitatively evolves towards a more symmetric line shape.

To quantify these observations, the theoretical Fano formula (eq. 2.43) convoluted with the spectrometer resolution (ch. 4.2) is fitted to the measured absorption lines. Three examples of that are depicted in figure 6.1 (b)-(d). The results of the Fano fit parameters are shown in figure 6.2. For the statistical uncertainty, the fit parameters for respectively three consecutive pulse-energy bins (fig. 6.1(a)) are combined. The mean and the standard deviation in these combined bins represent the value and uncertainty displayed in the respective panel (fig. 6.2). This procedure is chosen for technical reasons in this case. As the bins are sorted by pulse energy, the given uncertainties present the upper limit for the statistical uncertainties.

Concentrating on the two qualitative observations above, the parameters for the amplitude a and the asymmetry q are analyzed (fig. 6.2). The amplitude (6.2(b)), normalized to its peak value, exhibits a reduction of 80% in respect to its initial value. This is explained by the depletion of the ground state: Over the duration of the XUV pulse the density of unperturbed target atoms in the ground state decreases due to the interaction with the pulse. With a consequently smaller ratio of the ensemble dipole response and the external field this leads to a smaller amplitude of the OD (eq. 2.41). An outlier in the amplitude for the smallest pulse energy can be recognized.

This is attributed to the small signal-to-noise ratio in measured spectra at that low pulse energy.

Also, the fit result of the symmetry parameter q (6.2(a)) shows a significant change within the statistical uncertainty for rising pulse energy. Starting from $q = -2.2$ at low pulse energies it decreases to about $q = -5$ at 80 µJ pulse energy. As a consequence of equation 2.27 and figure 2.4(b) the calculated trend towards lower values corresponds to a more symmetric line shape. This confirms the observation made above of a symmetry change towards a symmetric line shape induced by high pulse energies. At the upper end of the measured range the q parameter exhibits increasing fluctuations along with a larger statistical uncertainty. Due to the reduced resonance amplitude the signal-to-noise ratio decreases and consequently the Fano line-shape fit has a larger statistical uncertainty. It becomes increasingly challenging to determine the precise symmetry of an almost symmetric absorption line shape when the amplitude decreases (fig. 6.1(b)). One can further identity a deviation of the symmetry parameter ($q \approx -2.2$) from the literature value $q_{lit} = -2.75$ recorded at synchrotron measurements [40] in the low pulse-energy regime. The small difference is attributed to systematic uncertainties within the measurement. It has no significant influence on the here identified trend.

Additionally, the spectral position of the resonance is evaluated (6.2(c)). No clear trend can be identified within the statistical uncertainty of the parameter.

The observed modifications of the absorption line inspire the application of a numerical simulation to gain a deeper understanding of the mechanisms behind these effects. A few-level model for that purpose has been introduced in chapter 5. In that chapter, the procedure and the values utilized in the Hamiltonian (eq. 5.11) are explained. A Gaussian pulse with a flat phase is selected as the input electric field. This is motivated by the fact that SASE pulses consists of single intensity spikes within their temporal envelope [32, 85, 86]. Here, these intensity spikes are approximated by a Gaussian pulse to investigate the impact of such a single spike. In chapter 5.2 the link between the average duration of intra-pulse intensity spikes and the spectral bandwidth is discussed. With the experimentally measured spectral bandwidth of 0.4 eV FWHM, the temporal duration of the Gaussian envelop is set to 4.66 fs. The central photon energy is also slightly red detuned from resonance to mimic the experiment. It is set to 59.9 eV, which includes a slight adjustment to emphasize the observed effect [7].

An intensity scan is performed utilizing this simulation with peak intensities between

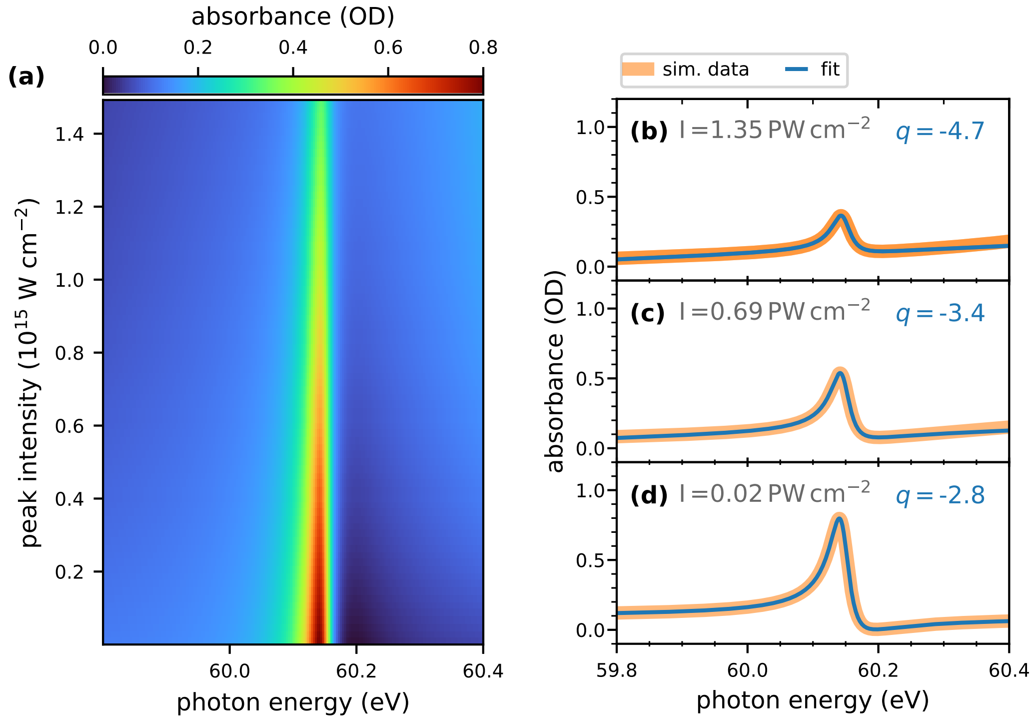

Figure 6.3.: Numeric intensity scan of the He 2s2p resonance conducted with the few-level model simulation using 4.66 fs FWHM long Gaussian XUV pulses. **(a)** two-dimensional map of the OD for a intensity range between 0.0×10^{15} W cm^{-2} and 1.5×10^{15} W cm^{-2}. **(b)-(d)** OD lineouts as orange translucent lines for selected pulse intensities I noted in the panels. The Fano fits are depicted as blue lines in combination with the respective resulting q parameter.

the weak-field limit of 10^6 W cm^{-2} and 1.5×10^{15} W cm^{-2} in steps of 0.02×10^{15} W cm^{-2}. For later reference, this corresponds to fluences between 10^{-9} J cm^{-2} and 7 J cm^{-2} in steps of 0.1 J cm^{-2}. The OD (eq. 2.39) is determined for every step on the grid with the computed dipole moments. Figure 6.3 presents the intensity-dependent OD. The absorption lines qualitatively show the same behavior as the experimental OD (fig. 6.1(a)): The amplitude decreases with an increasing intensity. At the same time, the line-shape symmetry trends towards a more symmetric line shape (fig. 6.1(b)). Here, the ODs are quantified with the Fano formula 2.43 analogue to the experimental results. The calculated fit parameters (fig. 6.4) confirm: The normalized amplitude falls to about 30 % of the initial weak-field value. Here, one can utilize the access to the quantum mechanical quantities provided by the model to analyze the origin of this decrease. The temporal evolution of the population $P_k = |c_k|^2$ with $k \in \{g, e, c\}$ (ch. 2.1.1) is depicted in figure 6.5. Concentrating only the ground-state population for different intensities (fig. 6.5 (b)) the depopulation is spread over the duration of the pulse. Hereby, the final population level decreases significantly for higher

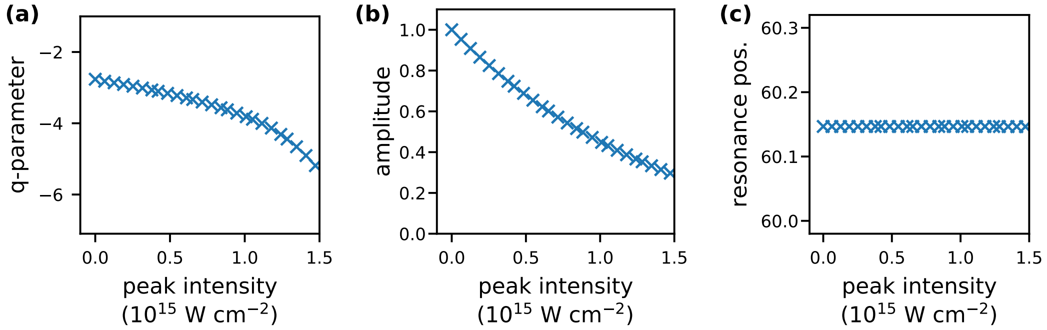

Figure 6.4.: Absorption line parameters extracted from the Fano fit of the simulated data for 4.66 fs FWHM Gaussian pulses in figure 6.3. The results for the **(a)** q parameter, **(b)** line amplitude and **(c)** resonance position are depicted over peak intensity. Hereby, the amplitude is normalized to its highest values in the weak-field limit.

intensities. Consequently, the rising envelope flank of the pulses with high intensity already depopulates a larger portion of the ground state. This leaves the remaining part of the pulse to interact with a smaller density of particles in the ground state, an effect that is known as induced transparency. Hence, the smaller ratio in equation 2.39 leads to a lower amplitude of the OD. This is in line with the explanation provided in the discussion of the experimental observations. While the population is considered here, one can further analyze the temporal evolution of the remaining states in the simulation (fig. 6.5 (a)). Simultaneously to the decline of the ground-state population the excited bound state is populated. After the XUV pulse has passed, the excited state decays accordingly to the literature value of 17 fs lifetime. On the other hand, the population in the pseudo continuum decays so fast that no amount of population is accumulated by the coupling from the other states. This concurs with the purpose of the pseudo continuum state discussed in chapter 5.1.2. Particles which have been ionized no longer contribute to the dipole response and the coupling between the states.

Returning to the results of the Fano fit from the simulation, the symmetry parameter q in figure 6.4 shows a similar trend as in the experiment. Starting from the calibrated value $q = -2.75$ it progresses towards larger absolute values, thus a more symmetric line shape, for increasing intensity. As discussed in chapter 2.3, the q parameter is directly linked to the phase of the dipole response measured in reference to the external field (eq. 2.42). The change in the line-shape symmetry thus derives from a phase shift of the decaying dipole. To investigate the origin of this shift, the state coefficients are further analyzed. The temporal evolution of their phase $\varphi_{k,int} = \arg(c_{k,int})$ is calculated and unwrapped for all states ($k \in g, e$) and intensities (subscript int).

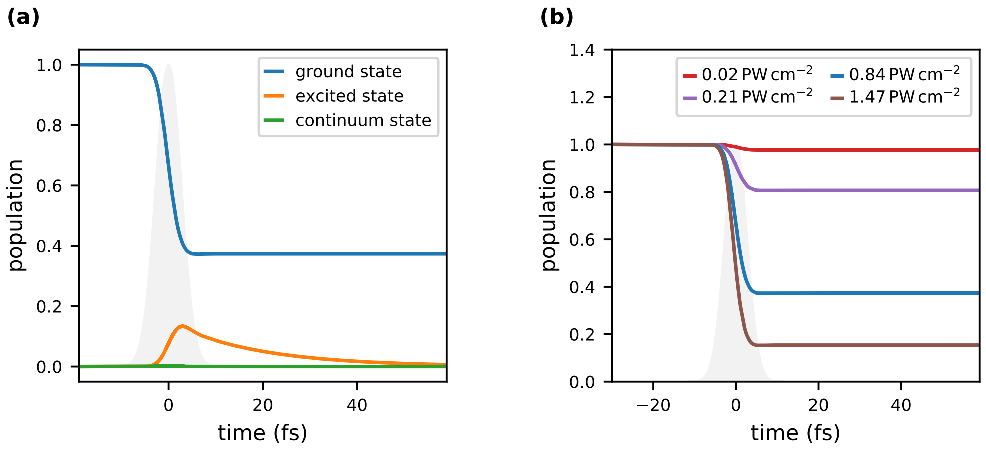

Figure 6.5.: Temporal evolution of the population induced by a 4.6 fs Gaussian XUV pulse. **(a)** Population of the ground, excited and continuum state dressed with 0.84 $\times 10^{15}$ W cm^{-2}. **(b)** Population of the ground state for different pulse intensities.

Then, the excited states' phase evolution is subtracted by the phase of the respective ground state $\varphi_{int} = \varphi_{e,int} - \varphi_{g,int}$ to exclude shifts acting on all states globally. Since the goal here is to extract the impact of intense pulses, only the difference $\Delta\varphi_{int} = \varphi_{int} - \varphi_{int=0}$ to the low intensity case is of interest. It eliminates in particular the accumulated trivial phase originating from the fast oscillation of the excited states' eigenenergies. This procedure is conducted for all intensities, respectively, and plotted for selected intensity values in figure 6.6(a). One can identify a rapid decline of the phase during the pulse. This corresponds to a phase jump in the temporal evolution of the excited state. The amount of this shift is intensity dependent and induced by the XUV pulse.

A more detailed observation reveals a bump at the center of the pulse pointing in the opposite direction of the discussed phase jump. This is attributed to the numeric realization of the continuum in this model. The strong coupling of the ground state to the continuum during the pulse induces transient population of the pseudo. This population follows the pulse instantly and can be observed when magnifying the scale of the continuum state's population in figure 6.5(a) sufficiently. In consequence, this effect can numerically impact the remaining states and cause the observed bump. Therefore, it is not a physical effect. Furthermore, a temporal delay of the phase shift to the peak of the XUV pulse can be observed. This is explained by the fact that the XUV pulse not only dresses the excited state but first needs to populate it significantly to create an observable effect.

The phase evolution of a state is related to its energy due to the solution of the

Schroedinger equation 5.4 and given by:

$$E_k(t) = -\hbar \frac{\partial}{\partial t} \varphi_k(t). \tag{6.1}$$

Thus, one can calculate the temporal evolution of the energy of the excited state $\Delta E_{e,int}(t)$ from the observed phase shift in $\Delta\varphi_{int}(t)$. Note a residual oscillation modulates the phase. Its $2\omega_F \approx 120\,\mathrm{eV} = 34.4$ frequency originates from far off-resonant coupling. Though small in amplitude it exhibits steep flanks, which in combination with the observed overshoot result in a disturbing impact on the differential $\frac{\partial}{\partial t}$ (eq. 6.1). Therefore, the temporal phase evolutions are fitted to eliminate both of these influences. Based on their qualitative shape, with the obvious exception of the above-mentioned bump, the error function is ideal as a fit model for this purpose. With these fitted functions (fig. 6.6(a)) the calculation of $\Delta E_e(t)$ is conducted. Its temporal evolution (fig. 6.6(b)) reveals a transient energy shift caused by the intense XUV field. One can further observe that the magnitude of the energy shift as well as the associated phase shift is intensity dependent.

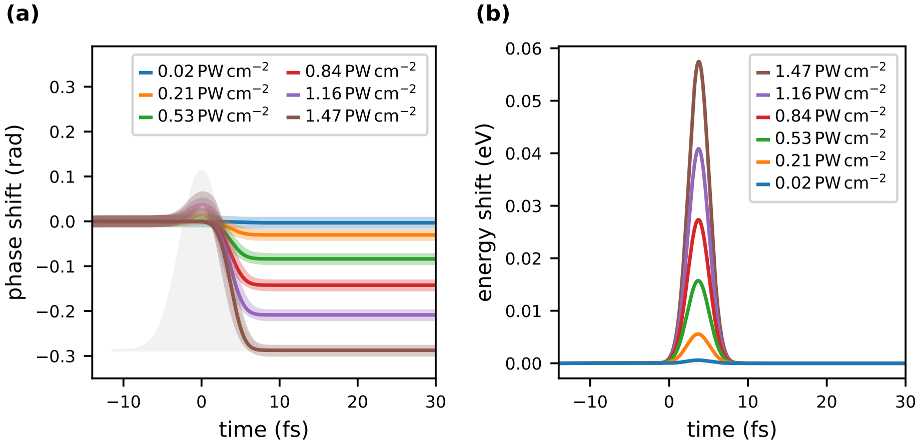

Figure 6.6.: Phase and energy shifts from the numeric model calculation for different XUV intensities. **(a)** Temporal jump of the excited state's phase induced by intense XUV field dressing as calculated (translucent) from the simulated data and fitted (solid) with an error function. **(b)** Transient energy shift of the excited state calculated form the fitted phase shift in (a).

With the origin of the phase jump identified, the phase shift of the excited state is compared to the phase of the dipole response. The latter is evaluated with equation 2.42 from the q parameter of the fit (fig. 6.2(a)). The values (fig. 6.7) of both numeric phases concur over the full intensity range. Slight deviations are attributed to the fact that equation 2.42 is only exactly valid for an impulsive 'kick'-like pulse [25]. The pulse duration of sub-five femtoseconds is slightly above that regime, but the data are still in good agreement. As a consequence, the transient energy shift of the excited state is the dominating factor for the phase shift in the dipole and thus the reason for the observed distortion of the line shape's symmetry.

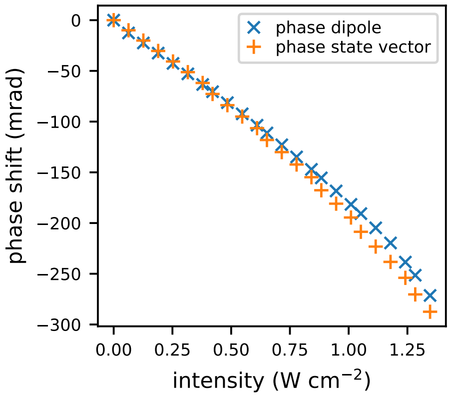

Figure 6.7.: Phase shifts of the excited state and q parameter from the numeric intensity scan. The $\Delta\varphi$ of the asymmetry parameter q determined with equation 2.42 is depicted as blue 'x', the phase shift of the excited state (see fig. 6.6(a)) is plotted as orange '+'.

In conclusion, a distortion of the helium 2s2p absorption line shape in the presence of intense XUV pulses has been observed experimentally. Particularly the symmetry of the resonance is altered by high pulse energies. This result has been qualitatively reproduced by a numeric few-level model simulation with ultrashort Gaussian XUV pulses. The simulation reveals the origin of the symmetry change in reference to the weak-field limit. High intense XUV pulses induces a transient shift of the excited state's energy level. The accumulated phase leads to a phase shift of the dipole response manifesting in the symmetry distortion. Furthermore, as the highly intense fields do not act on the energy position of the resonance, the interaction of the helium target with the XUV pulses can be classified to be in the impulsive regime. This result is consistent with the fact that the duration of the sub 5 fs Gaussian pulses is much shorter than the 17 fs lifetime of the doubly excited state.

6.2. Pulse-Length Effects

The last chapter (ch. 6.1) showed that the 2s2p absorption line shape in helium is altered in its symmetry by intense resonant XUV radiation. The origin lies in the energy-level shift of the excited state during the dressing with the XUV pulse. Intensity spikes of sub-five femtoseconds, which constitute a stochastic pulse, act impulsively on the atomic system.
At the same time, the overall duration of a SASE pulse from FLASH amounts to multiple tens up to one hundred femtoseconds. On the other hand, the lifetime of the autoionizing state is given at 17 fs and thus lies between overall pulse duration and duration of the intensity spikes. Hence, the question can be raised which role the overall duration of the stochastic pulse plays.
To explore this influence, the numeric few-level model simulation is extended to stochastic, SASE-like fields. With these new input pulses the simulation with the helium levels of interest is executed and the results are compared with the experimental and numeric observations of the previous chapter. Afterwards, to single out pulse-duration dependent effects the simulation is repeated for different overall pulse durations. Finally, the findings are compared with the second measurement performed at FLASH with a longer average pulse duration.

To emulate the realistic pulse structure used in the experiments, the few-level model simulation is extended in terms of the input electric fields. For this purpose, the concept of the partial-coherence pulse model is utilized, which is briefly explained in chapter 5.2. As input parameters for the model, the central photon energy of the initial spectral Gaussian envelope is set to 59.7 eV, slightly red detuned to the 2s2p resonance. The precise value of the detuning here is chosen such that the symmetry exhibits a sufficiently strong change, while the resonance is still contained in the average spectrum. In general, the degree of the q parameter change can be adjusted by the detuning [7]. Its spectral bandwidth is 0.4 eV FWHM analogue to the experimentally measured bandwidth of FLASH. The resulting temporal stochastic fields are windowed with a Gaussian envelope corresponding to a short 30 fs overall intensity duration. The simulation conducted in the previous chapter is repeated with these new pulses, utilizing 300 individual stochastic pulses for each pulse energy bin. In the context of simulated SASE pulses, the quantity peak intensity is no longer meaningful due to the fluctuating temporal pulse structure. Instead the quantity

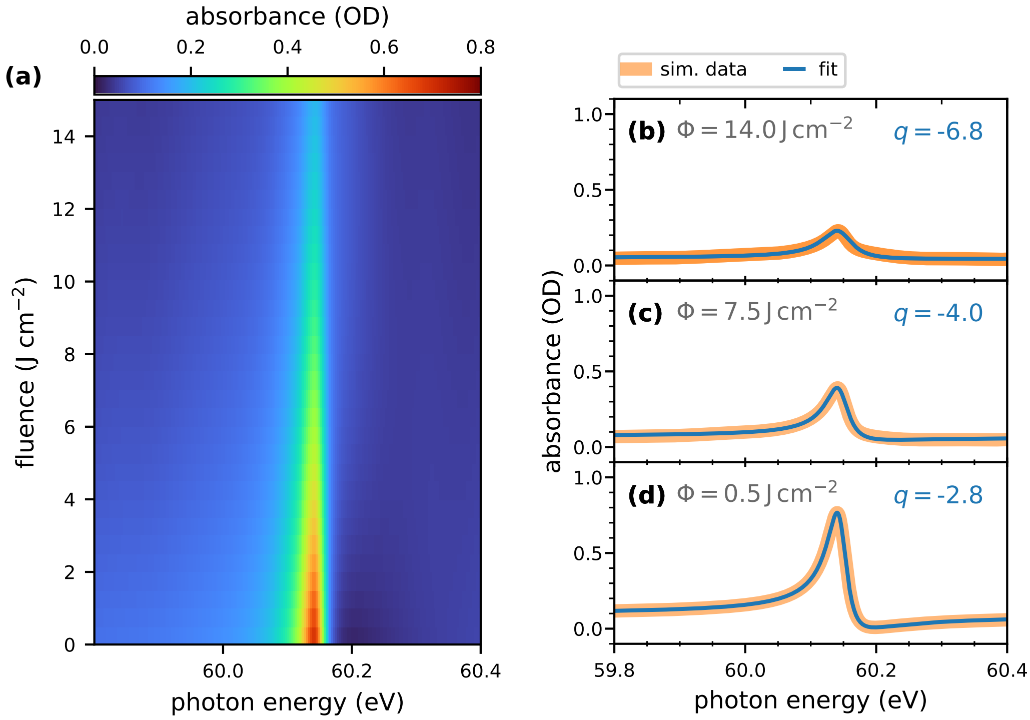

Figure 6.8.: Numeric fluence scan of the He 2s2p resonance conducted with the few-level model simulation using stochastic XUV pulses of 30 fs FWHM overall duration. **(a)** two-dimensional map of the OD for a fluence range between 0.0 J cm^{-2} and 15 J cm^{-2}. **(b)-(d)** OD lineouts as orange translucent lines for selected fluences ϕ noted in the panels. The Fano fits are depicted as blue lines in combination with the respective resulting q parameter.

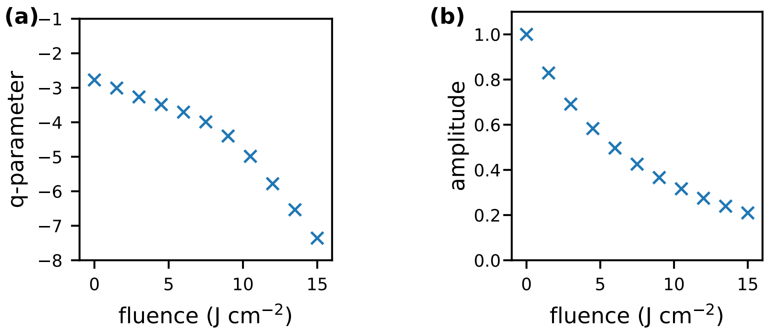

Figure 6.9.: Absorption line parameters extracted from the Fano fit of the simulation data for 30 fs FWHM stochastic pulses in figure 6.8. The results for the **(a)** q parameter and **(b)** line amplitude are depicted over fluence. Hereby, the amplitude is normalized to its highest values in the weak-field limit.

of the fluence (energy per unit area) is utilized, since it describes the temporally integrated intensity of the pulse and is thus independent of the energy distribution within. Therefore, it is a convenient measure for quantification of stochastic pulses.

The simulation is conducted for a fluence scan between 0.001 J cm^{-2} and 15 J cm^{-2} in 0.5 J cm^{-2} steps. The OD is calculated with the time-dependent dipoles and the 300 individual stochastic pulses from the simulation (eq. 2.41 in ch. 5.1.2). The determined OD (fig. 6.8) shows a clear qualitative resemblance to the experimental OD (fig. 6.1). In particular, the decrease in the line-shape's amplitude and change in its asymmetry towards a more symmetric line shape is observed. This is confirmed by the quantification of the line-shape parameters with the fit of the Fano formula 2.43 (fig. 6.9). The normalized amplitude decreases by 80% compared to the weak-field limit while the symmetry parameter q drops from the initial literature value $q = -2.75$ to a value around $q = -7.5$. These findings are in good agreement with the experimental (fig. 6.2) and numeric (fig. 6.4) results of the previous chapter.

To gain insight into the impact of the overall pulse duration of stochastic pulses the above simulation is repeated for a much longer pulse duration of 150 fs (fig. 6.10).

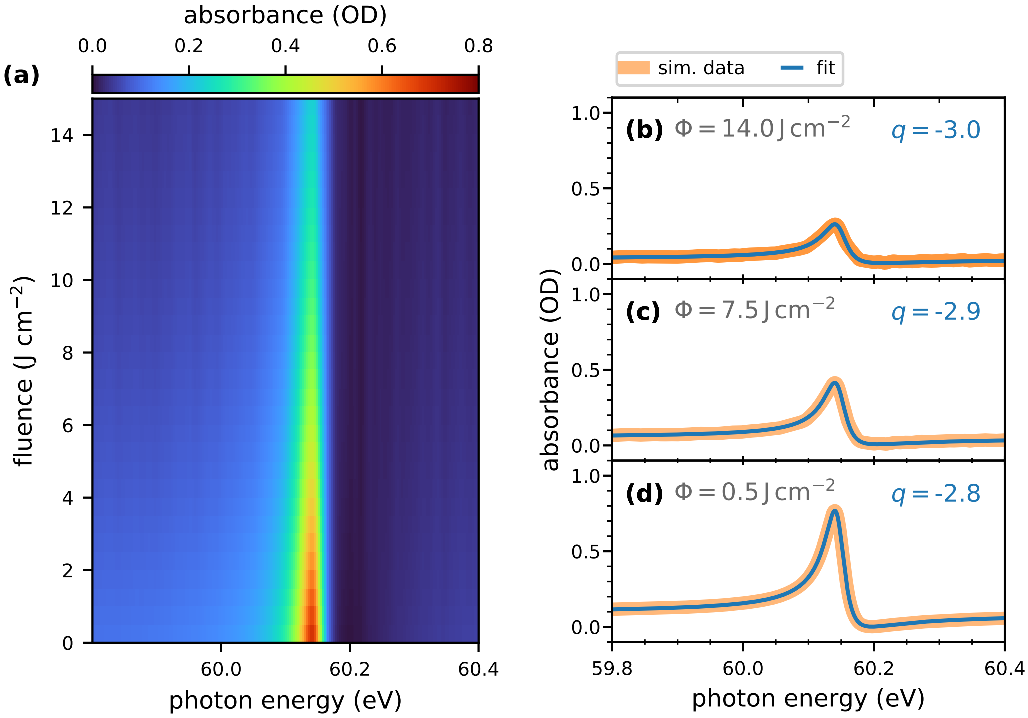

Figure 6.10.: Numeric fluence scan of the He 2s2p resonance conducted with the few-level model simulation using stochastic XUV pulses of 150 fs FWHM overall duration. **(a)** two-dimensional map of the OD for a fluence range between 0.0 J cm^{-2} and 20 J cm^{-2}. **(b)-(d)** OD lineouts as orange translucent lines for selected fluences ϕ noted in the panels. The Fano fits are depicted as blue lines in combination with the respective resulting q parameter.

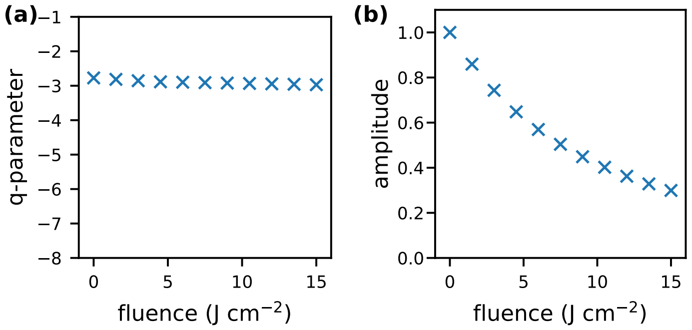

Figure 6.11.: Absorption line parameters extracted from the Fano fit of the simulation data for 150 fs FWHM stochastic pulses in figure 6.10. The results for the **(a)** q parameter and **(b)** line amplitude are depicted over fluence. Hereby, the amplitude is normalized to its highest values in the weak-field limit.

Here, the OD (fig. 6.11(a)) shows a different behavior: The OD minimum can be identified at 60.2 eV at low pulse energies analogue to the 30 fs simulation and the experimental results. In this case, though, this minimum remains for the entire fluence range. This is underlined by the representative absorption lines depicted in figure 6.10(b)-(d), which exhibit a remaining visible asymmetry even for high fluence. At the same time, the amplitude decreases qualitatively similarly to the numerical short pulse case above.

The quantification of the OD by fitting equation 2.43 confirms these observations. It reveals that the normalized amplitude declines in to about 30 %, which is in the same regime as the short-pulse case. Furthermore, the asymmetry parameter remains around $q = -2.75$ in contrast to the $q = -7.5$ for 30 fs overall pulse duration. Two conclusions can be drawn from these results:

First, despite the noticeable difference in symmetry behavior, the manner and magnitude of the decrease in amplitude is almost identical and hence independent of the pulse duration. Therefore, the absorption line strength, associated with the line shape amplitude of the measured spectral intensity, is dominated by the fluence of the SASE pulse and independent of the strong coupling effect manifesting in the symmetry distortion. The normalized decrease of the amplitude can thus potentially serve as a fluence metric, indicating the amount of fluence seen by the target. This enables the comparison of results from different experimental measurements and numerical simulations.

Secondly, the overall pulse duration of the stochastic fields has a strong impact on the observed line-shape symmetry change. To gain further insight into that relation, a systematic scan of pulse duration, between 20 fs and 180 fs, at a high fluence of

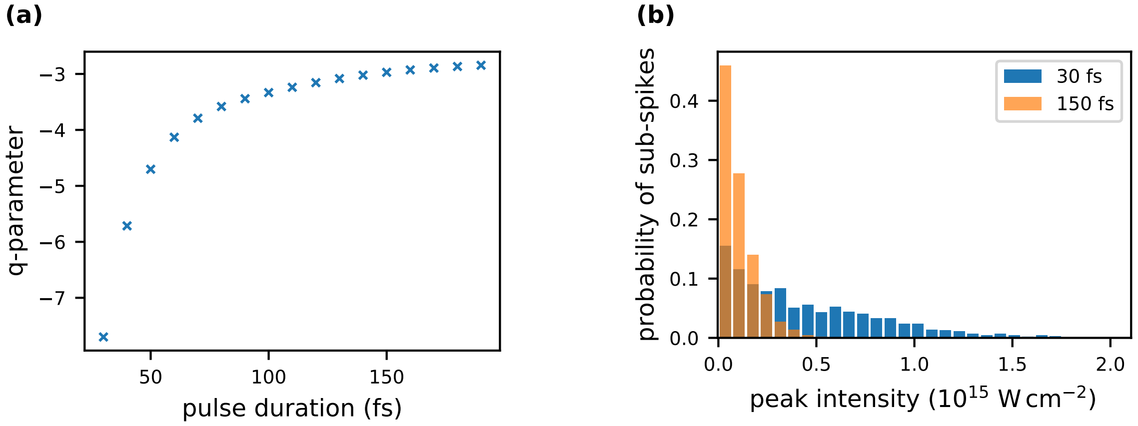

Figure 6.12.: **(a)** Pulse duration scan of the few-level model simulation for pulse envelops between 20 fs and 180 fs FWHM at a fluence of 15 J cm^{-2}. **(b)** Intensity spike analyse of numeric SASE pulses at a fluence of 15 J cm^{-2} for pulse envelops of 30 fs (blue) and 150 fs (orange) FWHM. Here, the top three intensity spikes of each pulse are evaluated for 100 stochastic pulses.

15 J cm^{-2} is performed with the simulation. The OD is calculated from 200 individual stochastic pulses for each pulse duration. The resulting ODs are fitted with the Fano formula 2.43 and the symmetry parameter q is extracted (fig. 6.12(a)). For long overall pulse durations above 100 fs the q parameter approaches asymptotically the literature value, to which the simulation is calibrated to ($q = -2.75$). With shorter pulse envelops the q parameter exhibits a steep decline and hence the line-shape symmetry a strong distortion towards a more symmetric line shape. This sensitivity to the pulse duration manifests for pulse envelops far longer than the lifetime of the autoionizing state (17 fs). Thus, the physical cause of the pulse-length sensitivity is expected to originate from the temporal intra-pulse structure of the stochastic pulses for shorter pulse durations.

In the previous chapter 6.1 it has been observed that a small intense, coherent spike of a few femtoseconds duration leads to the strong-coupling effect of a symmetry change. Since the stochastic pulse contains several of such short intensity spikes in the temporal domain (fig. 5.1), the peak intensity of these spikes is analyzed for the cases of 30 fs and 150 fs overall duration. For that purpose, the intensity of the three largest temporal features within each pulse is evaluated for 100 simulated pulses (fig. 6.12(b)). One can directly identify that the peak intensities of the intra-pulse intensity spikes are limited to 0.5×10^{15} W cm^{-2} for the 150 fs pulse envelope. On the other hand, for shorter 30 fs pulses the probability distribution of the peak intensity reaches beyond that and up to 1.5×10^{15} W cm^{-2}. This result is conclusive with the observation from the previous chapter 6.1, where a line-shape transformation becomes evident at peak intensities in the upper $10^{14}\,\mathrm{W\,cm^{-2}}$ regime. Therefore, the intra-pulse energy distribution for shorter pulses at a constant fluence leads to higher peak intensities within the SASE pulses. Furthermore, it can be concluded that the observed line-shape symmetry change originates predominantly from the impulsive strong coupling with individual highly intense intra-pulse features. This means in turn that the energy is distributed on a few spikes, stochastically separated in the time domain. One can thus regard these intensity spikes as sequential 'micro-experiments' within one pulse.

For an experimental validation, a second measurement campaign is carried out with similar FLASH pulse parameter settings but at a longer pulse duration. In addition to the rough estimation of 100 fs FWHM average pulse duration by the LOLA device at FLASH (chp. 3.1), a spectral analysis is performed.
For this purpose, the spectra of the SASE pulses are Fourier analyzed. This method works on the basis that a longer pulse envelope contains on average a larger number of intense spikes. These interfere spectrally and lead to a modulation of the measured spectra. Here, a higher number of pulses lead to a higher modulation frequency detectable via the Fourier transformation. Hence, the Fourier transformation of the individual XUV pulses is calculated and averaged for several pulses of one pulse setting. In figure 6.13 one can observe the sharp DC peak overlapped with a broad spectrum of Fourier components of the spiky SASE spectrum. This broad wing is fitted with a Gaussian function to determine the distribution of these frequency components. The

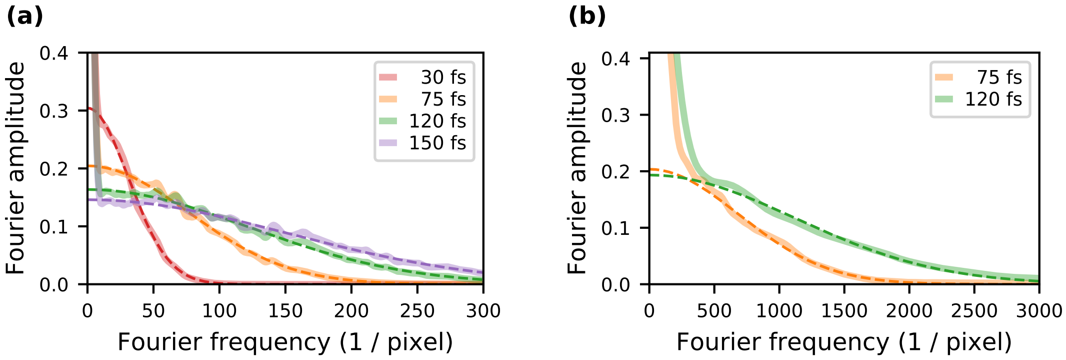

Figure 6.13.: Fourie analysis of single-shot spectra. The results are averaged for each pulse duration (translucent line). The broad distribution beyond the DC peak is fitted with Gaussian function (dashed line). **(a)** PCPM simulated pulses for different overall FWHM durations. **(b)** Experimental data from the first (orange) and second (green) measurement. The Gauss for the second measurement has 1.6 times the width of the first experiment and thus the pulse average duration of the second experiment is estimated to 120 fs.

set pulse duration	calculated pulse duration
30 fs	-
75 fs	74.6 fs
120 fs	118.4 fs
150 fs	146.7 fs

Table 6.1.: Overall durations of numeric SASE pulses calculated with the Fourier analysis method and compared to the input pulse durations in the PCPM.

resulting quantity of the *half width at half maximum* is used as the relative measure for the spikiness of the SASE spectrum.

With the PCPM at hand, this method is put to the test for various pulse durations set in the model, see figure 6.13(a) and table 6.1. The durations set in the PCPM as the input are in good agreement ($\approx 2\%$) with the results from the Fourier analysis calculated in relation to the 30 fs. Thus, this procedure allows for a estimation of a pulse duration relative to a reference dataset.

The method is applied to the experimentally measured data to estimate the pulse duration of the second measurement relative to the first one. Since the BL spectrometer exhibits sharper spectral features than the reference spectrometer, it has a higher resolution and its spectra are chosen for this method. The recorded spectra of both measurement campaigns without a target in the focus are analyzed and compared. Figure 6.13(b)) reveals the pulse duration of the second experiment to be a factor 1.6 larger than in the first experiment, which has been determined at 75 fs. Hence, this method indicates a pulse duration of about 120 fs FWHM for the second experiment.

The data measured in the second experiment are evaluated analogously to the first experiment with equation 4.2 and in accordance with chapter 4.3. Figure 6.14 depicts the resulting OD. The lineouts show a declining amplitude with increasing pulse energy. This observation is consistent with the first experiment. At the same time, no clear trend towards a more symmetric line shape can be qualitatively identified, particularly in the lineouts (6.14(b)). The OD is fitted with the Fano formula 2.43 for quantification, which is convoluted with the spectrometer resolution before the optimization algorithm is applied. This, as well as the determination of the statistical uncertainty, are carried out exactly as in the first experiment. The fit results (fig. 6.15) confirm the decrease in normalized amplitude to about 40%. This is on the same order of magnitude as the first experiment within the same range of pulse energy.

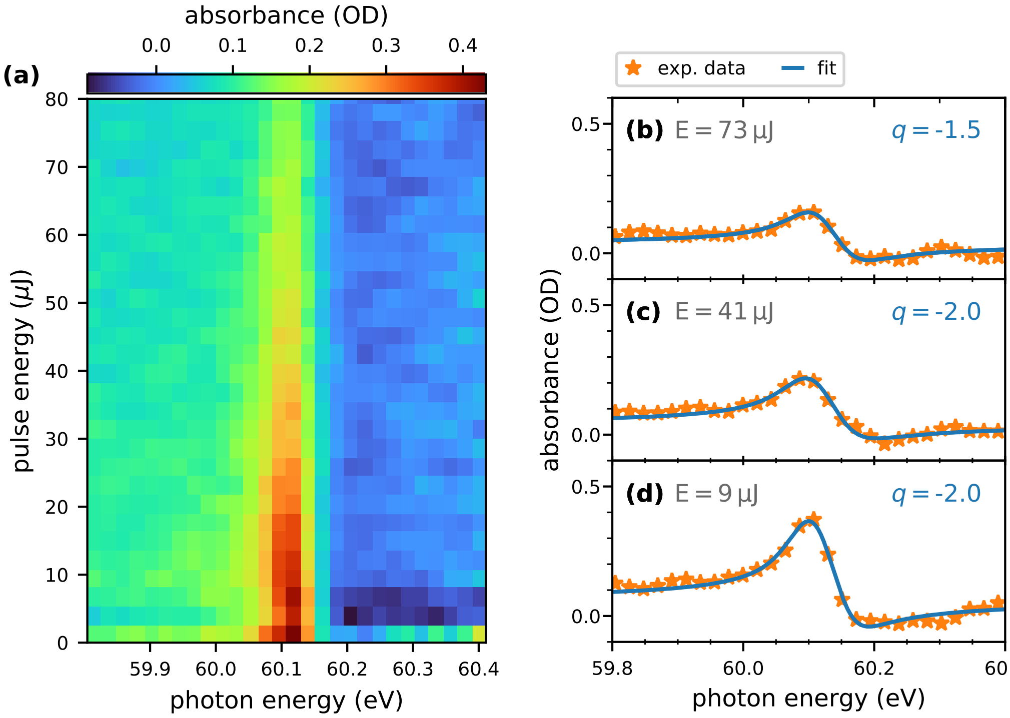

Figure 6.14.: Experimental pulse-energy scan of the He 2s2p resonance using 130 fs FWHM overall duration XUV SASE pulses. **(a)** two-dimensional map of the OD for a pulse-energy range between 0 µJ and 80 µJ. **(b)-(d)** OD lineouts as orange stars for selected pulse energies E noted in the panels. The Fano fits are depicted as blue lines in combination with the respective resulting q parameter.

Hence, the fluence seen by the target in both experimental campaigns is similar. This follows from the finding made above that the amplitude decline is connected to the fluence by the linear absorption process. The here observed symmetry parameter of the absorption line remains close to the initial value at low pulse energy. The distortion towards a more symmetric lineshape seen in the first experiment can not be observed (fig. 6.14(b)).

In conclusion, the numeric few-level model simulation employing stochastic SASE pulses has shown results in good agreement with the Gaussian pulse simulation in the previous chapter 6.1. Furthermore, a dependency of line symmetry distortion on the overall pulse duration of the stochastic pulses has been observed. It has been identified that the strong coupling is dominated by single intensity spikes within the pulse envelope. Hence, nonlinear experiments on the timescales shorter than the 17 fs lifetime of the autoionizing 2s2p state in helium can be performed with SASE pulses, even when their overall pulse durations far exceeds this timescale.

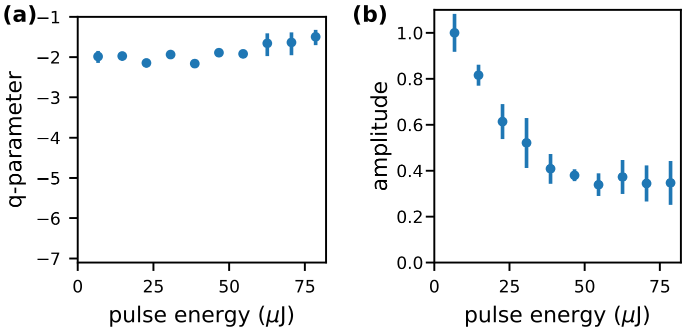

Figure 6.15.: Absorption line parameters extracted from the Fano fit of the experimental data in figure 6.14. The results for the **(a)** q parameter and **(b)** line amplitude are depicted over pulse energy. Hereby, the amplitude is normalized to its highest values in the weak-field limit.

6.3. Line-Width Broadening

The symmetry of the helium 2s2p absorption line and its manipulation has been in the focus in the previous chapters 6.1-6.2. Now, a different parameter of the absorption line, the line width, and what we can learn from its behavior in intense XUV fields is thoroughly investigated. In principle, the spectral width of a decaying dipole is intrinsically connected - via the Fourier transformation - to its lifetime (ch. 2.3). In consequence, the analysis of the line width can provide insights into the dynamics of the doubly excited state dressed with intense XUV fields.

The investigation is conducted on the experimental data set of the second measurement at FLASH, already subject of the previous chapter 6.2. Here, the SASE pulses of 120 fs overall duration exhibit a central photon energy of 60 eV with a bandwidth of 0.4 eV FWHM. The pulse energy reached up to 80 µJ per pulse and is scanned with the gas attenuator. For the evaluation of the line-width change, the number of pulse-energy bins is reduced to seven bins in this case, resulting in at least 1500 single shots per bin. This compensates a low signal-to-noise ratio in the line width parameter.

The data are otherwise evaluated analogue to the previous chapter with equation 4.2 and according to chapter 4.3.

First, to verify consistency, one can observe that the OD in Figure 6.16(a) is in qualitative agreement with the experimental results in the previous chapter concerning the line-shape amplitude and the asymmetry (fig. 6.14). Since only a different choice of bin size marks the difference here, the reader is referred to the previous chapter 6.2 for the discussion of the amplitude and symmetry parameter. The chosen illustration

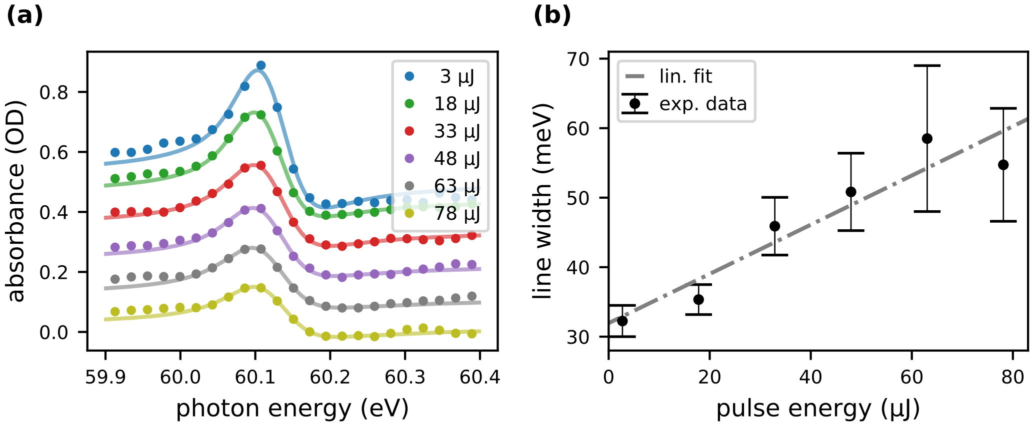

Figure 6.16.: Experimental pulse-energy scan of the helium 2s2p resonance. **(a)**: OD measured with XUV SASE pulses of 120 fs FWHM overall duration for different pulse energie bins. Note, for visualization the lineouts are shifted on the OD axis by an offset of 0.1 each, starting from the lowest lineout. The measured ODs (dots) are fitted with the Fano-formula (solid lines). **(b)** Line width extracted from the fit (a). The resulting line width parameter is linearly fitted to illustrated the trend.

(fig. 6.16(a)) with a 0.1 offset per lineout in OD already allows for the identification of a broadening in the absorption line with increasing pulse energy. In continuation of the previous chapters, its quantification is conducted with the fit of the Fano formula (eq. 2.43). The ensemble is split into three equally sized subsets per bin and evaluated individually for the statistical uncertainty. Its results for the line width parameter reveal a significant increase over the pulse energy range (fig. 6.16(b)). The width parameter starts at 33 meV for the lowest pulse energies, slightly lower than the 37 meV literature value [40]. It increases up to $\sim$ 60 meV at the highest XUV pulse energies, effectively doubling the initial value. Here, at higher pulse energies, the standard deviation exhibit large values. This is attributed to lower FEL pulse statistics and thus low signal-to-noise ratio. However, a trend can be identified over the full pulse energy range and quantified with a slope of 0.27 $\mathrm{meV\,\mu J^{-1}}$ provided by a linear fit. These observations motivate the question to the physical origin of the line width increase.

To investigate impacting factors leading to the observed broadening of the absorption line a numerical simulation, introduced in chapter 5 and utilized in the previous chapters 6.1-6.2, is conducted. Possible reasons for the broadening are connected to the modification of the average lifetime of the autoionizing state. Therefore, an increased coupling of the doubly excited state to the ground state by the intense XUV fields has to be considered. Another mechanism is the ionization of the excited state with a second photon, coupling it to the n=2 continuum of the He$^+$ ion. Therefore, a general, intensity-dependent loss channel is introduced to the excited state by adding the imaginary quantity $i \cdot \Gamma(t)/2$ to its eigenenergy in the Hamiltonian

$$H(t) = \begin{pmatrix} E_g & d_{ge}^{*}\cdot\tilde{F}(t) & d_{gc}^{*}\cdot\tilde{F}(t) \\ d_{ge}\cdot\tilde{F}(t) & E_e+i\cdot\Gamma(t)/2 & V_{CI}^{*} \\ d_{gc}\cdot\tilde{F}(t) & V_{CI} & E_c \end{pmatrix}. \tag{6.2}$$

For the loss rate $\Gamma(t)/2$ a linear absorption is assumed, making it proportional to the intensity

$$\Gamma(t) = \sigma \frac{I(t)}{\hbar\omega}. \tag{6.3}$$

Note the Hamilton is now split into three instead of two parts for the numeric calculations (compare to ch. 5.1.2), a constant, a field-dependent and an intensity-dependent part. Since the input field is an XUV pulse the latter two parts are time dependent.

The photo-ionization cross section of ground-state beryllium is chosen for the cross section of the additional loss channel. Its electron configuration (1s^{2}2s^2) has the two energetically higher lying electrons in the n=2 shell, analogue to the He 2s2p state. At the same time, the remaining two electrons shield the nucleus creating in first approximation a 'pseudo' helium-like system.

The photo-ionization cross section $\sigma_{\mathrm{Br}} = 0.336$ Mbarn at 60 eV [87] will hence serve as the initial value for the cross section of the additional loss channel in the numeric model.

The simulation is conducted with stochastic pulses of 130 fs FWHM overall duration and in consistency with the previous chapter at a central photon energy of 59.7 eV and a 0.4 eV FWHM bandwidth. The fluence range is increased slightly to an upper limit of 30 µJ cm^{-2} to increase the visibility of the line broadening effects. In this case the simulation is performed for 400 stochastic pulses per bin to keep the statistical uncertainty in line width introduced by the stochastic nature of the simulated SASE pulses at an insignificant level far below 1 meV. The OD is determined from the XUV fields in combination with the computed dipoles, analogue to the previous chapter, utilizing equation 2.41. In figure 6.17(a) (translucent line) the qualitative behavior of the OD can be observed. It reproduces the experimental results (fig. 6.16(a)) in terms of the decreasing amplitude and the retained symmetry. These parameters and their behavior have been discussed and explained in the previous chapter 6.2.

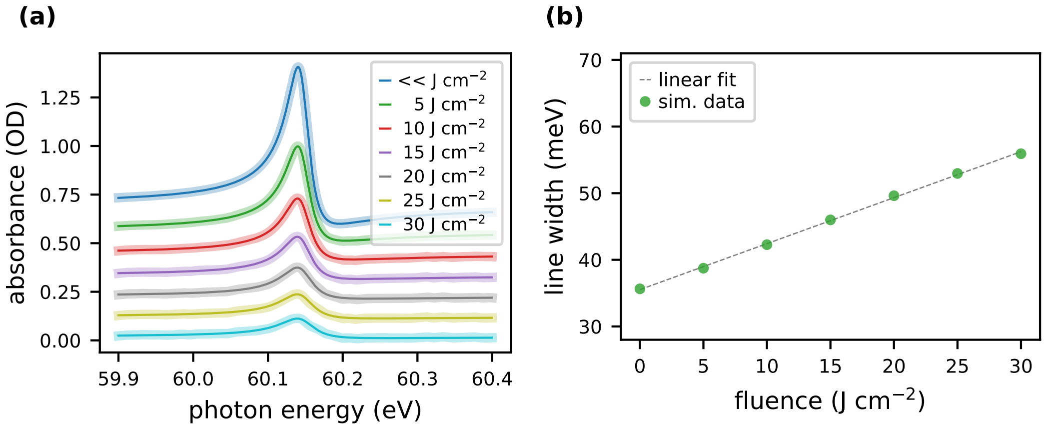

Figure 6.17.: Few-level model simulations of the helium 2s2p resonance with 400 numeric stochastic XUV pulses per bin. **(a)** OD calculated with pulses of 130 fs FWHM overall duration. This simulation is conducted with an additional loss-channel in the excited state ($\sigma = 0.336\,\mathrm{Mbarn}$). The lineouts of the OD (thick and translucid) are fitted with the Fano formula (thin and opaque). For illustration purposes, the sequential lineouts starting from 30 J cm^{-2} are shifted by a 0.1 offset in OD. **(b)** Simulated line width extracted from the fit in (a). A linear fit (dashed) indicates the trend.

For the analysis of the effect of interest here, the absorption line broadening, the line width is quantified by fitting the Fano formula 2.43 (see fig. 6.17(a), opaque). The result for the line width parameter (fig. 6.17(b)) confirms an increase. Starting around the low-intensity literature value of 37 meV [40] to which it has been calibrated, the resonance width broadens by about 20 meV over the fluence range. A linear fit provides a slope of 0.67 meV μJ^{-1} cm^2. Overall, a trend in the order of magnitude of the experimental line shape broadening can be identified. A more precise comparison of this quantity is not possible due to the impact of measurement uncertainties, e.g. the focus size, GMD precision and loss in the BDA.

As the fluence-dependent broadening of the resonance has been established with the numerical model, it can be utilized for a further investigation of the mechanisms that contribute to this effect. Thus, the influence of the additional loss channel, which represents the radiation-induced decay, is varied.
The computation is repeated for a set of cross sections $\sigma \in \sigma_{Br} \cdot \{0, 0.5, 1.5\}$, which also includes the absence of an additional loss channel ($\sigma = 0$). Proceeding in the same way as above, the OD is evaluated and directly quantified. The determined absorption line width (fig. 6.18(a)) shows a clear rising trend with increasing fluence for all cross sections. Motivated by the equidistant spacing of the line width for each fluence and the linear dependency in equation 6.3, the dependency of the line width

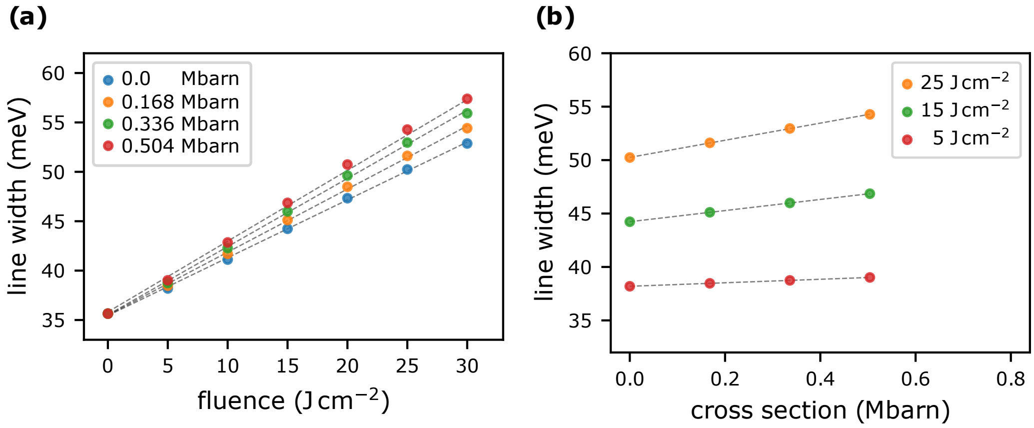

Figure 6.18.: Line width extracted with the Fano formula fit from the OD of the few-level simulation fluence scan of the helium 2s2p resonance. In extension to figure 6.17(b) the simulation has been conducted for different values of the loss channel cross section. **(a)** Line width over fluence. **(a)** Line width over the cross section of the additional loss channel. A linear fit (dashed) indicates the trend.

on the loss-channel cross section is analyzed (fig. 6.18(b)). Here, a linear relation of the line width and the cross section can be directly observed.

A second and even more interesting physical insight is also provided by the fluence dependency in figure 6.18(a)): The dominant feature of the broadening is a general mechanism acting on the line width even in the absence of the additional loss channel ($\sigma = 0$). For this case, the original Hamiltonian (eq. 6.2) contains no other field dependencies than the off-diagonal dipole coupling elements. Therefore, the origin for the increase in width of the resonance line is the coupling back of the excited state to the ground state. This results is an effective shortening of the average lifetime with increasing fluence, which leads to the broadening. Note while this effect is induced by the strong coupling of the states, it is present even at pulse durations and thus peak intensities where a line symmetry distortion is not yet acting. This allows for the isolated exploration of the line-width-broadening effect here.

In conclusion, the broadening of the resonance line shape has been observed experimentally for high pulse energies. This effect has been predominantly attributed to the increased coupling of the doubly excited state to the ground state in the presence of intense XUV fields with the numeric model. At the same time, the impact of the photo-induced coupling of the excited state to the n=2 continuum is not found to be a significant factor for the line shape broadening and thus manipulation of its lifetime.

7. Conclusion

The goal of this thesis is to deepen the understanding of electronic interactions within atomic systems on a quantum-mechanical level. Therefore, the fundamental three-body system of helium is explored under the influence of extreme electromagnetic fields. Specifically, the spectroscopically isolated two-electron resonance 2s2p is investigated with resonant, high-intensity and ultrashort XUV pulses at an FEL. To this end, a novel and flexible transient absorption beamline is built and pulse energy scans are conducted at the large-scale facility FLASH providing high-intensity XUV radiation. The measurements presented, discussed and analyzed within this work represent the first TAS experiments of the doubly excited state in helium in intense XUV SASE fields. To quantify the impact of the intense XUV fields on the helium atom, the 2s2p absorption line-shape symmetry, amplitude and width distortions are analyzed in detail and compared to few-level quantum-mechanical numerical simulations.

As a first result from the performed measurements at FLASH, the modification of the typical Fano line shape of the 2s2p resonance under the influence of intense 75 fs SASE XUV pulses is experimentally observed. It transforms towards a more symmetric line shape with increasing XUV pulse energy. The observation is investigated with a few-level model simulation. For this simulation, Gaussian XUV pulses are used. This is motivated by approximating a single intensity spike within the complex FEL SASE pulse structure with a Gaussian function. Thus, the impact of the single intensity spikes within the pulse on the helium atom is examined. The simulation shows that the origin to the symmetry change is a transient phase shift of the doubly excited state's energy level manifesting in a phase shift of the dipole response. This comes into effect beyond peak intensities of about $0.5 \times 10^{15}\,\mathrm{W\,cm^{-2}}$. Furthermore, the resonance position is not influenced significantly. This characterizes the interaction as being in the impulsive regime, which is conclusive with regard to the 17 fs lifetime of the autoionizing 2s2p state and pulse durations for an intra-pulse intensity spike on the order of 5 fs.

Afterwards, the simulation is extended from Gaussian input fields to more realistic stochastic SASE-like pulses. Here, the influence of the overall pulse duration is explored. The simulated pulse-duration scan reveals that the q parameter is strongly dependent on the SASE pulse envelope. By contrast, the amplitude is independent of the pulse envelope and thus of the intra-pulse intensity structure while its decrease is dominated by the on-target XUV fluence. The line strength decline is hence governed by linear absorption.

An analysis of the simulated SASE pulses shows a significantly different probability of high intensity spikes with respect to the SASE envelop. The shorter 30 fs pulses reach peak intensities of $1.5\ \times 10^{15}\,\mathrm{W\,cm^{-2}}$ while the longer 150 fs pulses only achieve maximum peak intensities up to $0.5\ \times 10^{15}\,\mathrm{W\,cm^{-2}}$. Hence, the observed pulse-envelope dependency of the dressing effects is due to the energy distribution within the pulse. Since symmetry changes only appear for short pulses and at high fluences we can summarize the findings as follows: For a not saturated target, the few most intense single spikes within the pulse envelope predominantly drives the light-matter interaction leading to the strong coupling effect that manifest in the line-shape symmetry change. Thus, the line-symmetry distortion is dominated by individual spikes. With the intensity peaks shorter than the lifetime of the autoionizing state on the order of 5 fs, the interaction can be classified to be in the impulsive regime, even though the overall pulse duration ($\sim$ 100 fs) is much longer than the autoionizing lifetime. Since the intensity spikes are randomly distributed within the pulse envelope, a stochastic SASE pulse can be considered to conduct a sequence of micro experiments. Their dipole response is combined and the average is detected by the spectrometer via the absorption spectrum.

These numeric observations are supported by a second experiment conducted at FLASH with longer 120 fs SASE pulses. Here the absence of the strong-coupling induced line shape modification is observed while the amplitude trend is reproduced.

Finally, the resonance line width is investigated in presence of intense XUV fields. To that end the absorption line in the second experiment is analyzed. One key observation is that intense resonant fields lead to a broadening of the absorption line. The channels contributing to this effect have been numerically investigated: A coupling of the 2s2p excited state to the n=2 continuum of He^{+} has been identified to induce a line shape broadening. It is found though, that this is overwhelmed by the effect of strong coupling from the excited 2s2p state back to the ground state, cf. [88]. Thus, the lifetime of the autoionizing state can be manipulated in single-color experiments by only using XUV radiation. These observations are similar to electron-spectroscopy measurements investigating Auger decay processes as reported by Kanter et al. [89]. At this intensity level, the above discussed strong-coupling induced line-shape symmetry changes do not come into play yet. Thus, the strong-coupling line-shape broadening aspects have to be considered at even lower intensities before line-symmetry distortions occur.

Overall, strong-coupling of a short-lived two-electron transition by an intense XUV dressing field is observed, explained and controlled. Consequently, the physical insights discussed in the course of this thesis will be of great value for future SASE-based spectroscopy and imaging studies at intermediate to high intensities.

The detailed understanding of the 2s2p line-shape distortions under the influence of intense XUV fields does not only deepen our understanding of fundamental light-matter interaction in atomic systems but paves the way for new technical advances in the field of FEL characterization [5]. Furthermore, the discussed processes have implications for studies employing coherent control schemes at intense XUV sources [90–93]. This work will inspire future experiments that use a more controlled high-frequency FEL light source, which has recently become available in form of seeded FELs, e.g. Fermi located in Italy [52]. In addition, the findings will become highly relevant for spectroscopic experiments with another class of novel XUV sources: The rising performance of tabletop systems is closing the gap to the FEL-intensity regime and already offers fully coherent, medium intensity XUV pulses [94, 95]. Also, conducting investigations into many-electron systems has the potential to build upon the findings of this thesis and overcome the gap to more complex atomic systems, e.g. neon. In addition, a particularly interesting exploration would be a time-dependent one-color two-pulse pump-probe-like experimental scheme in the femtosecond regime, complementary to the investigations already performed and published in the VIS and IR spectral range [25, 29]. Further extending this approach leads to multi-dimensional spectroscopy. This technique established a whole scientific field in chemistry and biology using IR/VIS pulses [96–98]. Thus, it is expected that an extension to core-level states by employing XUV fields will have disruptive impact on physical/chemical sciences by its ability to disentangle populations and coherences of core-level, site-specific electronic excitations [99, 100].

A. Appendix

A.1. Acronyms

BDA	beam-distribution array
BL	beamline (meaning the home-build setup)
DAQ	data acquisition
FEL	free-electron laser
FLASH	Free-Electron Laser in Hamburg
FWHM	full width at half maximum
GMD	gas-monitor detector
IR	infrared
OD	optical density
PCPM	partial-coherence-pulse model
SASE	self-amplified spontaneous emission
SE	Schrödinger equation
SXR	soft x-ray
TAS	transient absorption spectroscopy
VIS	visible
VLS	variable line-space grating
XUV	extreme ultraviolet

A.2. Raw Spectrometer Data

Figure A.1 shows example raw images recorded with the XUV camera of the spectrometer.

The calibration of the energy axis has been performed as described in chapter 4.2. Its results are documented in table A.1, while the lineouts can be observed in chapters 6.1 and 6.2 in the experimental sections for the low pulse energy regime. In general, the pixel exhibit a linear relation to the wavelength of the dispersed light determined by the grating equation. In the context of this work though, the energy calibration has been performed linear in photon energy. This approximation is valid as the considered relative spectral bandwidth of 0.4 eV FWHM at 60 eV is $\Delta\lambda/\lambda < 1\,\%$. Furthermore, the absorption-line width of the considered resonance (37 meV) is even smaller by about one order of magnitude. To underline the validity of this approach, figure A.2 shows equidistantly spaced wavelengths points over the considered bandwidth calculated in photon energy. No significant difference to the linear approximation of the photon energy can be identified, classifying the spectrum as sufficiently small for this approach.

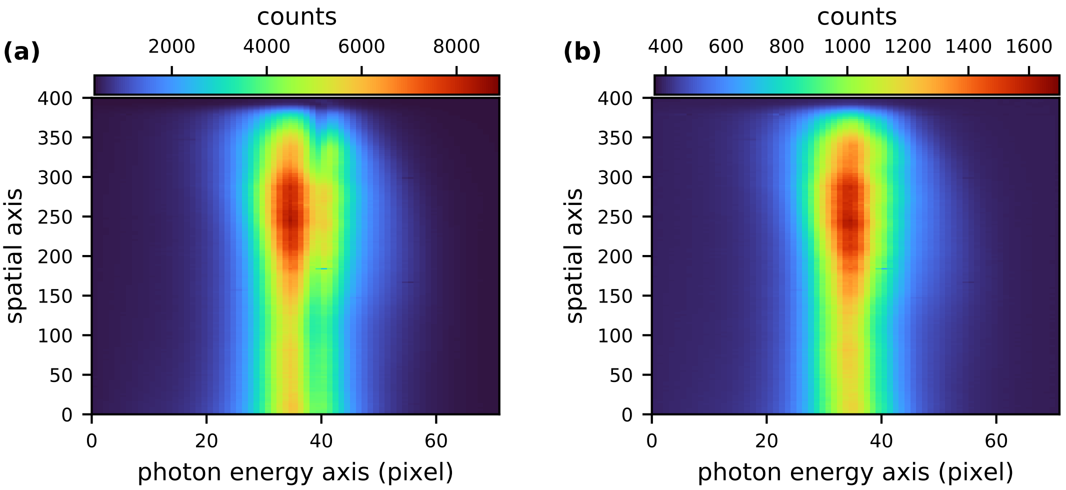

Figure A.1.: Images recorded by the XUV camera in the spectrometer at the second measurement campaign, averaged over 1000 single pulses. In **(a)** the dip of the absorption line of the helium 2s2p can be clearly identified. In comparison to **(b)**, where a measurement without target gas is depicted, one can further identify an enhancement beyond pixel 40 originating from the negative resonant absorbance of the Fano spectral line. This increase is visible due to the normalization of the color scale to the maximum value.

	a (eV/pixel)	b (eV)
first campaign	0.02195	46.788
second campaign	0.02166	59.306

Table A.1.: Spectrometer calibration values of the first and second measurement campaign in linear approximation of the photon energy ($energy = m \cdot pixel + b$). The significant difference in the offset b originates from a different position of the spectrum on the CCD chip.

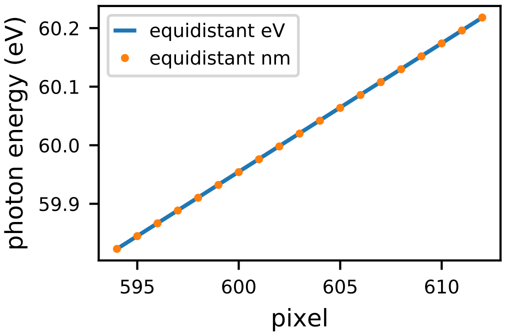

Figure A.2.: Illustration of the linear approximation of the relation photon energy to the pixel of the spectrometer camera, exemplary at data from the first measurement campaign. The values of 59.8 eV and 60.2 eV, equivalent to the range of the measured FLASH spectrum, are calculated in wavelength and equidistantly interpolated. The resulting values are calculated in photon energy (orange) and compared with the linear plot of the photon energy over pixel index (blue).

A.3. Experiment Software

This section provides a short overview over the entirety of the programs designed to drive the motorized and electronic devices on the presented multi-purpose beamline. It further details key feature to provide the reader with a quick understanding on how to operate and further develop the program framework.

The experimental setup is designed for experiments beyond the intensity scan presented in this work. To that end, large numbers of motorized translation stages, tilt stages as well as apertures in form of irises and two-dimensional slits have to be controlled. Furthermore, the gas pressure as well as the recording devices, here an XUV camera, are driven. Each device or group of devices has a physical controller at the beam line. For each physical controller (A, B, . . .) an individual stand alone program, a program instance, exists to address, control and drive its connected axes (X.a, X.b, . . . with X $\in$ {A, B, ...}). The program instances in general consist of three major parts, the *initialization* of the connection, the *operational* loop and the *closing* of the connection to the physical controller.

The signal connection between the main computer and the physical controller is realized via ethernet connections where possible, which compared to other connection types (e.g. USB) allow for a simple and un-ambiguity handshake during the initialization of the connection as well as a reliable connection and flexibility when using multiple computers. During the operational mode, the axes connected to the controller can be calibrated, manually adjusted (e.g. for alignment) and read out via the controller instance's graphic control panel. In addition to the direct access, an option for an external control allows for the operation of the connected devices by an external program instance, e.g. the main experiment program. If activated, no further input on the control panel is accepted to eliminate accidental disturbance by the user. The communication with an external instance is realized with a so-called global variable (fig. A.3), which is an instance containing a set of various variables in LabView. In addition, the globals also contain variables for the actual current position of the axes position, which are written independently of the remote control status. They can be used for recording of the axes position to the data files as well as for live analysis programs. The latter take the data directly from the globals and do not interfere with the data storage process and can be programmed to show preliminary trends and results during the experiment. The actual execution steps of the experiment are programmed into the main experiment instance (see fig. A.4). For simple application and adjustment

of the main experimental instance the communication with the controller instances in encapsulated in sub-programs, which manage the communication (fig. A.5).
Beyond all kinds of motorized stages, the structure is designed such, that also e.g. the control of the FLASH facilities interface DOOCS can be implemented very easily, as well as other types of devices, regardless of the particular structure of the individual controller instance. While being capable for addressing a multitude of devices only the controllers necessary for the respective measurement procedure have to be connected physically and their controller instance running. Then, all other supported but not needed devices are not demanded by the program, but their values are logged when their instance is running during the experiment. This required a little effort on the programming side but provides huge flexibility in the application of the framework at such a multi-purpose beamline.

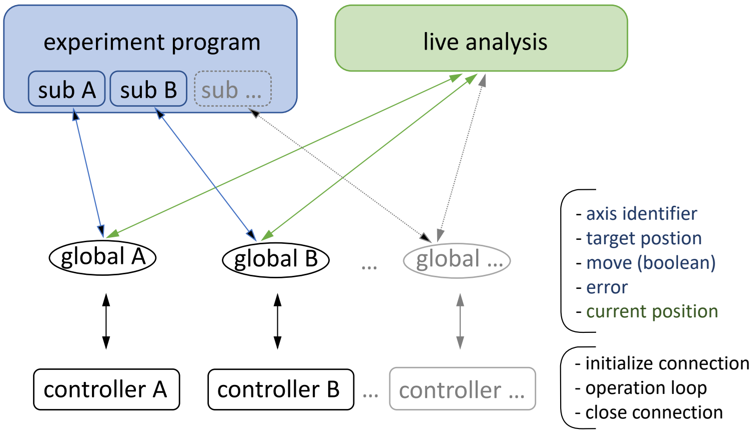

Figure A.3.: General structure of the programs driving an experiment. The main 'experiment program' instance contains the cycled execution steps of the experiment. It communicates via capsuled 'sub-programs' with the controller instances. The 'globals' present each a set of variables (axis identifier, ...) and build the interface of the controller instances of the devices (A, B, ...) to the general programs (experiment program, live analysis). The live analysis program can read the current position from the globals and utilize them to generate preliminary results. The controller instance itself is typically structured in three parts, the initialization of the connection, the operational loop and the closing of the connection.

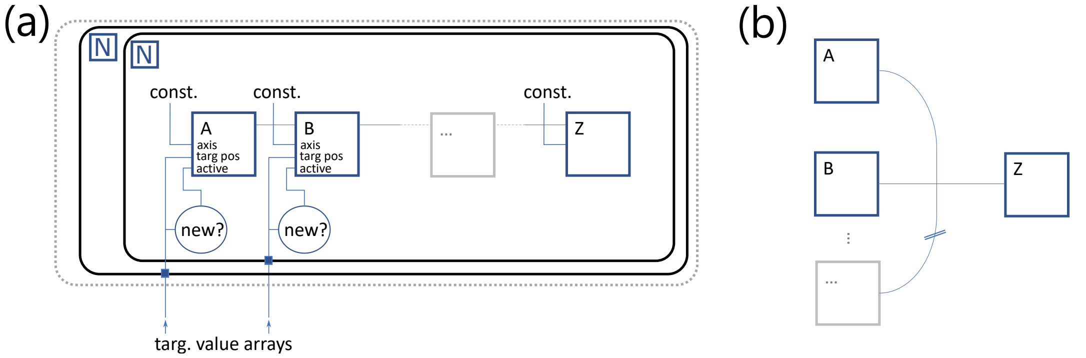

Figure A.4.: **(a)** Structure of the main experiment program instance. The sub-programs (A, B, ...) contain the entire communication with the controller instances. Their order and structure is therefore very easily manageable. For each loop iteration the input target position value is checked for a change compared to the last loop iteration. The target position value arrays are indexed - as typical in LabView - by a loop. Therefore, each independent target position array contributes an additional loop (N). The fixed values for the axis of each controller are constant. Typically the last device within the loop is the recording device (Z), e.g. the CCD camera. Here, the value for the number of frames as well as acquisition time are provided as constants, but can as well be provided on the bases of loop iteration to compensate for systematic alternating measurement signals. **(b)** While for fast stages the controller can be easily driven sequentially, the single controllers can also be driven in parallel. Only the recording device must wait for the stages to achieve their target position.

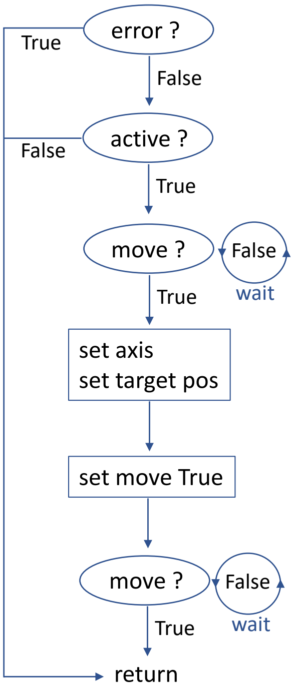

Figure A.5.: Working principle of the sub-program managing the communication with the controller program instances. The variables (*error*, *move*, *axis*, *target position*) are written to and read from the respective global variable. The controller instance reacts on the *move* variable being *True* with reading the axis and target position and initiation the movement. Once it reaches the target position it sets the variable *move* to *False*.

A.3.1. File Structure

Two types of files are written by the controller instance of the XUV camera. The *log file* (fig. A.6(a)) documents all parameters recorded by the individual controller instances (stage positions, gas pressure, camera settings), including notes entered by user, into one file. Each line is written for one execution of the acquisition command, independent of the number of frames of that command. This file thus provides a fast overview of changes in the experimental conditions within a folder of scan files. The first line (header) contains the keys of the recorded data. They are determined at the creation of the folder by the detection of active global variables and hence running controller instances.

(a) log file

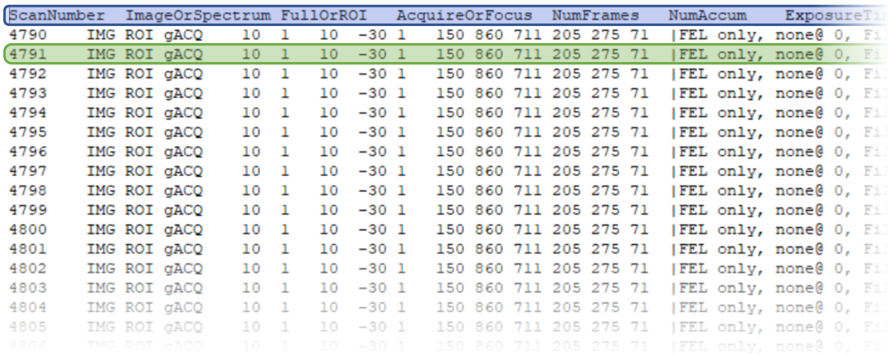

```
ScanNumber  ImageOrSpectrum FullOrROI   AcquireOrFocus  NumFrames   NumAccum    ExposureTi
4790       IMG ROI gACQ     10   1    10   -30 1    150 860 711 205 275 71  |FEL only, none@ 0, Fi
4791       IMG ROI gACQ     10   1    10   -30 1    150 860 711 205 275 71  |FEL only, none@ 0, Fi
4792       IMG ROI gACQ     10   1    10   -30 1    150 860 711 205 275 71  |FEL only, none@ 0, Fi
4793       IMG ROI gACQ     10   1    10   -30 1    150 860 711 205 275 71  |FEL only, none@ 0, Fi
4794       IMG ROI gACQ     10   1    10   -30 1    150 860 711 205 275 71  |FEL only, none@ 0, Fi
4795       IMG ROI gACQ     10   1    10   -30 1    150 860 711 205 275 71  |FEL only, none@ 0, Fi
4796       IMG ROI gACQ     10   1    10   -30 1    150 860 711 205 275 71  |FEL only, none@ 0, Fi
4797       IMG ROI gACQ     10   1    10   -30 1    150 860 711 205 275 71  |FEL only, none@ 0, Fi
4798       IMG ROI gACQ     10   1    10   -30 1    150 860 711 205 275 71  |FEL only, none@ 0, Fi
4799       IMG ROI gACQ     10   1    10   -30 1    150 860 711 205 275 71  |FEL only, none@ 0, Fi
4800       IMG ROI gACQ     10   1    10   -30 1    150 860 711 205 275 71  |FEL only, none@ 0, Fi
4801       IMG ROI gACQ     10   1    10   -30 1    150 860 711 205 275 71  |FEL only, none@ 0, Fi
4802       IMG ROI gACQ     10   1    10   -30 1    150 860 711 205 275 71  |FEL only, none@ 0, Fi
4803       IMG ROI gACQ     10   1    10   -30 1    150 860 711 205 275 71  |FEL only, none@ 0, Fi
4804       IMG ROI gACQ     10   1    10   -30 1    150 860 711 205 275 71  |FEL only, none@ 0, Fi
4805       IMG ROI gACQ     10   1    10   -30 1    150 860 711 205 275 71  |FEL only, none@ 0, Fi
4806       IMG ROI gACQ     10   1    10   -30 1    150 860 711 205 275 71  |FEL only, none@ 0, Fi
```

(b) scan file

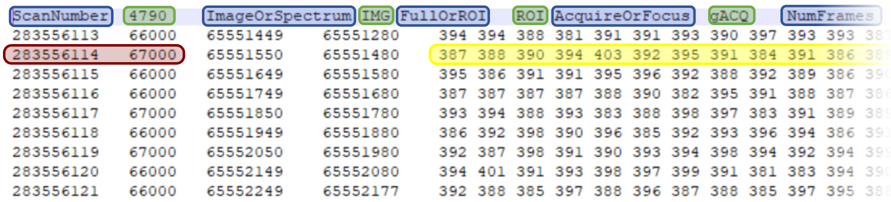

```
ScanNumber  4790    ImageOrSpectrum IMG FullOrROI    ROI AcquireOrFocus  gACQ    NumFrames
283556113   66000   65551449    65551280    394 394 388 381 391 391 393 390 397 393 393 38
283556114   67000   65551550    65551480    387 388 390 394 403 392 395 391 384 391 386 38
283556115   66000   65551649    65551580    395 386 391 391 395 396 392 388 392 389 386 39
283556116   66000   65551749    65551680    387 387 387 387 388 390 382 395 391 388 387 38
283556117   67000   65551850    65551780    393 394 388 393 383 388 398 397 383 391 389 38
283556118   66000   65551949    65551880    386 392 398 390 396 385 392 393 396 394 386 39
283556119   67000   65552050    65551980    392 387 398 391 390 393 394 398 394 392 394 39
283556120   66000   65552149    65552080    394 401 391 393 398 397 399 391 381 383 394 39
283556121   66000   65552249    65552177    392 388 385 397 388 396 387 388 385 397 395 38
```

Figure A.6.: Structure of the files written by the controller instance of the XUV camera. Here, an example from the experiment of the second measurement campaign is shown. **(a)** The *Log file* is appended for every execution of the acquisition command. The automatically generated header contains the keys (blue) of the camera settings in addition to all variables of the controller instances and axes detected active at the creation of the folder. The values (green) for each acquisition command are stored in one line and hence serve as a good overview for human evaluation. **(b)** A *scan file* is created for each acquisition command. Its header contains the information saved redundantly in the log file (keys in blue, values in green). Each recorded frame is written in one line, independent of the recorded data type (e.g. image, spectrum, number of ROIs). The first values represent identifiers for each frame, e.g. the bunch ID of the FLASH facility (red) and other timestamps, followed by the data recorded by the camera (yellow).

Typically a new folder is generated for every measurement for a clean data structure. Files of the second typ, the *scan files* (fig. A.6(b)), are written by the controller instance for every execution of the acquisition command. The header contains the same information as the log file (compare (a) and (b) in figure A.6). This feature creates redundancy of information, since the log file is appended for the entire duration of the experiment and could potentially be corrupted in rare cases.

Each of the following lines contain precisely one recorded frame. This makes the file structure independent of the recorded data type (e.g. image, spectrum, number of regions of interest (ROIs)). The first numerical values in each line represent identifiers, e.g. the so-called bunch ID in the case of FLASH, which can be accompanied by further timestamps for technical redundancy. This is followed by the data recorded with the XUV camera.

To enable the storage of all types of recorded data from the XUV camera into a single line and their subsequent reconstruction, the header contains the full set of information on the structure (fig. A.6(a)). With that information an algorithm can easily recreate the original data by reading out the header. An image is reshaped to a single line by simply concatenating its lines (fig. A.6(b)). The relevant information for its reconstruction is denoted in the header as 'ROIX_0L' describing the length of single pixel line within the image. The complimentary information of the second image dimension is stored in 'ROIY_0L', thus providing the full set of information.

In the case of multiple ROIs, the data are concatenated for the different ROIs (fig. A.6(c)). For recorded spectra this is intuitively clear while for the case of images from multiple ROIs the data of every image is reshaped to a single line as described above. Theses lines of the separate ROIs are then concatenated.

(a) scan file header

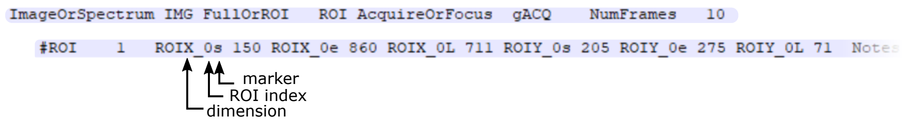

```
ImageOrSpectrum IMG FullOrROI   ROI AcquireOrFocus  gACQ    NumFrames    10
  #ROI     1   ROIX_0s 150 ROIX_0e 860 ROIX_0L 711 ROIY_0s 205 ROIY_0e 275 ROIY_0L 71  Note
```

(b) image reconstruction

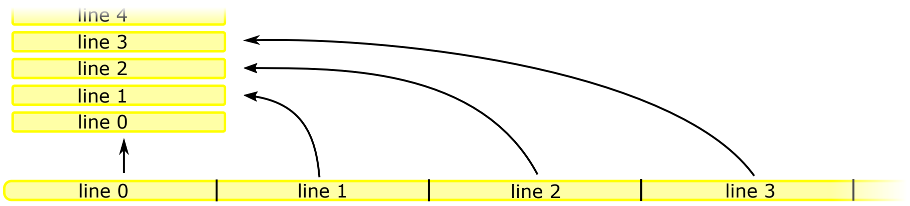

(c) region of interest

Figure A.7.: Structure of the data in the scan files. **(a)** The header contains the information on which type of data is stored including its dimensions. This enables the full reconstruction while storing the information in a single line. The key '#ROI' provides the number of ROIs. The dimensions of ROI with index i are provided by 'ROIX_iL' for the length and 'ROIY_iL' for the height. The remaining information denoted with markers 's' and 'e' instead of 'L' provide the position of the ROI on the CCD chip with 's' and 'e' being the index of the starting and final pixel, respectively. **(b)** An image is store by simply concatenating the single lines. **(c)** Multiple ROIs are stored by concatenating their data, which have been reshaped to a single lines.

A.4. Beamline Images

An example for the newly designed and constructed beamline is provided here with the mirror chamber (fig. A.8). For further details on single elements of the beamline see also [101–103].

One of the most important procedures is the alignment of the chamber, since in the end, the beam which is reflected off the aligned optics has to pass through the fix openings of the chambers. For that purpose, the mirror chamber contains additional flanges. The chamber is aligned in respect to the FEL beam by transmitting an alignment laser through the empty chamber. Figure A.8 shows the incoming beam (yellow + cyan axes) which is centered on the entrance flange as well as on the alignment flange (CF16 window) using glas targets. With this axis aligned, the ellipsoidal mirror is located in the chamber. Its roughly aligned under 8° angel of incidence (brown + pink axes) to center on the second alignment flange (CF40). This port is used during the experiment to couple out the focused FEL beam onto the connected wavefront sensor. The motorized planar mirrors, mounted on a hexapod, are finally aligned to the exit flange (green axis) and the spectrometer entrance in 1.5 m distance.

Apart from the alignment flanges, many additional ports have been added for signal/control-cable feedthroughs as well as as well as optical access into the chamber. Such an addition is represented by the CF 250 ring-structure on the right side of the chamber. It provides six additional CF 63 ports for the 15 channels of the hexapod-based four-split mirror at a strategically important location. The signal cables can only be connected within a short distance behind the actuators. The sockets of the feedthroughs are directly visible and accessible from the outside through the outer flange of the ring structure and without the risk of colliding with the hexapod or its optics. Furthermore, the entire mirror setup can be placed into the chamber in a way protective for the optics through the ring, pointing their surface away from scientist, his/her body parts and lab coat at all times.

Besides the double bread-board M6 thread grid on the base plate, the chamber contains a similar, less dense M6 thread grid on all walls providing mounting flexibility. Even the outer chamber is designed such that a change in the optical pathway, e.g. angle of incidence, only requires the exchange of the CF250 flange containing the the CF40 entrance and exit ports of the beam.

In the following photographs of the experimental setup are depicted (fig. A.11 - A.14).

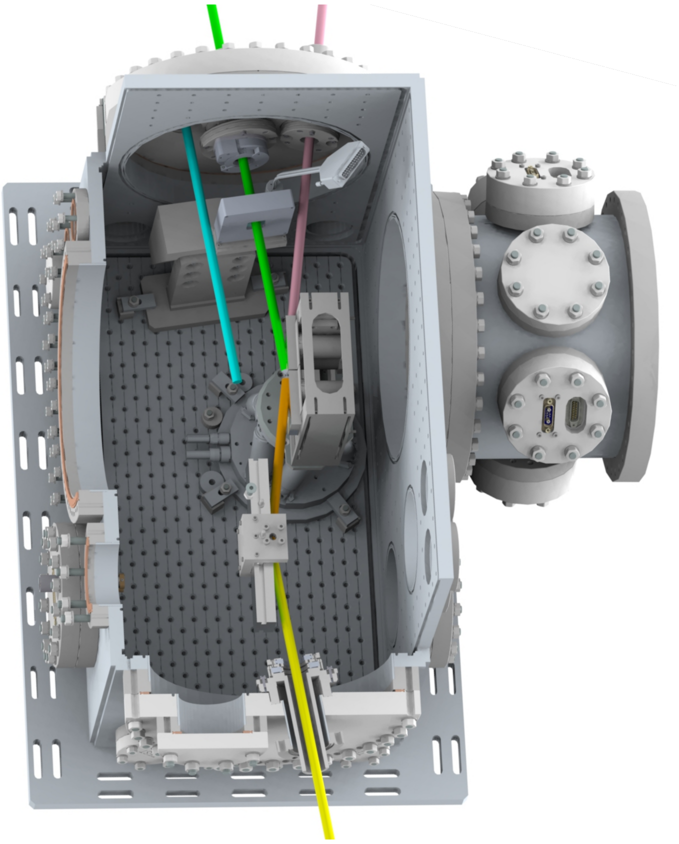

Figure A.8.: Technical rendering of the mirror chamber from the second measurement campaign. For details please see the text.

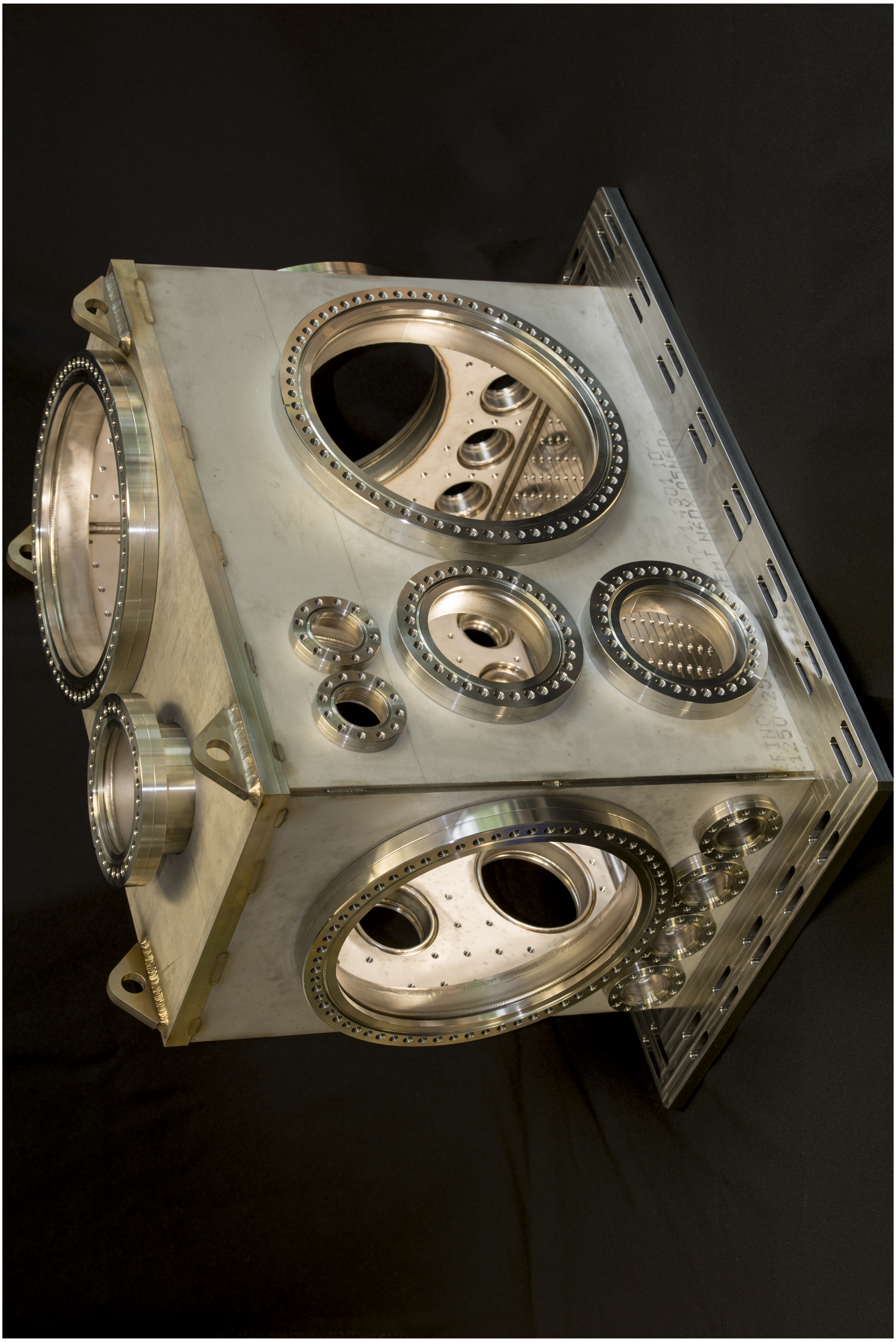

Figure A.9.: Photo (right side) of the raw mirror chamber from the second measurement campaign after completion by the mechanical workshop.

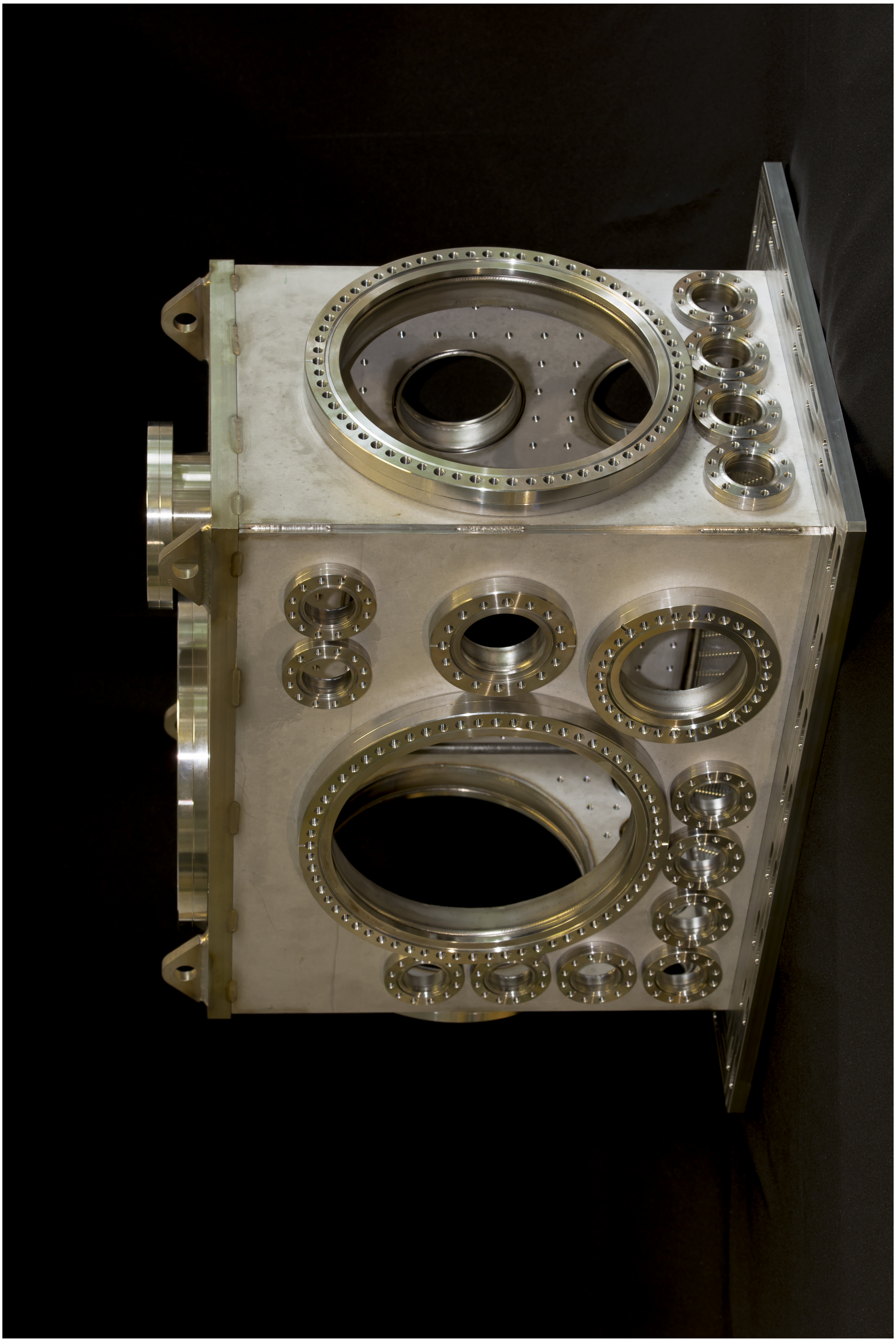

Figure A.10.: Photo (left side) of the raw mirror chamber from the second measurement campaign after completion by the mechanical workshop.

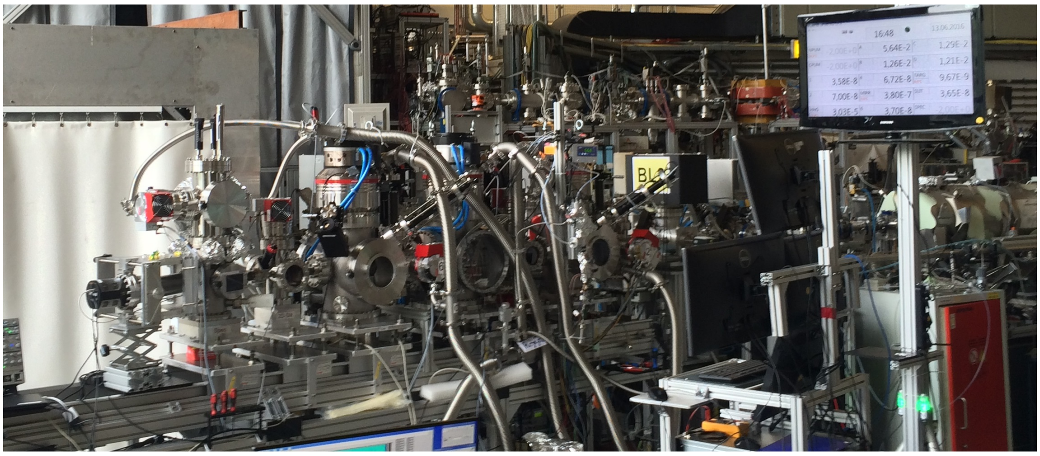

Figure A.11.: Photo of the beamline at the first measurement campaign at FLASH BL2

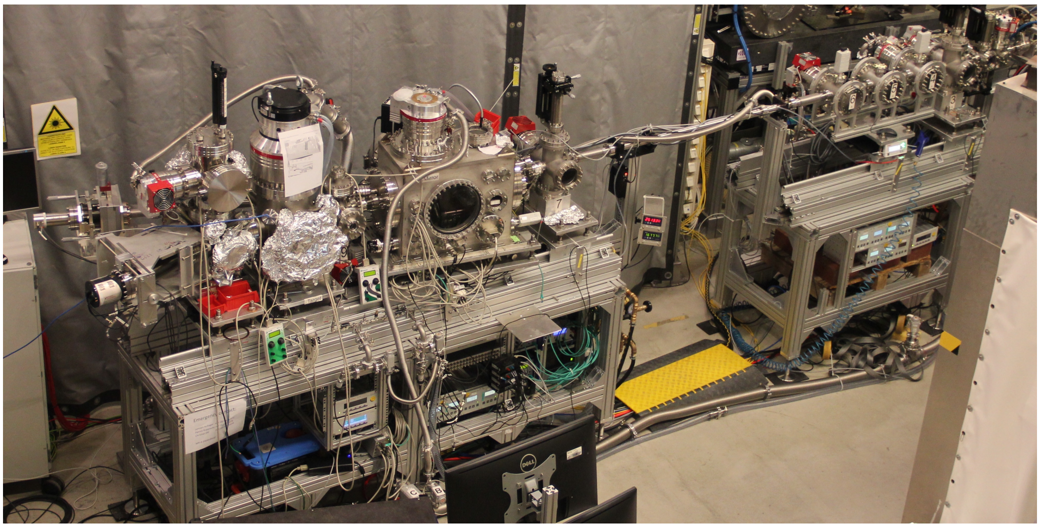

Figure A.12.: Photo of the beamline at the second measurement campaign at FLASH BL2

Figure A.13.: Photo of the inside of the truck transporting the beamline and further equipment (in essence the entire lab, excluding the laser light source), and how the bare BL arrives at FLASH (second campaign)

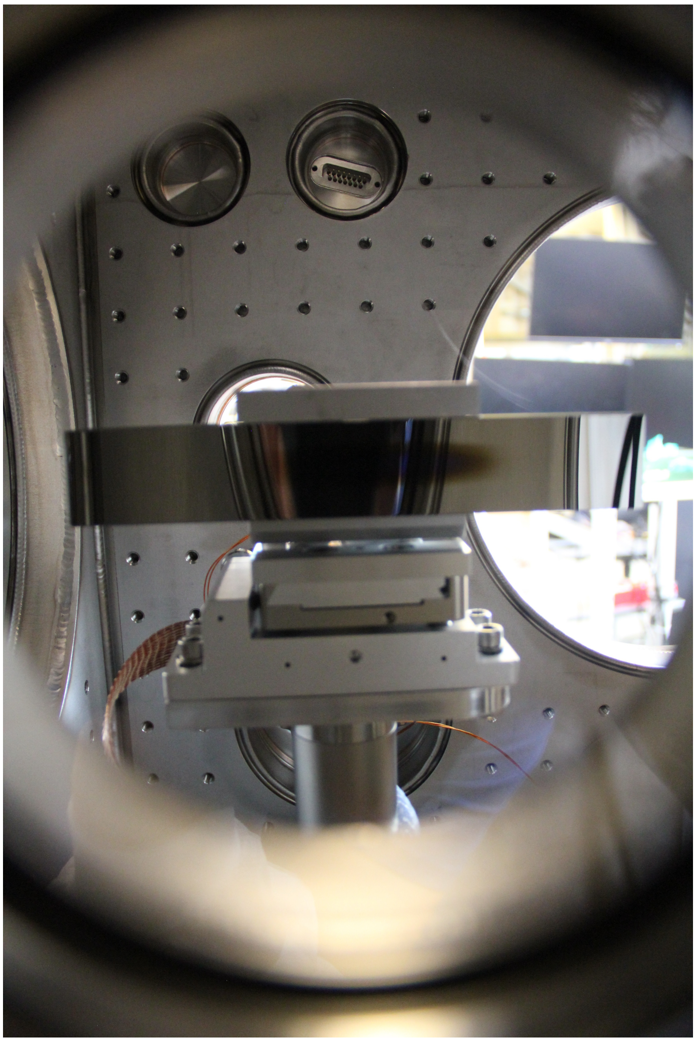

Figure A.14.: Photo of the ellipsoidal mirror in the mirror-vacuum chamber with slight signs of usage after a full campaign, (second campaign).

Bibliography

[1] C. Ott, L. Aufleger, T. Ding, M. Rebholz, A. Magunia, M. Hartmann, V. Stooß, D. Wachs, P. Birk, G. D. Borisova, K. Meyer, P. Rupprecht, C. da Costa Castanheira, R. Moshammer, A. R. Attar, T. Gaumnitz, Z.-H. Loh, S. Düsterer, R. Treusch, J. Ullrich, Y. Jiang, M. Meyer, P. Lambropoulos, and T. Pfeifer. Strong-Field Extreme-Ultraviolet Dressing of Atomic Double Excitation. *Phys. Rev. Lett.*, 123(16):163201, 2019. (Cited page ix)

[2] L. Aufleger, P. Friebel, P. Rupprecht, A. Magunia, T. Ding, M. Rebholz, M. Hartmann, V. Stooß, C. Ott, and T. Pfeifer. Pulse length effects on autoionizing states under the influence of intense SASE XUV fields. *J. Phys. B At. Mol. Opt. Phys.*, 53(23):234002, 2020. (Cited page ix)

[3] L. Aufleger, P. Friebel, P. Rupprecht, A. Magunia, T. Ding, M. Rebholz, M. Hartmann, C. Ott, and T. Pfeifer. Line-shape broadening of an autoionizing state in helium at high XUV intensity. *New J. Phys.*, 10:0–16, 2021. (Cited page ix)

[4] M. Rebholz, T. Ding, V. Despré, et al. All-XUV Pump-Probe Transient Absorption Spectroscopy of the Structural Molecular Dynamics of Di-iodomethane. *Phys. Rev. X*, 11(3):31001, 2021. (Cited page ix)

[5] T. Ding, M. Rebholz, L. Aufleger, M. Hartmann, V. Stooß, A. Magunia, P. Birk, G. D. Borisova, D. Wachs, C. da Costa Castanheira, P. Rupprecht, Y. Mi, A. R. Attar, T. Gaumnitz, Z. H. Loh, S. Roling, M. Butz, H. Zacharias, S. Düsterer, R. Treusch, A. Eislage, S. M. Cavaletto, C. Ott, and T. Pfeifer. Measuring the frequency chirp of extreme-ultraviolet free-electron laser pulses by transient absorption spectroscopy. *Nat. Commun.*, 12(1), 2021. (Cited page x, 77)

[6] T. Ding, M. Rebholz, L. Aufleger, M. Hartmann, V. Stooß, A. Magunia, P. Birk, G. D. Borisova, C. Da Costa Castanheira, P. Rupprecht, Y. Mi, T. Gaumnitz, Z. H. Loh, S. Roling, M. Butz, H. Zacharias, S. Düsterer, R. Treusch, C. Ott, and T. Pfeifer. XUV pump-XUV probe transient absorption spectroscopy at FELs. *Faraday Discuss.*, 228:519–536, 2021. (Cited page x)

[7] A. Magunia, L. Aufleger, T. Ding, P. Rupprecht, M. Rebholz, C. Ott, and T. Pfeifer. Bound-State Electron Dynamics Driven by Near-Resonantly Detuned Intense and Ultrashort Pulsed XUV Fields. *Appl. Sci.*, 10(18):6153, 2020. (Cited page x, 56, 62)

[8] T. Ding, M. Rebholz, L. Aufleger, M. Hartmann, K. Meyer, V. Stooß, A. Magunia, D. Wachs,

P. Birk, Y. Mi, G. D. Borisova, C. D. C. Castanheira, P. Rupprecht, Z.-H. Loh, A. R. Attar, T. Gaumnitz, S. Roling, M. Butz, H. Zacharias, S. Düsterer, R. Treusch, S. M. Cavaletto, C. Ott, and T. Pfeifer. Nonlinear Coherence Effects in Transient-Absorption Ion Spectroscopy with Stochastic Extreme-Ultraviolet Free-Electron Laser Pulses. *Phys. Rev. Lett.*, 123(10): 103001, 2019. (Cited page x)

[9] B. Bransden and C. Joachain. *Physics of Atoms and Molecules.* Prentice Hall, second edi edition, 2014. (Cited page 1)

[10] G. Tanner, K. Richter, and J. M. Rost. The theory of two-electron atoms: Between ground state and complete fragmentation. *Rev. Mod. Phys.*, 72(2):497–544, 2000. (Cited page 1, 2, 20)

[11] C. D. Lin. Hyperspherical coordinate approach to atomic and other Coulombic three-body systems. *Phys. Rep.*, 257(1):1–83, 1995. (Cited page 1)

[12] B. Walker, B. Sheehy, L. F. DiMauro, P. Agostini, K. J. Schafer, and K. C. Kulander. Precision Measurement of Strong Field Double Ionization of Helium. *Phys. Rev. Lett.*, 73(9):1227–1230, 1994. (Cited page 2)

[13] K. Kzazewski and J. H. Eberly. Confluence of Bound-Free Coherences in Laser-Induced Autoionization. *Phys. Rev. Lett.*, 47(6):408–412, 1981. (Cited page 2, 20)

[14] P. Lambropoulos and P. Zoller. Antoionizing states in strong laser fields. *Phys. Rev. A - At. Mol. Opt. Phys.*, 24(1):379–397, 1981. (Cited page 14)

[15] P. Lambropoulos, P. Maragakis, and J. Zhang. Two-electron atoms in strong fields. *Phys. Rep.*, 305(5):203–293, 1998. (Cited page)

[16] S. I. Themelis, P. Lambropoulos, and M. Meyer. Ionization dynamics in double resonance involving autoionizing states in helium: The effect of pulse shapes. *J. Phys. B At. Mol. Opt. Phys.*, 37(21):4281–4293, 2004. (Cited page 2, 20)

[17] J. Ullrich, R. Moshammer, R. Dörner, O. Jagutzki, V. Mergel, H. Schmidt-Böcking, and L. Spielberger. Recoil-ion momentum spectroscopy. *J. Phys. B At. Mol. Opt. Phys.*, 30(13): 2917–2974, 1997. (Cited page 2)

[18] R. Dörner, V. Mergel, O. Jagutzki, L. Spielberger, J. Ullrich, R. Moshammer, and H. Schmidt-Böcking. Cold Target Recoil Ion Momentum Spectroscopy: a 'momentum microscope' to view atomic collision dynamics. *Phys. Rep.*, 330(2-3):95–192, 2000. (Cited page)

[19] J. Ullrich, R. Moshammer, A. Dorn, R. D rner, L. P. H. Schmidt, and H. Schmidt-B cking. Recoil-ion and electron momentum spectroscopy: reaction-microscopes. *Reports Prog. Phys.*, 66(9):1463–1545, 2003. (Cited page 2)

[20] J. R. Harries, J. P. Sullivan, J. B. Sternberg, S. Obara, T. Suzuki, P. Hammond, J. Bozek, N. Berrah, M. Halka, and Y. Azuma. Double Photoexcitation of Helium in a Strong dc

Electric Field. *Phys. Rev. Lett.*, 90(13):133002, 2003. (Cited page 2)

[21] S. Gilbertson, M. Chini, X. Feng, S. Khan, Y. Wu, and Z. Chang. Monitoring and controlling the electron dynamics in helium with isolated attosecond pulses. *Phys. Rev. Lett.*, 105(26): 263003, 2010. (Cited page 2, 19, 20)

[22] V. Gruson, L. Barreau, Á. Jiménez-Galan, F. Risoud, J. Caillat, A. Maquet, B. Carré, F. Lepetit, J.-F. Hergott, T. Ruchon, L. Argenti, R. Taïeb, F. Martín, and P. Salières. Attosecond dynamics through a Fano resonance: Monitoring the birth of a photoelectron. *Science*, 354(6313):734–738, 2016. (Cited page 20)

[23] M. Ossiander, F. Siegrist, V. Shirvanyan, R. Pazourek, A. Sommer, T. Latka, A. Guggenmos, S. Nagele, J. Feist, J. Burgdörfer, R. Kienberger, and M. Schultze. Attosecond correlation dynamics. *Nat. Phys.*, 13(3):280–285, 2017. (Cited page 2, 20)

[24] Z. H. Loh, C. H. Greene, and S. R. Leone. Femtosecond induced transparency and absorption in the extreme ultraviolet by coherent coupling of the He 2s2p (1Po) and 2p2 (1Se) double excitation states with 800 nm light. *Chem. Phys.*, 350(1-3):7–13, 2008. (Cited page 2, 20)

[25] C. Ott, A. Kaldun, P. Raith, K. Meyer, M. Laux, J. Evers, C. H. Keitel, C. H. Greene, and T. Pfeifer. Lorentz meets Fano in spectral line shapes: a universal phase and its laser control. *Science*, 340(6133):716–20, 2013. (Cited page 2, 18, 19, 60, 77)

[26] C. Ott, A. Kaldun, L. Argenti, P. Raith, K. Meyer, M. Laux, Y. Zhang, A. Blättermann, S. Hagstotz, T. Ding, R. Heck, J. Madroñero, F. Martín, and T. Pfeifer. Reconstruction and control of a time-dependent two-electron wave packet. *Nature*, 516(7531):374–378, 2014. (Cited page)

[27] A. Blättermann. *Impulsive control of the atomic dipole response in the time and frequency domain.* Dissertation, Ruperto-Carola-University Heidelberg, 2016. (Cited page 19)

[28] A. Kaldun, C. Ott, A. Blättermann, M. Laux, K. Meyer, T. Ding, A. Fischer, and T. Pfeifer. Extracting Phase and Amplitude Modifications of Laser-Coupled Fano Resonances. *Phys. Rev. Lett.*, 112(10):103001, 2014. (Cited page)

[29] A. Kaldun, A. Blättermann, V. Stooß, S. Donsa, H. Wei, R. Pazourek, S. Nagele, C. Ott, C. D. Lin, J. Burgdörfer, and T. Pfeifer. Observing the ultrafast buildup of a Fano resonance in the time domain. *Science*, 354(6313):738–741, 2016. (Cited page 2, 20, 77)

[30] V. Stooß, S. M. Cavaletto, S. Donsa, A. Blättermann, P. Birk, C. H. Keitel, I. Březinová, J. Burgdörfer, C. Ott, and T. Pfeifer. Real-Time Reconstruction of the Strong-Field-Driven Dipole Response. *Phys. Rev. Lett.*, 121(17):173005, 2018. (Cited page 2, 20)

[31] W. Ackermann, G. Asova, V. Ayvazyan, et al. Operation of a free-electron laser from the extreme ultraviolet to the water window. *Nat. Photonics*, 1(6):336–342, 2007. (Cited page 3, 29)

[32] N. Hartmann, G. Hartmann, R. Heider, M. S. Wagner, M. Ilchen, J. Buck, A. O. Lindahl, C. Benko, J. Grünert, J. Krzywinski, J. Liu, A. A. Lutman, A. Marinelli, T. Maxwell, A. A. Miahnahri, S. P. Moeller, M. Planas, J. Robinson, A. K. Kazansky, N. M. Kabachnik, J. Viefhaus, T. Feurer, R. Kienberger, R. N. Coffee, and W. Helml. Attosecond time-energy structure of X-ray free-electron laser pulses. *Nat. Photonics*, 12(4):215–220, 2018. (Cited page 3, 56)

[33] T. Fließbach. *Quantenmechanik*. Springer, 2018. (Cited page 6)

[34] S. H. Autler and C. H. Townes. Stark Effect in Rapidly Varying Fields. *Phys. Rev.*, 100(2): 703–722, 1955. (Cited page 11)

[35] B. R. Mollow. Power Spectrum of Light Scattered by Two-Level Systems. *Phys. Rev.*, 188(5): 1969–1975, 1969. (Cited page 11)

[36] U. Fano. Effects of configuration interaction on intensities and phase shifts. *Phys. Rev.*, 124 (6):1866–1878, 1961. (Cited page 12, 14)

[37] J. Fraunhofer. Bestimmung des Brechungs- und des Farbenzerstreungs- Vermögens verschiedener Glasarten, in Bezug auf die Vervollkommnung achro- matischer Fernröhre. *Ann. Phys.*, 56(7):264–313, 1817. (Cited page 15)

[38] G. Kirchhoff and R. Bunsen. Chemische Analyse durch Spectralbeobachtungen. *Ann. Phys.*, 189(4):337–381, 1861. (Cited page 15)

[39] M. Wu, S. Chen, S. Camp, K. J. Schafer, and M. B. Gaarde. Theory of strong-field attosecond transient absorption. *J. Phys. B At. Mol. Opt. Phys.*, 49(6):062003, 2016. (Cited page 18)

[40] M. Domke, K. Schulz, G. Remmers, G. Kaindl, and D. Wintgen. High-resolution study of 1 P o double-excitation states in helium. *Phys. Rev. A*, 53(3):1424–1438, 1996. (Cited page 19, 20, 42, 49, 53, 55, 56, 71, 73)

[41] R. P. Madden and K. Codling. New Autoionizing Atomic Energy Levels in He, Ne, and Ar. *Phys. Rev. Lett.*, 10(12):516–518, 1963. (Cited page)

[42] R. P. Madden and K. Codling. Two-Electron Excitation States in Helium. *Astrophys. J.*, 141: 364, 1965. (Cited page)

[43] H. D. Morgan and D. L. Ederer. Photoionization cross section of helium for photon energies 59-67 eV: The (sp,2n+)Po1 Rydberg series of autoionizing resonances. *Phys. Rev. A*, 29(4): 1901–1906, 1984. (Cited page 19)

[44] J. M. Madey. Stimulated emission of bremsstrahlung in a periodic magnetic field. *J. Appl. Phys.*, 42(5):1906–1913, 1971. (Cited page 21)

[45] L. R. Elias, W. M. Fairbank, J. M. Madey, H. A. Schwettman, and T. I. Smith. Observation of stimulated emission of radiation by relativistic electrons in a spatially periodic transverse magnetic field. *Phys. Rev. Lett.*, 36(13):717–720, 1976. (Cited page)

[46] D. A. G. Deacon, L. R. Elias, J. M. J. Madey, G. J. Ramian, H. A. Schwettman, and T. I. Smith. First Operation of a Free-Electron Laser. *Phys. Rev. Lett.*, 38(16):892—-894, 1977. (Cited page 21)

[47] P. Schmüser, M. Dohlus, and J. Rossbach. *Ultraviolet and Soft X-Ray Free-Electron Lasers*. Springer, Berlin, Heidelberg, 2009. (Cited page 21, 22, 23, 25, 26)

[48] J. Li, J. Lu, A. Chew, S. Han, J. Li, Y. Wu, H. Wang, S. Ghimire, and Z. Chang. Attosecond science based on high harmonic generation from gases and solids. *Nat. Commun.*, 11(1):2748, 2020. (Cited page 21)

[49] G. P. Williams. A general review of synchrotron radiation, its uses and special technologies. *Vacuum*, 32(6):333–345, 1982. (Cited page 21)

[50] J. Als-Nielsen and D. McMorrow. *Elements of Modern X-ray Physics*. John Wiley & Sons, Ltd, 2011. (Cited page 22)

[51] P. Zeitoun, G. Faivre, S. Sebban, T. Mocek, A. Hallou, M. Fajardo, D. Aubert, P. Balcou, F. Burgy, D. Douillet, S. Kazamias, G. de Lachèze-Murel, T. Lefrou, S. le Pape, P. Mercère, H. Merdji, A. S. Morlens, J. P. Rousseau, and C. Valentin. A high-intensity highly coherent soft X-ray femtosecond laser seeded by a high harmonic beam. *Nature*, 431(7007):426–429, 2004. (Cited page 25)

[52] N. S. Mirian, M. Di Fraia, S. Spampinati, et al. Generation and measurement of intense few-femtosecond superradiant extreme-ultraviolet free-electron laser pulses. *Nat. Photonics*, 15(7):523–529, 2021. (Cited page 26, 77)

[53] J. Amann, W. Berg, V. Blank, et al. Demonstration of self-seeding in a hard-X-ray free-electron laser. *Nat. Photonics*, 6(10):693–698, 2012. (Cited page 26)

[54] K. Tiedtke, A. Azima, N. von Bargen, et al. The soft x-ray free-electron laser FLASH at DESY: beamlines, diagnostics and end-stations. *New J. Phys.*, 11(2):023029, 2009. (Cited page 29, 30, 31)

[55] FLASH Parameters, 2021. (Cited page 29)

[56] O. H. Altenmueller, R. R. Larsen, and G. A. Loew. Investigations of traveling-wave separators for the stanford two-mile linear accelerator. *Rev. Sci. Instrum.*, 35(4):438–442, 1964. (Cited page 29)

[57] S. Düsterer, M. Rehders, A. Al-Shemmary, et al. Development of experimental techniques for the characterization of ultrashort photon pulses of extreme ultraviolet free-electron lasers. *Phys. Rev. Spec. Top. - Accel. Beams*, 17(12):120702, 2014. (Cited page 29)

[58] Free-electron laser FLASH, 2021. (Cited page 30)

[59] K. Tiedtke, J. Feldhaus, U. Hahn, U. Jastrow, T. Nunez, T. Tschentscher, S. V. Bobashev, A. A. Sorokin, J. B. Hastings, S. Möller, L. Cibik, A. Gottwald, A. Hoehl, U. Kroth, M. Krumrey,

H. Schöppe, G. Ulm, and M. Richter. Gas detectors for x-ray lasers. *J. Appl. Phys.*, 103(9): 094511, 2008. (Cited page 31)

[60] G. Brenner, S. Kapitzki, M. Kuhlmann, E. Ploenjes, T. Noll, F. Siewert, R. Treusch, K. Tiedtke, R. Reininger, M. Roper, M. Bowler, F. Quinn, and J. Feldhaus. First results from the online variable line spacing grating spectrometer at FLASH. *Nucl. Instruments Methods Phys. Res. Sect. A Accel. Spectrometers, Detect. Assoc. Equip.*, 635(1):S99–S103, 2011. (Cited page 32, 36)

[61] A. Magunia. *Doubly-Excited Helium Strongly Driven with Short and Long Wavelength Pulses.* Master thesis, Ruperto-Carola-University Heidelberg, 2018. (Cited page 32)

[62] F. Henrich. *An investigation into experimental transient absorption measurements of neon by a few-level simulation.* Bachelor thesis, Ruperto-Carola-University Heidelberg, 2020. (Cited page 32)

[63] BL Beamlines (FLASH1), 2021. (Cited page 33)

[64] A. A. Sorokin, A. Gottwald, A. Hoehl, U. Kroth, H. Schöppe, G. Ulm, M. Richter, S. V. Bobashev, I. V. Domracheva, D. N. Smirnov, K. Tiedtke, S. Düsterer, J. Feldhaus, U. Hahn, U. Jastrow, M. Kuhlmann, T. Nunez, E. Plönjes, and R. Treusch. Method based on atomic photoionization for spot-size measurement on focused soft x-ray free-electron laser beams. *Appl. Phys. Lett.*, 89(22):1–4, 2006. (Cited page 33)

[65] optiX fab GmbH: Off-axis Ellipsoid, model: major: 43000mm, minor: 1283.11mm, Eccentricity 42018.7mm, 2017. (Cited page 33)

[66] B. Flöter, P. Juranic, S. Kapitzki, B. Keitel, K. Mann, E. Plönjes, B. Schäfer, and K. Tiedtke. EUV Hartmann sensor for wavefront measurements at the Free-electron LASer in Hamburg. *New J. Phys.*, 12:0–13, 2010. (Cited page 34)

[67] B. Keitel, E. Plönjes, S. Kreis, M. Kuhlmann, K. Tiedtke, T. Mey, B. Schäfer, and K. Mann. Hartmann wavefront sensors and their application at FLASH. *J. Synchrotron Radiat.*, 23: 43–49, 2016. (Cited page 34)

[68] B. Flöter, P. Juranic, S. Kapitzki, B. Keitel, K. Mann, E. Plönjes, B. Schäfer, and K. Tiedtke. EUV Hartmann sensor for wavefront measurements at the Free-electron LASer in Hamburg. *New J. Phys.*, 12, 2010. (Cited page 34)

[69] R. Heck. *Erzeugung hoher Harmonischer durch Interferenz freier Elektronenwellenpakete / Charakterisierung und Einrichtung eines Toroidalspiegels.* Bachelor thesis, Ruprecht-Karls-Universität Heidelberg, 2010. (Cited page 34)

[70] Smaract: Piezo Stick-Slip Stages, model SLLV42 -S-HV, 2021. (Cited page 34)

[71] Hitachi: Aberration-Corrected Concave Gratings for Flat-Field Spectrographs, model 001-0640, 2021. (Cited page 35)

[72] T. Kita, T. Harada, N. Nakano, and H. Kuroda. Mechanically ruled aberration-corrected concave gratings for a flat-field grazing-incidence spectrograph. *Appl. Opt.*, 22(4):512, 1983. (Cited page 35)

[73] H. A. Rowland. XXIX. On concave gratings for optical purposes. *London, Edinburgh, Dublin Philos. Mag. J. Sci.*, 16(99):197–210, 1883. (Cited page 35)

[74] H. G. Beutler. The Theory of the Concave Grating. *J. Opt. Soc. Am.*, 35(5):311, 1945. (Cited page 35)

[75] Princeton Instruments: PIXIS, model XO:400B, 2021. (Cited page 36)

[76] L. J. Frasinski. Covariance mapping techniques. *J. Phys. B At. Mol. Opt. Phys.*, 49(15): 152004, 2016. (Cited page 41)

[77] J. A. Fleck, J. R. Morris, and M. D. Feit. Time-dependent propagation of high-energy laser beams through the atmosphere. *Appl. Phys.*, 10:129–160, 1976. (Cited page 47)

[78] A. D. Bandrauk and H. Shen. Exponential split operator methods for solving coupled time-dependent Schrödinger equations. *J. Chem. Phys.*, 99(2):1185–1193, 1993. (Cited page 47)

[79] A. D. Bandrauk and H. Shen. Improved exponential split operator method for solving the time-dependent Schrödinger equation. *Chem. Phys. Lett.*, 176(5):428–432, 1991. (Cited page 48)

[80] G. V. Marr and J. B. West. Absolute photoionization cross-section tables for helium, neon, argon, and krypton in the VUV spectral regions, 1976. (Cited page 49)

[81] J. A. R. Samson, Z. X. He, L. Yin, and G. N. Haddad. Precision measurements of the absolute photoionization cross sections of He. *J. Phys. B At. Mol. Opt. Phys.*, 27(5):887–898, 1994. (Cited page 49)

[82] J. M. Rost, K. Schulz, M. Domke, and G. Kaindl. Resonance parameters of photo doubly excited helium. *J. Phys. B At. Mol. Opt. Phys.*, 30(21):4663–4694, 1997. (Cited page 49)

[83] T. Pfeifer, Y. Jiang, S. Düsterer, R. Moshammer, and J. Ullrich. Partial-coherence method to model experimental free-electron laser pulse statistics. *Opt. Lett.*, 35(20):3441, 2010. (Cited page 49, 51)

[84] I. J. Bermúdez Macias, S. Düsterer, R. Ivanov, J. Liu, G. Brenner, J. Rönsch-Schulenburg, M. K. Czwalinna, and M. V. Yurkov. Study of temporal, spectral, arrival time and energy fluctuations of SASE FEL pulses. *Opt. Express*, 29(7):10491, 2021. (Cited page 50)

[85] K. Meyer. *Coherent and statistical phase control and measurments of time-dependent quantum dynamics.* Dissertation, Ruperto-Carola-University Heidelberg, 2014. (Cited page 51, 56)

[86] W. F. Schlotter, F. Sorgenfrei, T. Beeck, M. Beye, S. Gieschen, H. Meyer, M. Nagasono,

A. Föhlisch, and W. Wurth. Longitudinal coherence measurements of an extreme-ultraviolet free-electron laser. *Opt. Lett.*, 35(3):372, 2010. (Cited page 56)

[87] J. J. Yeh and I. Lindau. Atomic Subshell Photoionization Cross Sections and Asymmetry Parameters: 1 <= Z <= 103. *At. Data Nucl. Data Tables*, 32(l):1–155, 1985. (Cited page 72)

[88] M. L. Citron, H. R. Gray, C. W. Gabel, and C. R. Stroud. Experimental study of power broadening in a two-level atom. *Phys. Rev. A*, 16(4):1507–1512, 1977. (Cited page 76)

[89] E. P. Kanter, B. Krässig, Y. Li, A. M. March, P. Ho, N. Rohringer, R. Santra, S. H. Southworth, L. F. Dimauro, G. Doumy, C. A. Roedig, N. Berrah, L. Fang, M. Hoener, P. H. Bucksbaum, S. Ghimire, D. A. Reis, J. D. Bozek, C. Bostedt, M. Messerschmidt, and L. Young. Unveiling and driving hidden resonances with high-fluence, high-intensity X-ray pulses. *Phys. Rev. Lett.*, 107(23):233001, 2011. (Cited page 77)

[90] K. C. Prince, E. Allaria, C. Callegari, et al. Coherent control with a short-wavelength free-electron laser. *Nat. Photonics*, 10(3):176–179, 2016. (Cited page 77)

[91] A. A. Lutman, T. J. Maxwell, J. P. MacArthur, M. W. Guetg, N. Berrah, R. N. Coffee, Y. Ding, Z. Huang, A. Marinelli, S. Moeller, and J. C. U. Zemella. Fresh-slice multicolour X-ray free-electron lasers. *Nat. Photonics*, 10(11):745–750, 2016. (Cited page)

[92] N. Hartmann and J. M. Glownia. Attosecond coherent control at FELs. *Nat. Photonics*, 10 (3):148–150, 2016. (Cited page)

[93] L. Young, K. Ueda, M. Gühr, et al. Roadmap of ultrafast x-ray atomic and molecular physics. *J. Phys. B At. Mol. Opt. Phys.*, 51(3):032003, 2018. (Cited page 77)

[94] B. Bergues, D. E. Rivas, M. Weidman, A. A. Muschet, W. Helml, A. Guggenmos, V. Pervak, U. Kleineberg, G. Marcus, R. Kienberger, D. Charalambidis, P. Tzallas, H. Schröder, F. Krausz, and L. Veisz. Tabletop nonlinear optics in the 100-eV spectral region. *Optica*, 5(3):237, 2018. (Cited page 77)

[95] B. Major, O. Ghafur, K. Kovács, K. Varjú, V. Tosa, M. J. J. Vrakking, and B. Schütte. Compact intense extreme-ultraviolet source. *Optica*, 8(7):960, 2021. (Cited page 77)

[96] S. Mukamel, Y. Tanimura, and P. Hamm. Coherent Multidimensional Optical Spectroscopy. *Acc. Chem. Res.*, 42(9):1207–1209, 2009. (Cited page 77)

[97] P. Hamm and M. Zanni. *Concepts and Methods of 2D Infrared Spectroscopy*. Cambridge University Press, Cambridge, 2011. (Cited page)

[98] M. Kowalewski, B. P. Fingerhut, K. E. Dorfman, K. Bennett, and S. Mukamel. Simulating Coherent Multidimensional Spectroscopy of Nonadiabatic Molecular Processes: From the Infrared to the X-ray Regime. *Chem. Rev.*, 117(19):12165–12226, 2017. (Cited page 77)

[99] L. Foglia, F. Capotondi, R. Mincigrucci, D. Naumenko, E. Pedersoli, A. Simoncig, G. Kurdi, A. Calvi, M. Manfredda, L. Raimondi, N. Mahne, M. Zangrando, C. Masciovecchio, and

F. Bencivenga. First Evidence of Purely Extreme-Ultraviolet Four-Wave Mixing. *Phys. Rev. Lett.*, 120(26):263901, 2018. (Cited page 77)

[100] Y. Kayser, C. Milne, P. Juranić, L. Sala, J. Czapla-Masztafiak, R. Follath, M. Kavčič, G. Knopp, J. Rehanek, W. Błachucki, M. G. Delcey, M. Lundberg, K. Tyrała, D. Zhu, R. Alonso-Mori, R. Abela, J. Sá, and J. Szlachetko. Core-level nonlinear spectroscopy triggered by stochastic X-ray pulses. *Nat. Commun.*, 10(1):4761, 2019. (Cited page 77)

[101] L. Aufleger. *Measurement of electron dynamics in atoms and molecules with intense XUV FEL radiation.* Master thesis, University of Heidelberg In, 2016. (Cited page 88)

[102] T. Ding. *Quantum dynamics in weak and strong fields measured by XUV nonlinear spectroscopy.* Dissertation, Ruperto-Carola-University of Heidelberg, 2018. (Cited page)

[103] M. Rebholz. *All-XUV pump-probe transient absorption spectroscopy on the dissociation dynamics of small molecules.* Dissertation, Ruperto-Carola-University of Heidelberg, 2020. (Cited page 88)

Danksagung

Mein außerordentlicher Dank für die Unterstützung bei dieser Arbeit gilt:

Prof. Dr. Thomas Pfeifer für die Möglichkeit, diese Forschungsarbeit in seiner Arbeitsgruppe durchzuführen und die hier vorliegende Doktorarbeit anzufertigen. Weiterhin für die allzeit offene Tür bei Fragestellungen und Problemen sowie für Diskussionen und seine Fähigkeit bei Meetings, auch während frustrierender Arbeitsphasen, Motivation und Begeisterung zu versprühen.

Prof. Dr. Andreas Wolf für die Übernahme des Zweitgutachtens.

Prof. Dr. Joerg Jaeckel und Prof. Dr. Lothar Schad für die Vervollständigung des Prüfungskomitees.

Dr. Christian Ott für die direkte Betreuung im Rahmen der Promotion und die vielen hilfreichen Diskussionen während der Arbeitsabschnitte.

Dem gesamten X-MuSIC- und Interatto-Team sowie den weiteren Kollegen, mit welchen die Messzeit-Kampagnen erst möglich geworden sind. Hierbei insbesondere:

> Dr. Thomas Ding und Dr. Marc Rebholz für die Aufnahme in ihr Team, in welchem wir gemeinsam das Experiment erfolgreich umsetzen konnten.
>
> Alexander Magunia für die wertvollen Diskussionen zu den numerischen Simulationen.
>
> Patrick Friebel für die gute Zusammenarbeit und die tatkräftige Unterstützung bei der Strahlzeit 2018 und der Datenauswertung.
>
> Zuletzt vor allem Patrick D. Rupprecht für die gemeinsame Zeit, die bereichernden Diskussionen, on und off topic, die gegenseitige Unterstützung und die kontinuierliche Begeisterung für Qualitätssparwitze.

Den Gewerken am MPI-K, vor allem der Konstruktion, der Zentralen Feinmechanik und der Elektronik. Hierbei insbesondere auch der Elektronik Ausbildungswerkstatt für die Unterstützung bei der Umsetzung unserer Ideen.

Dem gesamten Team der IT für die kompetente, unkomplizierte und zuweilen kurzfristige Lösung nicht immer trivialer Probleme.

Dr. Claus Dieter Schröter für die Beratung hinsichtlich technischer Details und dem

entsprechenden Vorgehen.

Christian Kaiser für seine außerordentliche Tatkraft und guten Laune während der Arbeit und seine Direktheit.

Den Teams am FLASH, vor allem Dr. Stefan Düsterer et al. für die Unterstützung vor Ort und ihre Geduld und Hilfsbereitschaft, den beteiligten IT-Spezialisten für die Lösung der Herausforderungen bei der Integration unseres Equipments am FLASH, sowie Dr. Barbara Keitel et al. für die Unterstützung bei der Nutzung des Wellenfrontsensors.

Für den intensiven Austausch und Anmerkungen rund um die Verfassung dieser Dissertation danke ich meinen Freunden.

Meinen Eltern, Dr. G. und Dr. P. Aufleger, für die Ermöglichung dieses Pfades, der mich bis zum Abschluss der Promotionsarbeit geführt hat, und ihre ununterbrochene Unterstützung,

Prof. Dr. H.G. und Dr. C. Penzel für ihr offenes Ohr, die klugen Gedanken und den Austausch von Perspektiven.

Dr. I. Weigl für den ausdauernden und auch emotionalen Rückhalt.

Erklärung/*Declaration*

Ich versichere hiermit, dass ich diese Arbeit selbstständig verfasst, und keine anderen als die angegebenen Quellen und Hilfsmittel verwendet habe.
I hereby certify, that this thesis is entirely my own original work except where indicated otherwise.

Heidelberg, den 22. November 2021 ....